Studies in Thin Shell Buckling: Experiments, Computations and Design Implications

by

Ashok Kumar

DEPARTMENT OF MECHANICAL ENGINEERING

INDIAN INSTITUTE OF TECHNOLOGY KANPUR

October 11, 2022

Studies in Thin Shell Buckling: Experiments, Computations and Design Implications

A Thesis Submitted

in Partial Fulfillment of the Requirements

for the Degree of

DOCTOR OF PHILOSOPHY

by

Ashok Kumar

Roll Number: 12205063

DEPARTMENT OF MECHANICAL ENGINEERING

INDIAN INSTITUTE OF TECHNOLOGY KANPUR

October 11, 2022

CERTIFICATE

It is certified that the work contained in the thesis titled "**Studies in Thin Shell Buckling: Experiments, Computations and Design Implications**" by Ashok Kumar has been carried out under our supervision and that this work has not been submitted elsewhere for a degree.

Dr. A. John Arul
Professor, HBNI
Head RSDD /RDTG,
IGCAR, Kalpakkam-603102
(External advisor)

Dr. Anindya Chatterjee
Professor
Department of Mechanical Engineering
Indian Institute of Technology, Kanpur
Kanpur-208016.

December 10, 2021

DECLARATION

This is to certify that the thesis titled Studies in Thin Shell Buckling: Experiments, Computations and Design Implications has been authored by me. It presents the research conducted by me under the supervision of Dr. Anindya Chatterjee and Dr. A. John Arul (external guide)

To the best of my knowledge, it is an original work, both in terms of research content and narrative, and has not been submitted elsewhere, in part or in full, for a degree. Further, due credit has been attributed to the relevant state-of-the-art and collaborations (if any) with appropriate citations and acknowledgements, in line with established norms and practices.

Signature

Name: Ashok Kumar

Programme: PhD/MTech/MDes

Department: Mechanical Engineering

Indian Institute of Technology Kanpur
Kanpur 208016

SYNOPSIS

In this thesis we study experimental and computational aspects as well as design implications of thin shell buckling.

Thin shells can buckle at a fraction of their theoretical elastic buckling load. Thus, experimental buckling studies have been useful in developing understanding of shell buckling. Shell buckling experiments in the past were conducted on large scale structures but had relatively small sample sizes. One part of this thesis presents experimental shell buckling studies with small specimens but large sample sizes. Note that buckling experiments have strongly influenced shell design practices for safety-critical structures. Hence, understanding the extent of variability in large-sample buckling experiments and the factors contributing to such variability is of both theoretical and practical significance. In this thesis, we present 100 buckling experiments each, on two shell geometries, to study statistical variability in their buckling loads. We demonstrate that interaction between geometrical imperfection and contact loading can lead to higher variability in the buckling loads of shells.

Following up on the experiments, we critically reexamine an imperfection estimation method in the design code RCC-MR. We show that one particular method of imperfection estimation allows potentially nonconservative results, leading to surprisingly high predictions of safe buckling loads. Finally, using detailed computations, we unequivocally prove that this method of imperfection estimation leads to nonconservative buckling loads for two design examples.

Thus, the work in this thesis comprises of three parts. In the first part, we carry out one hundred buckling experiments each, for two different thin shell geometries. One is a dome-like shell with a flat base (a bowl), and the other is a truncated conical shell with a flat base (a tumbler). The test shells are notionally identical, mass-produced, and made of stainless steel. We provide detailed material and geometric characterizations of both shell geometries. The buckling experiment in each case is carried out by axially

compressing shell specimens between two rigid plates. The load-displacement curves of 100 bowl shells show variability by a factor of 2 and stable post-buckling behaviour. The load-displacement curves of the conical shell show variability by a factor of 5 and unstable post-buckling behaviour.

We present two sets of axisymmetric finite element simulations to explain the large scatter in buckling loads and the initial part of the post-buckling behaviour of the conical shells. In one set of simulations, loads are directly applied as tractions on the conical shell. In the second set of simulations, loads are applied on the conical shell through contact with a rigid plate. Compared to simulations with traction loading, the simulations with contact load show twice as much sensitivity to geometric imperfections. The results demonstrate that interaction between contact loading and geometric imperfection leads to higher variability in buckling load.

In the second part, we examine one particular imperfection estimation method in RCC-MR, which is here called the "third method", with three design examples. The first example is a nonuniform cylindrical shell closed with a spherical endcap subjected to external pressure. The second example is a cylinder with an ellipsoidal head subjected to internal pressure. The third example is an L-shaped pipe subjected to an end load.

We present detailed finite element calculations and compute imperfection estimates and safe buckling loads for all three design examples. We show that the third method of RCC-MR results in very small imperfection estimates compared to the actual geometric imperfection values, and leads to surprisingly high predictions of safe buckling loads for all design examples. Specifically, in the second and the third design example, the computed imperfection estimate is insensitive to the actual geometric imperfection, resulting in the computed safe buckling load becoming independent of the actual geometric imperfection. The three design examples reveal scenarios in which a designer may derive a false sense of safety from the design code for a borderline safe design and may further reduce shell thickness, resulting in an unsafe design for safety-critical structures.

In the third and final part, we motivate our approach and first discuss bounds on safe loads in a design activity. We then present two design examples to prove nonconservatisim in the third method of RCC-MR. The two examples are a spherical shell and a toripsherical shell, both subjected to external pressure. We compute the buckling load for both shells using nonlinear buckling analysis using ABAQUS as well as the particular method of RCC-MR that is critiqued in this thesis. For particular imperfection shapes, the buckling load of the torispherical shell and the spherical shell are overpredicted by RCC-MR's third method by factors of about 11/10 and 8/7, respectively. Here we have denied ourselves a safety factor of 2.5 to give the third method benefit of doubt, and our demonstration of nonconservatism is unequivocal. We conclude that the third imperfection quantification method in RCC-MR should be reviewed by competent scientific authorities.

ACKNOWLEDGEMENTS

I am indebted to my advisor, Dr. A. Chatterjee, for his support, encouragement and continuous guidance during my PhD study. I am thankful to him for helping me with prompt, pragmatic and actionable advice whenever I faced any difficulties in my research work. I also thank him for numerous, rich technical discussions about buckling, thin shells, design codes and technical writing that educated me and broadened my outlook in mechanics and design. I thank him for inspiring me with his original thinking and courageous approach to research in mechanics. Last but not least, I thank him for his kindness and generosity.

I thank Dr. A. John Arul for agreeing to be my external advisor towards the end of my PhD and also for all his kind help and support.

I thank all my course instructors in IIT Kanpur for educating me and making learning a joyous and enriching experience.

I thank all my friends in IIT Kanpur and labmates, both PhD and masters students, for support and friendship during my stay in IIT Kanpur.

I am thankful to the IGCAR for allowing me to pursue my PhD at IIT Kanpur. I am particularly grateful to Dr. P. Chellapandi for motivating and encouraging me to pursue the PhD from IIT Kanpur and piloting the necessary administrative approvals for the same. I thank Shri S.D Sajish, Shri S. Jalaldeen, Dr. K. Velusamy and Shri S. Raghupaty in IGCAR for support and encouragement.

Finally, I express my sincere thanks to my family for their unlimited and unconditional support throughout my PhD and life in general.

Contents

Acknowledgements **iv**

List of Figures **x**

List of Tables **xv**

1 Introduction **1**

2 Buckling experiments **13**

2.1 Introduction 13

2.2 Test shell specimen details 18

2.2.1 Material characterization 18

2.2.2 Geometric details 18

2.3 Buckling experiments 25

2.4 Finite element analysis of the tumbler 34

2.5 Conclusions 40

3 On one imperfection estimation method in the design code RCC-MR **42**

3.1 Introduction 42

3.2 Safe buckling load as per RCC-MR 46

3.2.1 Calculation procedure 46

3.3 Shell design case studies 50

3.3.1 Example 1: Nonuniform cylinder with a spherical cap 51

3.3.2 Example 2: Ellipsoidal head 51

3.3.3 Example 3: L-shaped shell under vertical end load 52

3.4 Imperfection quantification 53

3.4.1 Nonuniform cylinder with a spherical cap 54

3.4.2 Ellipsoidal head 57

3.4.3 L-shaped shell under vertical end load . . . 59
3.5 Final safe load estimation . . . 61
3.6 Three ways in which the equation for d_{new} can fail . . . 65
3.7 Discussion and conclusions . . . 66

4 Unequivocally nonconservative results from RCC-MR's third method 68
4.1 Introduction . . . 68
4.2 Bounds on safe loads . . . 71
4.3 Safe buckling load as per RCC-MR-A7 . . . 76
4.4 Linear elastic finite element modeling . . . 78
4.4.1 Geometry . . . 79
4.4.2 Mesh convergence . . . 81
4.5 Safe buckling load as per RCC-MR . . . 83
4.5.1 Hemispherical shell . . . 83
4.5.2 Torispherical shell . . . 85
4.6 Nonlinear buckling analysis . . . 88
4.6.1 Hemispherical shell . . . 88
4.6.2 Torispherical shell . . . 92
4.6.3 Nonlinear analysis . . . 95
4.7 Discussion and conclusions . . . 95

5 Conclusions 98

6 Appendix 102
6.1 P_m and $P_m + P_b$ calculation . . . 102
6.2 Mesh convergence studies . . . 103
6.3 Safe buckling load calculation details . . . 105
6.3.1 Ellipsoidal head . . . 105
6.3.2 L-shaped shell . . . 106
6.4 Verification and validation of nonlinear buckling procedure . . . 107
6.4.1 Geometry . . . 107
6.4.2 Nonlinear analysis . . . 108

Bibliography 108

List of Figures

1.1 The first buckling mode ($n = 3$) of externally pressurized ring obtained using ABAQUS. Solid red line is the buckled shape and dashed black line is the undeformed ring. Displacements are exaggerated. 4

1.2 Left: Perfect cylinder with simply supported edges, under axial compression. Right: Buckling mode obtained using ABAQUS. Displacements are exaggerated. 4

1.3 Left: Perfect cylinder with simply supported edges, under external pressure. Right: Buckling mode ($n = 7$) obtained using ABAQUS. Displacements are exaggerated. 5

2.1 Specimens for experiments. The pen on the left is for scale. 17

2.2 Half cut bowls. 19

2.3 Bowl specimen drawing (all dimensions are in mm). 20

2.4 Profile of bowl with thickness measurement locations. 21

2.5 Mean profile of tumbler. 22

2.6 Profile of tumbler with thickness measurement locations. 23

2.7 Cutting procedure for tensile specimens from bowls. 23

2.8 Left: True stress-strain curve from conical tumbler tensile tests. Right: The shape and location of the tensile test specimen cut from the conical tumbler. 25

2.9 Experimental set up. 26

2.10 Buckled bowl. 26

2.11 Left: three stages of tumbler deformation. The depression caused in the flat base is due to plastic deformation near the periphery. The light source was arranged to aid visibility by reflection. 27

2.12 Load displacement plots for bowl. Left: Initial load displacement plots. Right: Full load displacement plots. The onset of buckling occurs at the first maximum in each load-displacement plot. 28
2.13 Load displacement plots for tumbler. Left: Initial load displacement plots. Right: Full load displacement plots. 28
2.14 Red curves denote the mean and mean ± two standard deviations. Thin blue curves are actual load displacement data. Left: Conical tumbler. Right: Bowl. 29
2.15 Bowl deformed shapes. Left: Minimum buckling load (1.91 kN). Center: Median buckling load (3.39 kN). Right: Maximum buckling load (4.91 kN). The wave numbers observed are 6, 7, and 7. 29
2.16 Empirical CDFs of loads at displacement 0.5 mm, 1 mm, 4 mm and 15 mm for bowls. 30
2.17 Empirical CDFs of loads at displacement 1 mm, 2 mm, 4 mm and 8 mm for tumblers. 31
2.18 Quantile quantile plot of loads with different displacement levels for conical tumbler. 32
2.19 Quantile quantile plot of loads with different displacement levels for bowls. 32
2.20 Buckled shape of bowl tumbler due to pressure load on top surface. 33
2.21 Buckled shape of conical tumbler due to pressure load on top surface. . . . 33
2.22 The variation of collapse load of the conical tumbler with different mesh sizes. 34
2.23 Finite element model of the tumbler and rigid plate. The mesh in fillet radius region is shown. The gap between the plate and tumbler is enhanced for clear depiction. 36
2.24 Finite element model of tumbler, highlighting the loading region where a surface traction is applied in the downward direction. 37
2.25 The load displacement plots for different fillet radii. Left: The load displacement with surface traction. Right: The load displacement with contact loading. 38
2.26 The deformed shape of tumbler for fillet radius 2.4 mm. 39
2.27 Final deformed shape of conical tumbler. Left: Under traction loads. Right: Under contact loads. Displacement are in m. 39

3.1 RCC-MR reduction factor chart for unstable post-buckling behavior, recomputed using our own interpolation program. 50
3.2 A nonuniform cylinder. Loading: external pressure on the spherical cap of radius 3 m. Left: schematic diagram. Right: ABAQUS model with boundary conditions. 52
3.3 Ellipsoidal head. Loading: internal pressure. Left: schematic diagram. Right: ABAQUS model with boundary conditions. 52
3.4 L-shaped shell. Left: circular cross section. Right: swept path used to define geometry. 53
3.5 ABAQUS model of L-shaped shell with boundary conditions and downward-acting end loads. 53
3.6 Top: membrane stresses, and total stresses (von Mises), plotted against curvilinear distance along the shell. Bottom: key locations on the shell. . . 54
3.7 First linear elastic buckling mode of nonuniform cylinder with spherical cap. Displacements are exaggerated. 55
3.8 Results of linear stress analysis of a perturbed geometry with $d/h = 1.5$. . 56
3.9 Membrane stresses, and total stresses (von Mises), plotted as a function of curvilinear distance measured along the shell, for $d/h = 1.5$. 57
3.10 S_d at two locations: the fillet region, and in the buckling region. The horizontal axis depicts imperfection d/h. 57
3.11 von Mises stress distribution in ellipsoidal head. 58
3.12 First buckling mode of ellipsoidal head. 58
3.13 von Mises stress variation along the meridian of ellipsoidal head for perfect geometry. Key locations are marked. 59
3.14 Ellipsoidal head geometry with key locations corresponding to Fig. 3.13. . 59
3.15 von Mises stress variation along the meridian of ellipsoidal head with geometry perturbed with imperfection $d/h = 1.5$. 60
3.16 Ellipsoidal head. Left: Maximum stress S_d against actual d/h. Right: new imperfection value against actual d/h. 60
3.17 von Mises stress distribution in L-shaped shell. 61
3.18 First buckling mode of L-shaped shell. 62
3.19 Top: membrane stresses, and total stresses (von Mises), plotted against curvilinear distance along the shell. Bottom: some key locations on the shell, (rotated view). 63

3.20 von Mises stress along the L-shaped shell (along different lines: one that passes through the point of maximum S_d and one that passes through the point of maximum P_m) for perturbed geometry with $d/h = 1.5$. 64
3.21 L-shaped shell. Left: maximum stress S_d. Right: new imperfection value against actual d/h. 64

4.1 Schematic diagram of hemispherical shell. 79
4.2 ABAQUS model of hemispherical shell with external pressure. 80
4.3 Schematic sketch of torispherical shell. 81
4.4 ABAQUS model of torispherical shell. 81
4.5 Mesh convergence for the hemispherical shell. (a) Strain energy of perfect hemispherical shell. (b) S_d in imperfect hemispherical shell. 82
4.6 Mesh convergence for the torispherical shell. (a) Strain energy of perfect torispherical shell. (b) S_d in imperfect torispherical shell. 82
4.7 First buckling mode of hemispherical shell (displacements (unit: m) are exaggerated, the maximum displacement shown is 187.5 times the shell thickness). 84
4.8 The membrane stress (unit: Pa) in hemispherical shell. 85
4.9 von Mises stress (unit: Pa) distribution in the perturbed hemispherical shell geometry. Displacements are exaggerated: the magnification factor is 500. 85
4.10 First buckling mode of the torispherical shell. Displacement (unit: m) are exaggerated. The maximum displacement is 250 times the shell thickness. . 87
4.11 Membrane stress (unit: Pa) distribution in the perfect torispherical shell. . 87
4.12 von Mises stress (unit: Pa) distribution in the perturbed torispherical shell geometry. 88
4.13 The shape perturbation in the hemispherical shell, exaggerated by a factor of 100. Coordinates x and y are in m. 90
4.14 Perfect (dashed lines) and imperfect hemispherical shells (solid lines), with shell thickness shown. Coordinates x and y are in m. (a) Zoomed region near the pole shows small imperfection. (b) On a larger scale, the two geometries look indistinguishable. 91
4.15 Load displacement plot of the hemispherical shell. 92
4.16 von Mises stress (unit: Pa) distribution in the hemispherical shell at maximum load. 92

4.17 The shape perturbation in the torispherical shell, exaggerated by a factor of 50. Coordinates x and y are in m. 94
4.18 ABAQUS model of imperfect torispherical shell (axisymmetric). 94
4.19 Load displacement plot of the torispherical shell. 95
4.20 von Mises stress (unit: Pa) distribution in the torispherical shell at maximum load. Deformations are exaggerated: the magnification factor is 20. . 96

6.1 Mesh convergence for the nonuniform cylinder with spherical cap. Left: von Mises stress. Right: strain energy. 104
6.2 Mesh convergence for the ellipsoidal head. Left: von Mises stress. Right: strain energy. 104
6.3 Mesh convergence for the L-shaped pipe. Left: von Mises stress. Right: strain energy. 104
6.4 Schematic of the spherical shell used for validating our ABAQUS calculations. 108
6.5 Load displacement plot of the spherical shell with dimple defect at poles. . 108

List of Tables

1.1 Summary of review articles 11
1.2 Summary of review articles 12

2.1 Chemical composition (mass %) of shell specimens. Measurements were made for two specimens each by staff at an external laboratory. The reported numbers are taken as representative. 19
2.2 Dimensions of bowl 20
2.3 Bowl thickness measurements (mm). 21
2.4 Dimensions of truncated conical shells. 22
2.5 Conical shell thickness measurements (mm). 24

Chapter 1

Introduction

A shell is a three-dimensional structure of which two dimensions are significantly larger than the third dimension [1]. In other words, a shell is a structure bounded by two surfaces with a small gap between them. The normal distance between the two surfaces is called the shell thickness, which is very small compared to the other surface dimensions [2]. Shells with a radius to thickness ratio greater than 20 are generally categorized as thin shells [2]. In the nuclear industry, ratios greater than 100 are common.

Thin shells are extensively used in the design of structural components in many engineering applications. Thin shells are routinely used in oil industries, nuclear industries, piping systems, pressure vessels, and aerospace and marine applications. Large-diameter liquid containers in the oil industry, thin walled large containment vessels that house and support the reactor assembly in a nuclear reactor, and cylindrical shells as rocket fuselages are a few examples of such shells. Thin shells have efficient load carrying capacity, high stiffness, and high strength to weight ratio, making them one of the principal structural elements used in the design of industrial structures.

There has been a trend towards thinner shells in modern structural designs due to cost optimization efforts and operational requirements. Sophisticated manufacturing technologies and high strength materials have also accelerated the use of thinner shells in structural

designs. However, thin shells are prone to the risk of buckling failure when loaded with compressive forces. Buckling failure is made more likely by the *thinness* of the shell.

The buckling of a structure is defined as its transition from a stable equilibrium state to an unstable equilibrium state when loaded beyond a critical load. This critical load is called the buckling load of the structure [3]. For example, consider a thin plate subjected to in-plane forces. When the forces are small, the plate is in stable equilibrium. Any application and subsequent removal of small lateral perturbations on the plate results in small lateral displacements and reversal to the original (stable) configuration. But if in-plane forces are increased further and further, then the plate may attain a state where an application of a tiny perturbation leads to excessively large and possibly irreversible deformations [2]. This phenomenon is called buckling. The deformation behaviour of shells after the buckling load has been exceeded is often briefly referred to as just "post-buckling" [4].

Bushnell [5] discussed shell buckling in terms of membrane and bending strain energy stored in the shell. The in-plane stiffness of a thin shell is several times higher than its flexural stiffness. Hence, thin shells can absorb a large amount of in-plane strain energy without any significant deformations but undergo large deformation for the same amount of flexural strain energy [5]. Thus, thin shells are efficient when in-plane stresses sustain the external load. However, when the loads on such structures are increased, the equilibrium may lose stability beyond a critical load. In that case, the structure may switch to an alternate stable equilibrium configuration, converting its in-plane strain energy into flexural strain energy, resulting in large deflections and failure of the structure.

For simple geometries subjected to compressive loads, simple analytical formulas of buckling load are available in the books and literature. The buckling load formulas for some example geometries are given below.

The buckling load (P_{cr}) of an axially loaded, simply supported beam [3] is

$$P_{cr} = \frac{\pi^2 EI}{L^2}.$$

Here EI and L are the flexural rigidity and length of the beam, respectively.

For an externally pressurized circular ring (or a thin cylinder of very short length), the buckling load per unit length [3] is

$$q_{cr} = \frac{3EI}{r^3},$$

where EI and r are the flexural rigidity and radius of the ring. Figure 1.1 shows the buckling mode of a ring under external pressure.

For a long, simply supported cylinder at ends and subjected to axial compressive load, the buckling stress σ_{cr} [3] is

$$\sigma_{cr} = \frac{Eh}{r\sqrt{3(1-\nu^2)}},$$

where E, ν, h and r are elastic modulus, Poisson's ratio, thickness and radius of the cylindrical shell, respectively. Figure 1.2 shows the first buckling mode of a long, simply supported, axially loaded cylindrical shell, obtained using ABAQUS. Similarly, the buckling pressure (p_{cr}) of a simply supported, externally pressurized thin cylinder [3] is

$$p_{cr} = \frac{Eh^3(n^2-1)}{12r^3(1-\nu^2)},$$

where $n \geq 2$ is the circumferential mode number of the cylindrical shell. Figure 1.3 shows the buckling mode of a simply supported, externally pressurized cylindrical shell, obtained using ABAQUS. Though the buckling loads of simple shell geometries subjected to simple loads are easy to compute, the design against buckling of practical shells subjected to complex loads is a challenging activity.

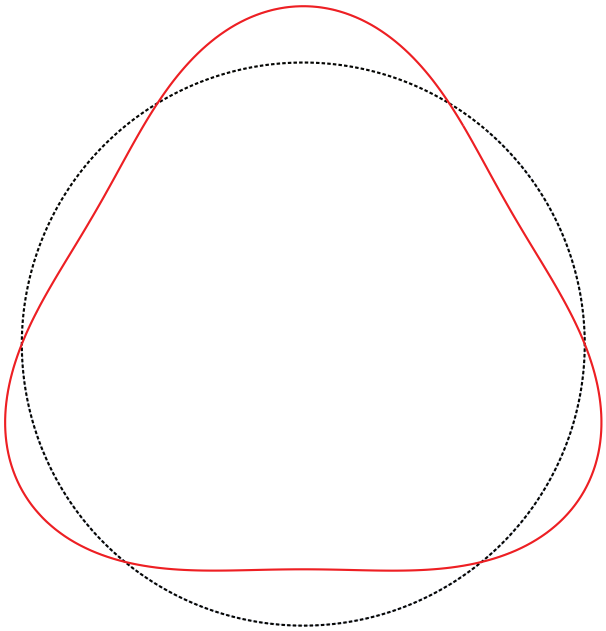

Figure 1.1: The first buckling mode ($n = 3$) of externally pressurized ring obtained using ABAQUS. Solid red line is the buckled shape and dashed black line is the undeformed ring. Displacements are exaggerated.

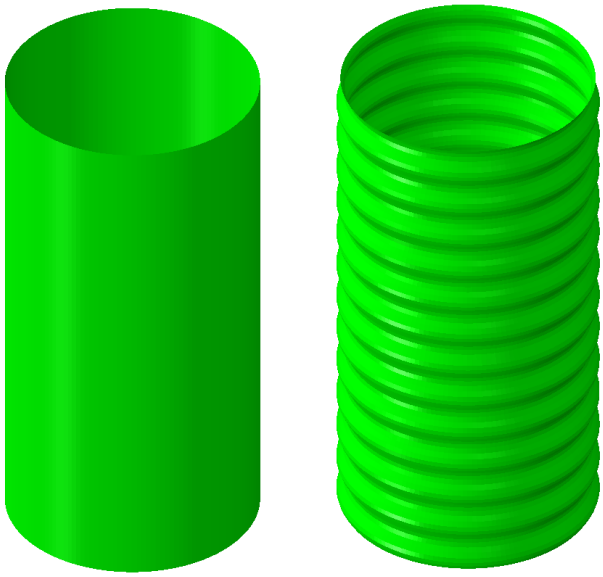

Figure 1.2: Left: Perfect cylinder with simply supported edges, under axial compression. Right: Buckling mode obtained using ABAQUS. Displacements are exaggerated.

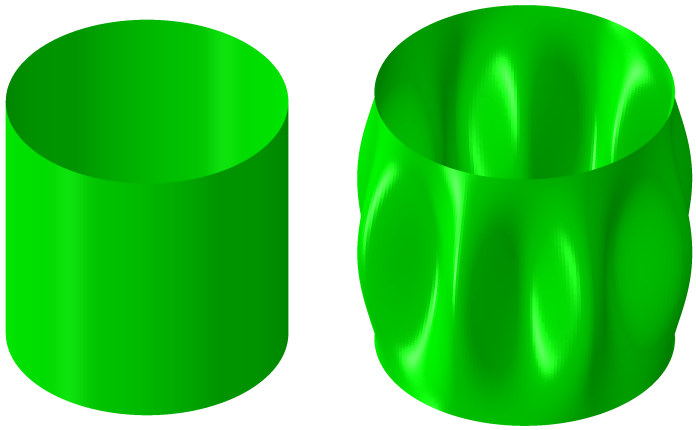

Figure 1.3: Left: Perfect cylinder with simply supported edges, under external pressure. Right: Buckling mode ($n = 7$) obtained using ABAQUS. Displacements are exaggerated.

Thin shell design against buckling is challenging because many real shells buckle at a fraction of their theoretical buckling loads. This is because geometric imperfection, among other factors, reduces the actual buckling load of real shells significantly from the estimated theoretical buckling load. In the earliest studies, von Karman and Tsien [6] showed a large discrepancy between the classical theoretical buckling loads of perfect shells and shells with small imperfections. In some early reported experiments, the buckling load observed was within 15-50 % of the classical buckling load [7]. Tennyson [8] and Almroth *et al.* [9] independently showed that the buckling loads of thin cylinders could be controlled by controlling initial imperfection. Babcock *et al.* [10, 11] conducted experimental and theoretical buckling investigations on axially loaded cylindrical shells and attributed discrepancies between theoretical and experimental buckling load to imperfections as well as end constraints (assumptions about boundary conditions). Calladine *et al.* [12, 13] discovered less-than-expected scatter in experimental results due to deliberately introduced and existing imperfections. They attributed the lack of scatter in experimental buckling load to the absence of statistically indeterminate boundary condition.

Simitses [7] presented a brief overview of the history of shell buckling and attributed the difference between theoretical and experimental buckling load to pre-buckling defor-

mations, in-plane boundary conditions, and initial geometric imperfections. The author also discussed efforts by researchers to create an imperfection data bank. The primary aim of creating an imperfection data bank is to make all the imperfection data identically normalized and provide this data to future users to compute accurate shell buckling loads using nonlinear shell theories and advanced computational tools. Thus, the important role of imperfections in shell buckling is well known.

Some detailed literature reviews of shell buckling studies can be found in [14, 15, 16]. A brief summary of these articles is presented in table 1.1 and 1.2.

We now turn to shell design, where the physical shell does not exist yet, and the exact imperfection shape it will have is not known. At best, some bounds on the geometrical size of the imperfection may be available. In such situations, the accepted industrial practice is to use design codes.

For the nuclear industry, the RCC-MR and ASME codes give detailed procedures to compute safe buckling load for shells using knockdown factors computed using geometric imperfection in the shell and also its material properties. The knockdown factors are then applied to the structure's linear buckling load to compute a safe buckling load. ASME code case N-284 provides knockdown factors α and η to account for the reduction in the classical buckling load due to imperfection and plasticity, respectively [17]. Design code RCC-MR provides single knockdown factor charts for a given nominal geometry and an imperfection estimate [18]. For the ASME code, knockdown factors are derived from an extensive experimental program discussed in [19]. For RCC-MR, reduction factor charts were generated by the writers of the code by solving a canonical beam bending problem with an unstable post-buckling response followed by an offbeat and clever analysis [20]. For shells with unstable post-buckling behaviour, RCC-MR is less conservative than the ASME code [20], which means that in some design situations, a "safe design" is still possible based on RCC-MR but not based on the ASME code. We emphasize that in

various nonlinear elastic-plastic simulations, we have not found an example where the safe load computed using RCC-MR is unsafe, except for designs based on the single clause that is critiqued in this thesis. It is for this reason that we continue to hold RCC-MR in high regard even as we critique one clause in it.

Two salient points about the state of the art of thin shell buckling research require particular attention. First, the contribution of uncertainties in loading and boundary conditions to the buckling load of the shell is not discussed in buckling design procedures. Second, the number of buckling experiments conducted or reported for a specific shell geometry and loading are typically low because large-sample buckling experiments for large structures are difficult to conduct and prohibitively expensive as well.

The non-availability of large-sample buckling experiments impedes our empirical understanding of the statistical variability in shell buckling experiments and the factors contributing to that variability. Such large-sample buckling experiments can lead to better insights into shell mechanics, and also help to assess the safety factors in design codes like RCC-MR which are used to design safety critical shell structures.

In the Indian nuclear industry, RCC-MR is extensively used to design fast breeder reactor components. In comparison to ASME, RCC-MR allows buckling design at comparatively high temperature (up to 973 K) and allows the buckling design of a wide range of geometrical shapes [18]. The importance of accommodating high temperature and general shape is great for design of nuclear reactor components. Some examples of the application of RCC-MR in the buckling design of fast breeder reactor components are reported in [21, 22, 23, 24, 25, 26, 27]. Thus, RCC-MR is the mainstay of design activities in the Indian fast breeder nuclear industry and some other places as well.

RCC-MR allows three imperfection estimation methods to compute an imperfection quantity, subsequently used to compute safe buckling loads. The computed safe buckling load is sensitive to the imperfection estimate used. Of these three methods, the third

method allows a lower imperfection estimate than other methods, leading to a higher value of the predicted safe buckling load, i.e., a less conservative design. Since the RCC-MR code is widely used, and the resulting design has vast safety implications, a detailed examination of its imperfection estimation methods has both theoretical and practical value.

This thesis has two distinct parts. In the first part, we carry out large-sample buckling experiments on two small shells and study the statistical variability in large-sample buckling experiments. We also study the interaction of geometry and contact loading and its impact on the buckling load in these experiments. In the second part of the thesis, following up on these experiments, we examine the third imperfection estimation method in the design code RCC-MR with several design examples, and assess its non-conservativeness.

Both parts of the thesis are connected due to the underlying theme of trying to understand and improve the design of thin shells against buckling in the presence of imperfections. The experiments show the variability actually observed in tests of notionally identical specimens, and the critique of the design code deals with the situation where the shell in question does not physically exist yet and a computational design is being done. Both parts talk to the designer. The first part shows some aspect of reality and the second part critiques some aspect of accepted procedure.

We now present a more detailed outline of the thesis.

In chapter 2, we present one hundred buckling experiments each, for two different shell geometries. One is a dome-like shell with a flat base (a bowl), and the other is a truncated cone with a flat base (a tumbler). The test shells are industrially mass-produced, inexpensive, and made of stainless steel. The buckling experiments were carried out by axially compressing these shell specimens between two rigid plates. The experimental load-displacement plots of 100 bowl specimens show variation in buckling load by a factor of two and stable postbuckling response. The experimental load-displacement curves for

tumbler specimens show variations of as much as a factor of 5 and unstable postbuckling response for higher displacements.

Further, we present axisymmetric finite element simulations to explain the large scatter observed in the buckling load of the conical shell in the initial phase of postbuckling behaviour. Our central finding is this: the interaction of contact loads and large curvature in the vicinity of the contact edge leads to higher variability in the load-displacement behaviour. We present two sets of simulations to establish this finding. In one set of simulations, loads are directly applied to a predetermined region, and in the second set of simulations, loads are applied through contact with a rigid plate. The simulations with contact show approximately twice as much sensitivity to geometric imperfections. The importance of contact loading in the vicinity of large curvature, leading to the large variability in failure load, may guide new assessments of safety factors in buckling as laid down in design codes. The work presented in this chapter has been published in [28].

In chapter 3, we examine the third of three imperfection estimation methods given in RCC-MR. We critique the third method of imperfection estimation using three design examples. Our first example is a nonuniform cylindrical shell closed with a spherical endcap subjected to external pressure. Our second example is a cylinder with an ellipsoidal head subjected to internal pressure. Our final example is an L-shaped pipe subjected to an end load. In all three design examples, the imperfection computed using the third method is surprisingly small compared to the actual value used for computations (e.g., 25 times smaller). In two cases, the result is insensitive to the actual geometrical imperfection. Using the results of these design examples, we explain how a designer can be misled by the third method in three different ways. The work presented in this chapter has been published in [29].

In chapter 4, we prove unequivocal nonconservatism in the third imperfection estimation method using two design examples. The two thin shell designs considered are a

spherical shell and a torispherical shell, both subjected to external pressure. The shell walls are thin enough so that plasticity is absent during structural collapse. For specific imperfection shapes, we show that RCC-MR's third method overpredicts the collapse load of the imperfect shells by a factor of about 8/7 and 11/10, respectively. Our calculation does not include a further safety factor of 2.5, which we have denied ourselves here to give the third method the benefit of the doubt. We conclude that the third imperfection quantification method in RCC-MR should be reviewed. The work presented in this chapter has been published in [30].

Chapter 5 presents some final discussion and concludes the thesis.

Table 1.1: Summary of review articles

Reference	Summary and comment
Hutchinson and Koiter, 1970	Summary: The authors reviewed many numerical calculations using the large-deflection behaviour of perfect shells to compute the minimum load sustained by a practical shell. The authors concluded that this approach was not useful. They then discussed the initial post-buckling theory and pointed out that the existence of a large number of simultaneous unstable equilibrium branches explains the imperfection sensitivity of shells. The authors also noted that applying the initial post-buckling theory could explain the wide scatter in the experimental data. Comment: Theoretical and experimental investigations of imperfection sensitivity and the degree to which it affects buckling load can be done for special structures. But in the design of complicated shapes, especially using the linear buckling analysis approach allowed by design codes, the unstable equilibrium branches obviously will not be computed. So it is clear that the design code and its method of incorporating imperfection plays a critical role in the safety of the design.
Teng, 1996	Summary: The author noted that many factors, including boundary conditions, contribute to the variability in the buckling loads of shells. However, the role and need for accurate modelling of boundary conditions had not been discussed in buckling design procedures. Despite significant development in the computational modelling of shell buckling, developing a reliable design procedure to convert numerically computed buckling load to safe design load is still challenging. Using a design procedure based on linear analysis and reduction factors is easy to implement but it is difficult to obtain reduction factors for different loading and support conditions. The author advocated developing statistically-based imperfection models for particular classes of shells fabricated by the same process. Comment: The accurate modelling of boundary conditions indeed has not been discussed in buckling design procedures. The buckling design procedure based on linear analysis is easier to use. In fact, it is how design is currently done using either RCC-MR or ASME codes. Though there may be other non-linear methods for the safe buckling load calculation that are superior in principle, the fact of the matter is that these design codes exist and are widely used in industrial design. Therefore, we must either eliminate the codes or improve them. As long as these codes exist, industry will use them. The author's recommendation for developing statistically-based models for particular classes of shells has not yet been incorporated into general practice. However, the first experimental study of this paper is an effort in this direction. We have carried out a large number of tests on thin-walled shells fabricated by the same process. But instead of extensive measurements of real geometric imperfection, we have attempted an experimental characterisation of the variability of buckling behaviour.

Table 1.2: Summary of review articles

Reference	Summary and comment
Schmidt, 2000	Summary: The author discussed two different approaches to simulate the effect of imperfection on shell buckling. One approach is based on Koiter's initial post-buckling theory, in which the buckling behaviour of an imperfect structure is deduced from the properties of a perfect structure. The second approach is to study the behaviour of an imperfect shell by studying imperfect shells as they are, with geometric imperfections modelled with the geometry. The author cautions that modelled imperfections are still a substitute for actual imperfections, which are unknown, and appropriate care shall be taken to model the worst imperfection scenario. The author stressed the continuing need for statistics-focused buckling tests. Comment: The second approach to simulate the effect of imperfection on shell buckling behaviour, discussed by the author, can be easily implemented using advanced numerical procedures available in commercial finite element packages. However, using this approach to compute a safe buckling load for practical shells is challenging. As the author cautions, modelled imperfection shapes at the design stage are still a substitute for actual imperfection in the shell, which is yet to be manufactured. The modeled shape may not be the most damaging imperfection shape.

Chapter 2

Buckling experiments

The work presented in this thesis begins with an experimental buckling study of thin shell geometries. The material in this chapter has been published in [28].

2.1 Introduction

Uncertainty and associated risk in performance of structural systems have been an area of active research (e.g., [31, 32, 33]). In this chapter we consider statistical variability in the buckling load and postbuckling behaviors of two small thin walled shell structures.

Thin walled structures are important because they are widely used in structural designs. Various technological and economic factors like the availability of high strength materials, high stiffness to weight ratio, cost optimization pressures, and specific application areas like aerospace, marine structures, automobiles, and nuclear reactors, have led to widespread use of thin walled structures. There are many thin walled substructures or components used in a variety of engineering structures as well. In low cost and mass produced thin walled structures, due to inevitable imperfections, the variability in postbuckling behavior remains imperfectly understood.

von Karman and Tsien [6] first showed that a large discrepancy can exist between

the buckling load calculated from linear shell theory and the actual buckling load of a real structure with small imperfections. Babcock Jr. [10] carried out initial-buckling tests on 34 cylindrical shells and compared results with the theoretical buckling load. He attributed the discrepancies observed to imperfections, end constraints, and uncertain boundary conditions. In later studies, the roles of plasticity, boundary conditions, and residual stresses have been recognized in contributing to variability in buckling loads. Details on shell buckling experiments for various type of shell geometries can be found in the book by Arbocz *et al.* [34].

We now present a brief literature of review of probabilistic method in shell buckling and experimental buckling studies.

Chryssanthopoulos [35] presented the review of the probabilistic method applied to thin plate and shell buckling problems and studied the effect of geometric imperfection and residual stress on buckling problems using reliability analysis. The author noted that reliability methods in the domain of buckling could be as effective as deterministic methods.

Kameshwar *et al.* [36] presented an imperfection model for buckling of above-ground storage tanks based on measured imperfection data for probabilistic buckling analysis. The authors found that change in mean buckling capacity is small for smaller imperfection values and large for higher imperfection values.

Gotsulyak *et al.* [37] carried out a nonlinear stability analysis of an imperfect cylindrical shell under external pressure using a probabilistic approach. The presented methodology allowed calculation of the reliability of imperfect shells for a given initial imperfection and a given load and determining maximum permissible loads for imperfect shells.

V. Papadopoulos *et al.* [38] studied the effect of elastic modulus, thickness and geometric imperfection on the buckling of an axially loaded cylinder. The authors assumed non-Gaussian distribution for elastic modulus and thickness and Gaussian distribution

for initial imperfection. The properties of these distributions were determined by experimental measurements. The authors showed that the choice of probability distribution function strongly influences both shape and extreme values of resulting buckling load distribution.

M. T. Roudsari *et al.* [39] carried out the probabilistic buckling analysis for a double vaulted space structure. The authors studied the effect of geometric and length imperfection on the reliability and collapse of such structures. The reliability and collapse load of space structures was found to be very sensitive to geometric imperfection. The authors also concluded that the type of support or boundary conditions strongly influence the imperfection sensitivity of space structures.

Arbocz *et al.* [40] carried out probabilistic buckling analysis to compute reliability-based knock-down factor for cylindrical shells loaded in compression and compared them to the knock-down factors obtained using the lower bound design curve. The authors showed that reliability-based, less conservative knock-down factors could be developed from a database containing measurements of elastic modulus, geometry, and the initial imperfection of shells. The author argued that probabilistic-based buckling design is useful for designs where cost and weight optimization of shells is necessary. This approach helps generate more rational but safe knock-down factors.

Tankova *et al.* [41] presented a review of safety assessment methodologies of structural design rules in the European structural design code (EN 1990). The authors discussed a procedure to derive partial safety factors based on the framework provided by EN 1990 and presented a safety assessment of stability design rules.

Lee *et al.* [42] investigated the effect of dimple imperfection on the buckling of the externally pressurized spherical shell. The investigation included sixty buckling experiments in which both magnitude and shape of imperfection in spherical shells were designed and controlled. The authors derived and presented the relation between knock-down factors

and the imperfection magnitudes in spherical shells from experimental investigations. The authors also presented the buckling results from finite element simulations and shell theory solutions, which were in excellent agreement with experimental results. The authors noted that knock-down factors become independent of imperfection magnitude beyond a critical value, observed similarly in the lower limit of the ensemble of historic buckling data. Hence the authors argue that current lower limit curves can be replaced with more accurate knock-down factors derived using the presented approach.

Ifayefunmi [43] carried out buckling experiments and accompanying finite element simulations of the axially loaded thick cylinders. The author reported good agreement between simulations and experimental results. However, the number of shells tested was relatively small (5 numbers).

As is clear from the forgoing review, the role of imperfection in the buckling behaviors of shells has received considerable attention in the past, however the sample sizes of shell buckling experiments have generally been modest. To understand the statistical variability and effects of various parameters on buckling loads, it seems useful to conduct a large number of experiments for a given geometry, say 100 experiments for notionally identical shells. In such studies, for simplicity as well as more precise control on experimental conditions, relatively smaller shell specimens are attractive. As a step in this direction, in this chapter we present 100 buckling experiments[1] each, for two different thin shell geometries, to obtain a detailed statistical view of the buckling load-displacement curves of these thin shells. Our immediate goal is to report on the variability observed; and our longer term goal is to prompt detailed simulations that attempt to quantify uncertainty and imperfection sensitivity in such shells through detailed nonlinear finite element simulations.

Our shells are industrially produced, inexpensive, made of stainless steel, and easily available in India for common use. One shell is dome-like with a flat base (a bowl), and

[1] 100 is an order of magnitude greater than the typical sample size in previous studies.

is stable after buckling. The other is a truncated cone with a flat base (a tumbler), and has unstable post-buckling behavior. Figure 2.1 shows the test shells used in buckling experiments. Physical dimensions of the tests shells are on the order of ten centimeters and the wall thickness is below 1 mm. The small size, easy dimensional and material characterization, and low cost of our test shells facilitate experiments in large numbers, providing a detailed statistical picture that was not available so far. We anticipate that qualitative features of the variability observed in the postbuckling behaviors of these two shells may lead to improved understanding of such behavior in other shell structures in general.

Figure 2.1: Specimens for experiments. The pen on the left is for scale.

We note that our test shells have small variations in geometric (height, diameter, thickness) and material parameters (yield stress). We will duly report on these variations below.

Among these variations, we have noted in particular that large scatter in load-displacement plots can occur due to interaction between contact loading and high geometric curvature. To demonstrate, we have carried out two sets of finite element analyses of the tumbler with varying radii in the high curvature region. In one case we have included the contact nonlinearity, and in another case we have applied the load as a surface traction on a predetermined region. The former indeed shows greater sensitivity to geometric imperfections.

The rest of this chapter is organized as follows. A detailed geometric, material and microstructure characterization for test specimens is presented in section 2.2. In section 2.3, buckling test set up details and test results are presented. In section 2.4 we present details and results of finite element modelling. Finally, in section 2.5 we present some concluding remarks.

2.2 Test shell specimen details

2.2.1 Material characterization

Each set of shell specimens was obtained from a single vendor in one single purchase. This effectively assures us that all specimens were manufactured by the same process, in the same factory, and within a short space of time. In subsequent discussion, the specimens are considered as notionally identical.

Optical spectroscopy based chemical analysis[2] for both shell materials showed them to be similar to stainless steel UNS S20430, an austenitic stainless steel with an FCC crystal structure. Average chemical composition estimates of the shells (two samples each) are given in table 2.1. X-ray diffraction analysis showed that the crystal structure is FCC (details omitted).

2.2.2 Geometric details

We now describe the geometry of the bowl and the tumbler.

First the profiles of several bowls were measured, initially by studying long focal length photographs and then taking vertical cross sections (electrical discharge machining (EDM); see figure 2.2), and finally by external diameter measurement using Vernier calipers. Wall thicknesses were measured from cut specimens using a screw gauge. Figure

[2]At Microlab in Chennai; see `http://www.microlabchennai.com/` .

Table 2.1: Chemical composition (mass %) of shell specimens. Measurements were made for two specimens each by staff at an external laboratory. The reported numbers are taken as representative.

Element (%)	Bowl	Tumbler
Carbon	0.16 ± 0.01	0.11 ± 0.005
Silicon	0.49 ± 0.03	0.39 ± 0.02
Manganese	10.41 ± 0.06	10.46 ± 0.06
Phosphorus	0.06 ± 0.005	0.06 ± 0.007
Sulphur	0.04 ± 0.01	0.005 ± 0.003
Chromium	13.19 ± 0.05	14.30 ± 0.005
Nickel	0.78 ± 0.06	0.60 ± 0.012
Copper	2.08 ± 0.08	1.84 ± 0.03

2.3 shows a schematic sketch of the bowl. The dimension W varies from 0.9 mm to 1.0 mm. The mean, standard deviation and standard error of measured Z values are 0.91 mm, 0.06 mm and 0.027 mm, respectively. The dimension W of the flat portion varies from 4.5 to 5.1 mm. The mean, standard deviation and standard error of measured W values are 4.8 mm, 0.26 mm and 0.1 mm, respectively. The dimension Y of the flat portion varies from 2.7 to 3.35 mm. The mean, standard deviation and standard error of measured Y values are 2.9 mm, 0.29 mm and 0.12 mm, respectively. Details of geometric measurements are presented in table 2.2.

Figure 2.2: Half cut bowls.

The thickness of the bowl was measured at six locations shown in figure 2.4. Table 2.3 shows measured values for five bowls. Measurements were taken with a hand-held micrometer with a notional least count of 0.001 mm; however, due to small differences in contact conditions and ratchet tightening, we think the actual error in measurement may

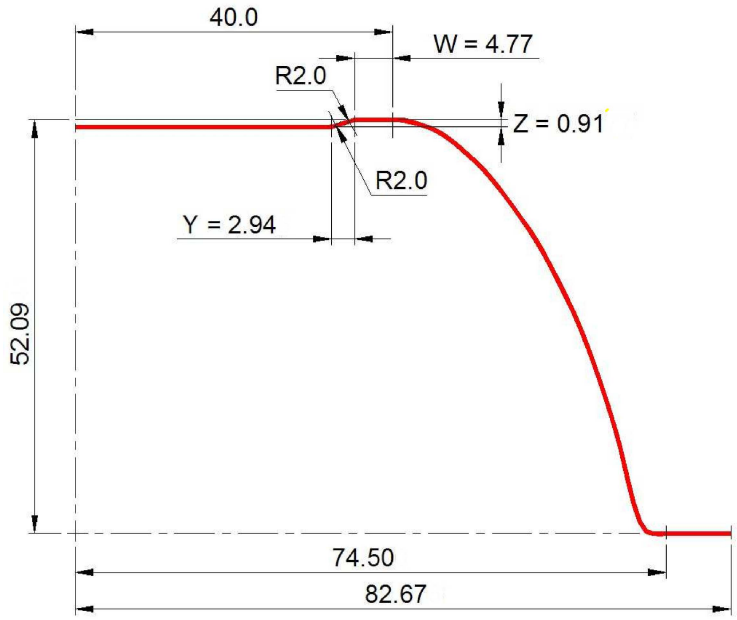

Figure 2.3: Bowl specimen drawing (all dimensions are in mm).

Table 2.2: Dimensions of bowl

Specimen no.	W (mm)	Y (mm)	Z (mm)
1	4.47	3.35	0.90
2	4.69	2.80	0.82
3	5.10	2.86	0.94
4	4.81	3.26	1.02
5	4.53	2.70	0.89
6	5.02	2.70	0.90

be somewhat larger, although less than 10 microns. The standard error at all points is about 0.002 mm.

The geometry of the tumblers was relatively simpler. Geometry parameters of eleven tumblers (diameter at top and bottom; and height) were measured using Vernier calipers; see table 2.4. The mean, standard deviation and standard error of the measured value of tumbler height are 111.3 mm, 1.57 mm and 0.47 mm, respectively. The mean, standard deviation and standard error of the measured value of tumbler top diameter are 45.50 mm, 0.29 mm and 0.09 mm, respectively. The mean, standard deviation and standard error of the measured value of tumbler bottom diameter are 71.54 mm, 0.27 mm and 0.08

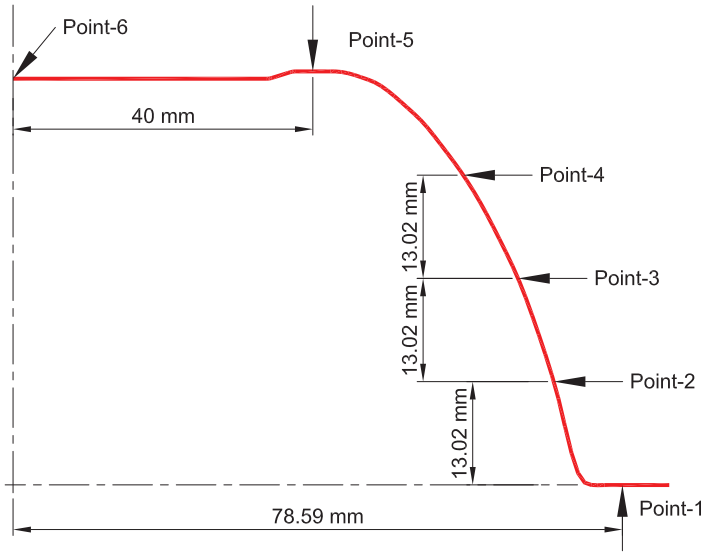

Figure 2.4: Profile of bowl with thickness measurement locations.

Table 2.3: Bowl thickness measurements (mm).

	Bowl 1	Bowl 2	Bowl 3	Bowl 4	Bowl 5	Mean	Standard deviation
Point 1	0.257	0.245	0.256	0.256	0.260	0.255	0.006
Point 2	0.232	0.235	0.240	0.246	0.238	0.238	0.005
Point 3	0.221	0.231	0.235	0.234	0.231	0.230	0.006
Point 4	0.225	0.217	0.226	0.226	0.230	0.225	0.005
Point 5	0.239	0.232	0.235	0.239	0.243	0.238	0.004
Point 6	0.246	0.231	0.236	0.243	0.245	0.240	0.003

mm, respectively. Figure 2.5 shows the geometry with averaged measured dimensions.

The wall thickness of the tumbler was measured at 8 locations as shown in figure 2.6. Tumbler thicknesses are given in table 2.5. We observe that the wall thickness varies with location, although the thickness variation is small across specimens at any given location. The standard error of measurements at point-1 is 0.012 mm and for all other points is about 0.004 mm.

The yield strengths of the shell materials were evaluated by routine tensile tests carried out on a universal testing machine. Tensile specimens were prepared as follows. For the bowls, EDM was first used to cut out portions larger than the final specimens. The cut portions were not flat, but the radius of curvature was large. A fixture with two flat plates

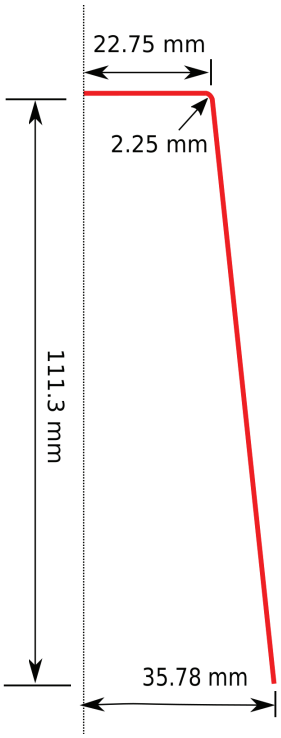

Figure 2.5: Mean profile of tumbler.

Table 2.4: Dimensions of truncated conical shells.

Specimen no.	Height (mm)	Bottom dia. (mm)	Top dia. (mm)
1	108.60	71.30	45.27
2	110.60	71.89	45.37
3	109.40	71.24	45.43
4	112.45	71.60	45.10
5	110.22	71.57	45.87
6	111.20	71.20	45.59
7	111.70	71.60	45.74
8	112.80	72.10	45.81
9	114.17	71.40	45.78
10	111.70	71.57	45.58
11	111.32	71.43	45.00

was fabricated, with a cutout of test specimen dimensions (figure 2.7). After clamping the cut portions in the fixture, EDM was used to cut out the final test specimens. The slight bend in the test specimens straightened out easily, and had a negligible effect on the estimated yield strength. Specimens from the tumbler were easier to cut (longitudinal

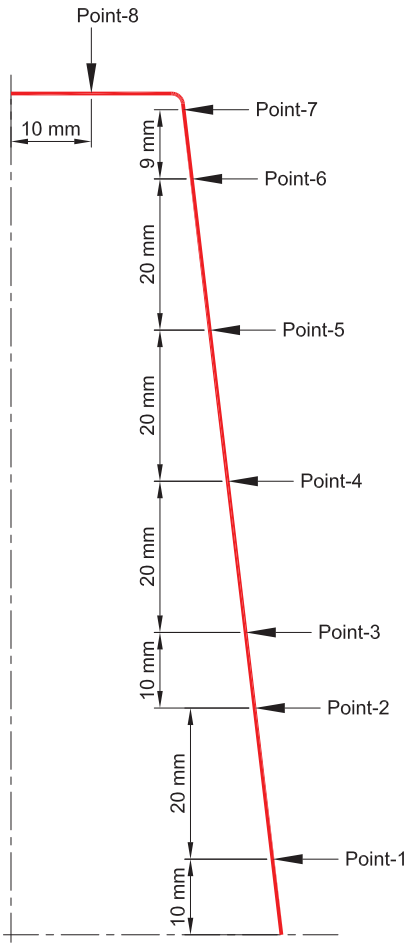

Figure 2.6: Profile of tumbler with thickness measurement locations.

direction; EDM; details omitted).

From simple tensile tests on three specimens from the bowls, the yield stress corresponding to 0.2 percent plastic strain was 830 MPa, 794 MPa and 800 MPa. The mean and standard deviation of measured yield stress is 808 MPa and 19.28 MPa.

Corresponding values from four specimens from the tumblers gave yield stresses of 1321 MPa, 1219 MPa, 1465.6 MPa and 1312.6 MPa. The mean and standard deviation

Figure 2.7: Cutting procedure for tensile specimens from bowls.

Table 2.5: Conical shell thickness measurements (mm).

	Conical-1	Conical-2	Conical-3	Conical-4	Mean	Standard deviation
Point-1	0.482	0.507	0.488	0.536	0.503	0.024
Point-2	0.270	0.275	0.253	0.267	0.266	0.009
Point-3	0.266	0.254	0.246	0.265	0.258	0.009
Point-4	0.254	0.248	0.240	0.247	0.247	0.006
Point-5	0.263	0.264	0.258	0.260	0.261	0.003
Point-6	0.383	0.382	0.399	0.381	0.386	0.008
Point-7	0.461	0.463	0.465	0.472	0.465	0.005
Point-8	0.670	0.673	0.663	0.680	0.672	0.007

of measured yield stress is 1329 MPa and 101.80 MPa. Note that these tensile test specimens were from relatively thinner (and more work-hardened) portions of the shells. The tops and bottoms of the tumblers had greater wall thicknesses, and were therefore less stretched and less work hardened. Figure 2.8 (left) shows the true stress-strain curve of the tensile specimen cut from the conical tumbler top. Figure 2.8 (right) shows the shape and location of the tensile test specimen cut from the conical tumbler for tensile tests.

The Young's modulus of the shell material is 207 GPa, estimated using a simple bending test. A thin strip is cut from the conical tumbler for the bending test. One end of the thin strip is kept fixed, and a load of known magnitude is applied to the other. The displacement at the loaded end is noted. Subsequently, an FEA analysis of the bending test is carried out. In the FEA analysis, the elastic modulus is varied such that displacement at the loaded end is the same as measured in the test. The final elastic modulus for which both displacements become equal is the elastic modulus of the specimen.

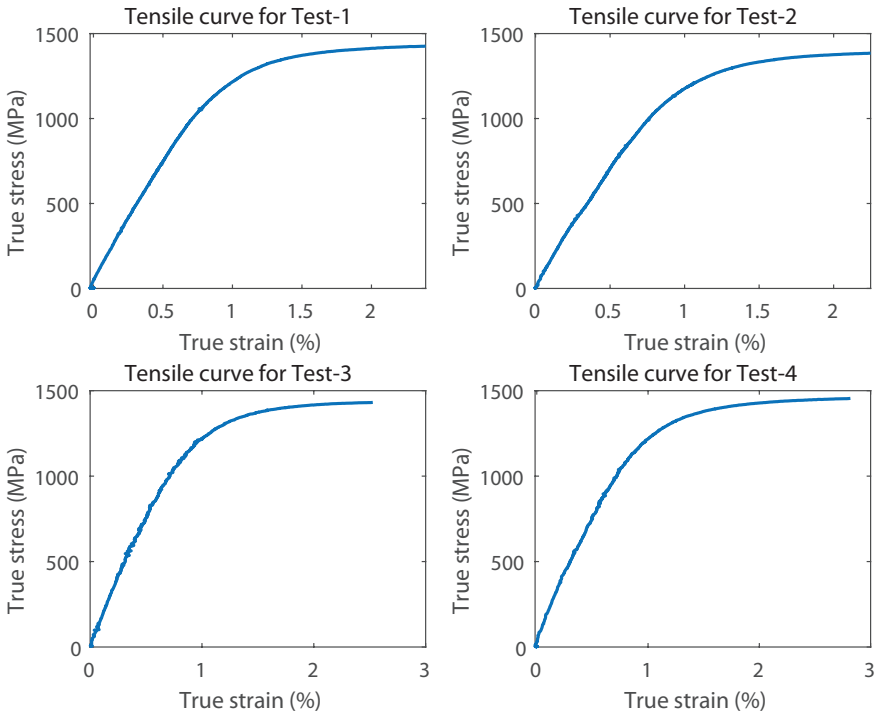

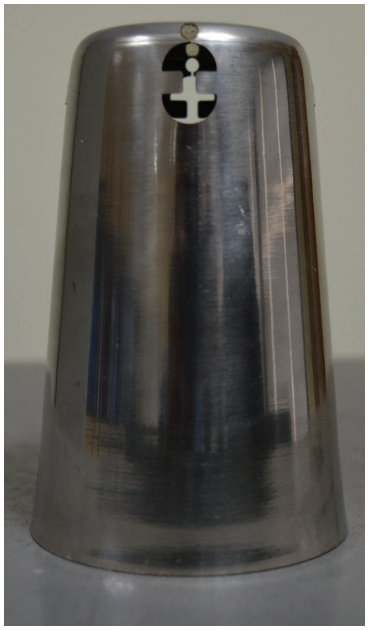

Figure 2.8: Left: True stress-strain curve from conical tumbler tensile tests. Right: The shape and location of the tensile test specimen cut from the conical tumbler.

2.3 Buckling experiments

Buckling experiments were carried out at room temperature on a universal testing machine (UTM). The shell specimen was placed, open side down, on a flat rigid circular plate at the bottom, and a vertical compressive load was applied through another flat rigid plate at a constant displacement rate. It was soon clear that the bowls had more regular behavior than the tumblers. Accordingly, for subsequent tests, the displacement rate used for the tumblers was 1 mm per minute, while for bowls the rate was 3 mm per minute. Figure 2.9 shows the experimental set up for the bowl and tumbler specimens. Speeded up (16 times) video of several buckling tests is available at `youtu.be/76KgjyJSg9I`.

During the experiments, as may be seen in the video, the bowls initially deform axisymmetrically until an initial peak load is reached. Nonaxisymmetric buckling modes appear later at the top of the bowl. Figure 2.10 shows an intermediate stage for one

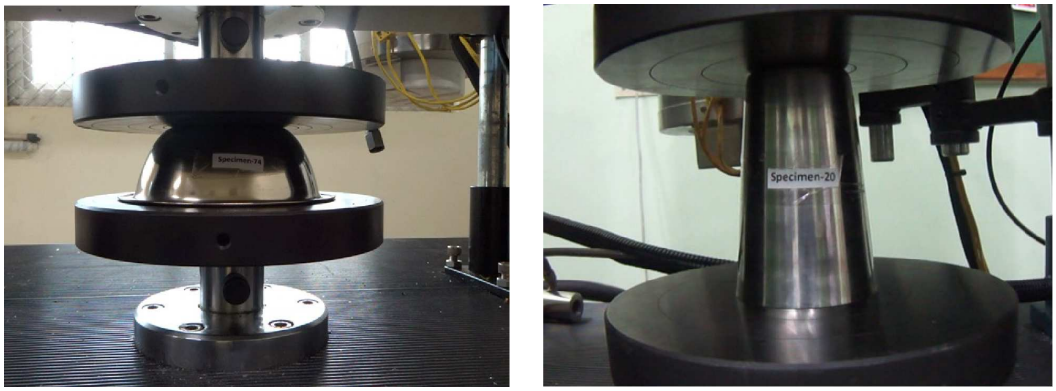

Figure 2.9: Experimental set up.

bowl. The bowls continue to deform in the same buckling mode in the post-buckling regime as the load is increased. The depression in the central region of the top of the bowl is not because there are loads acting there. As the bowl is pressed between rigid plates, loads act on the raised portion, along the rim.

Figure 2.10: Buckled bowl.

In the buckling of the tumblers, an axisymmetric depression initially is formed at the top (see figure 2.11); subsequently, an axisymmetric lateral bulge appears near the top (watch the video); and finally, nonaxisymmetric buckling occurs. This type of symmetry breaking bifurcation is not surprising. For example, in purely elastic buckling of a thin walled cylinder, a large number of such bifurcations exist off a main axisymmetric solution branch. See Wohlever and Healey [44] and especially figure 6 therein.

There is a significant difference between the bowls and tumblers. The bowls are stable

Figure 2.11: Left: three stages of tumbler deformation. The depression caused in the flat base is due to plastic deformation near the periphery. The light source was arranged to aid visibility by reflection.

post-buckling, and the tumblers are unstable. Figure 2.12 and figure 2.13 shows load versus displacement plots for the bowls and tumblers (100 specimens each) respectively. To make uniform the initial displacement point in the load displacement curves, all the graphs were made to pass through the same point at a load of 0.2 kN load for the bowl, and 0.35 kN for the tumbler. The relative difference in stability between the two types of specimens is clearly seen. The experiments would be visually more dramatic if the tests were load controlled instead of displacement controlled; however, in displacement controlled mode, intermediate points are obtained more reliably.

In figure 2.12 (left), the scatter in the load displacement curves slightly exceeds a factor of 2, with an overall rising tendency. This is stable behavior. In contrast, the scatter is about a factor of 5 for the tumblers, with an overall tendency to drop dramatically from intermediate maxima. Both sets show behavior in the elastoplastic regime, which is relevant to both small shells at ordinary temperatures and large shells at elevated temperatures.

The scatter in load displacement curves is represented with $\mu + 2\sigma$ and $\mu - 2\sigma$ curves. Here μ and σ are the mean and the standard deviation of all the loads at a particular displacement. Figure 2.14 shows load displacement plots along with $\mu + 2\sigma$ and $\mu - 2\sigma$

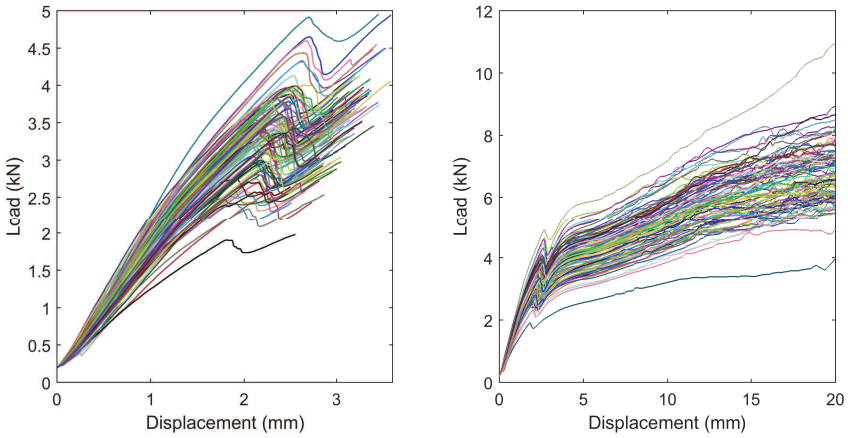

Figure 2.12: Load displacement plots for bowl. Left: Initial load displacement plots. Right: Full load displacement plots. The onset of buckling occurs at the first maximum in each load-displacement plot.

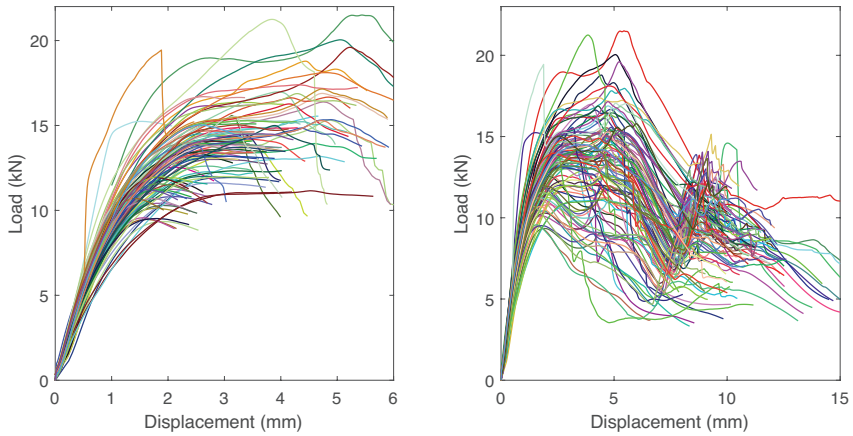

Figure 2.13: Load displacement plots for tumbler. Left: Initial load displacement plots. Right: Full load displacement plots.

curves. For computing μ and σ for tumbler, 96 curves were retained and 4 curves that terminated early were discarded.

For the tumblers, the load displacement curves show clearly the need for care with structures which are unstable post-buckling. The load can rise to high levels (e.g., above 21 kN) or dip to relatively much lower levels (e.g., below 4 kN). Some of the load displacement curves have nearly vertical portions, which are traced easily in a displacement controlled experiment but would cause a dynamic snap-through event in a load controlled experiment. Even in our slow experiments, some specimens produced a "thud" like sound

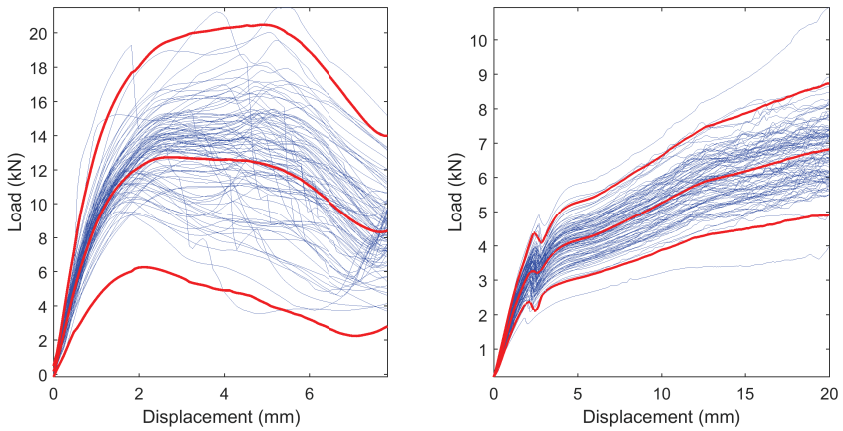

Figure 2.14: Red curves denote the mean and mean ± two standard deviations. Thin blue curves are actual load displacement data. Left: Conical tumbler. Right: Bowl.

at an intermediate point, indicating a small dynamic instability.

We have randomly selected the load-displacement results of 50 conical tumblers and found that the mean and standard deviation of peak loads is 14.41 kN and 2.24 kN, respectively. The mean and standard deviation of peak loads of all 100 samples are 14.25 kN and 2.48 kN, respectively. For the bowl, the mean and standard deviation of initial peak loads for randomly drawn 50 samples are 3.37 kN and 0.55 kN, respectively. For all 100 test samples, the mean and standard deviation of initial peak loads are 3.40 kN and 0.53 kN, respectively. Figure 2.15 shows the deformed bowl shape of bowl with minimum buckling load, median buckling load and maximum buckling load.

Figure 2.15: Bowl deformed shapes. Left: Minimum buckling load (1.91 kN). Center: Median buckling load (3.39 kN). Right: Maximum buckling load (4.91 kN). The wave numbers observed are 6, 7, and 7.

We now briefly report on the nature of the underlying distribution in loads attained at particular values of the displacement in the load-displacement curves. Empirical cumulative distribution function (CDF) plots of load for specific values of displacement are shown below. Figure 2.16 shows the empirical CDF plots of loads at displacements equal to 0.5 mm, 1 mm, 4 mm and 15 mm for bowls. Similarly, empirical CDF plots of loads at displacements equal to 1 mm, 2 mm, 4 mm and 8 mm are plotted for the tumblers, in figure 2.17. The CDF plots appear S-shaped. They may be approximated as normal. The 1 mm plot for the tumbler looks slightly asymmetrical, but is not conclusively different from normal based on a simple statistical test (details not reported here).

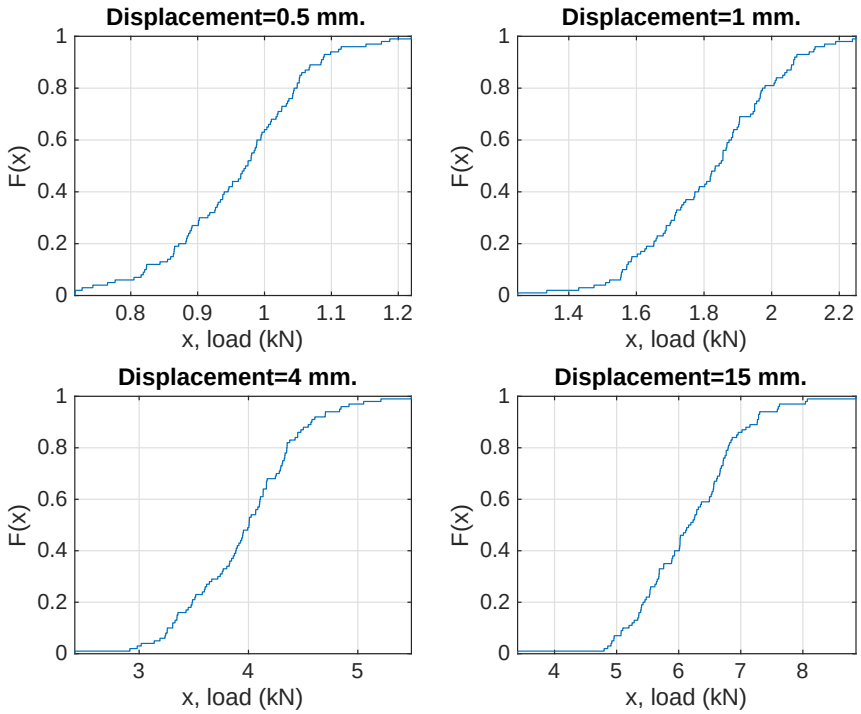

Figure 2.16: Empirical CDFs of loads at displacement 0.5 mm, 1 mm, 4 mm and 15 mm for bowls.

The figure 2.18 shows the normal quantile-quantile (Q-Q) plot of loads at four displacement levels for the conical tumbler. The points in the Q-Q plot for displacement 1 mm, 2 mm and 8 mm show some scatter at the ends of the straight line, indicating the a deviation from purely normal distribution in loads. The points in the Q-Q plot for 4

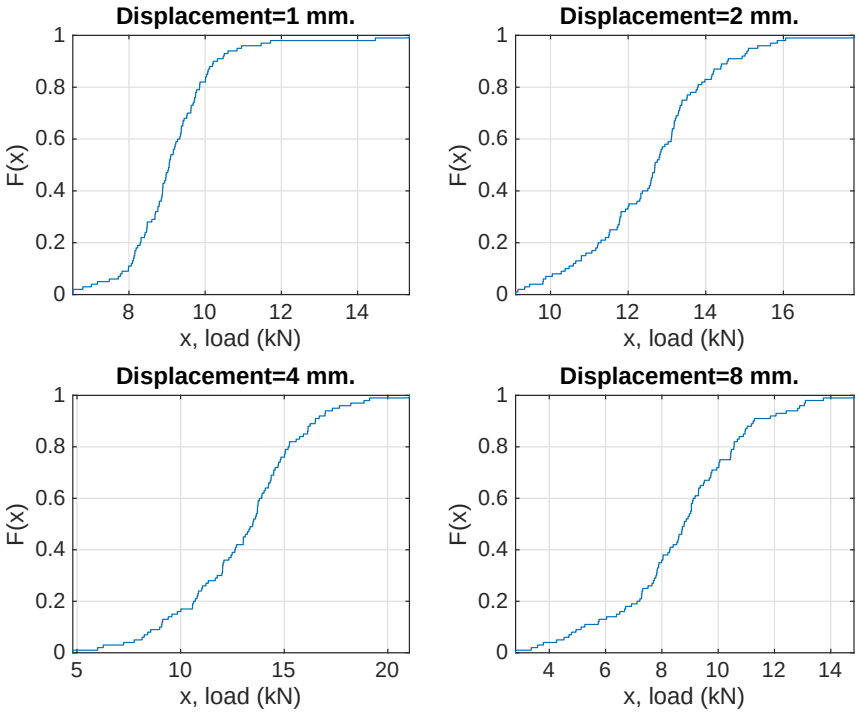

Figure 2.17: Empirical CDFs of loads at displacement 1 mm, 2 mm, 4 mm and 8 mm for tumblers.

mm displacement have less scatter at the ends. However, the middle of the plot is fairly linear.

The figure 2.19 shows the Q-Q plot of loads at four displacement levels for the bowl. The points in the Q-Q plot for displacements 1 mm, 2 mm, and 4 mm lie almost on a straight line, suggesting a normal distribution of loads at these displacement levels. The points in the Q-Q plot of load at displacement 15 mm have significant deviation at the ends.

Figures 2.20 and 2.21 show the buckling mode of the bowl and conical tumbler shell under compressive load on the top surface, respectively. The figure 2.20 and 2.21 show that the buckling mode obtained using linear buckling analysis is different from the buckling mode seen in the buckling experiments. The difference in the buckling mode shape from linear analysis and experiments is due to the limitation of linear buckling analysis, which cannot incorporate contact constraints imposed on specimens in the buckling experiments.

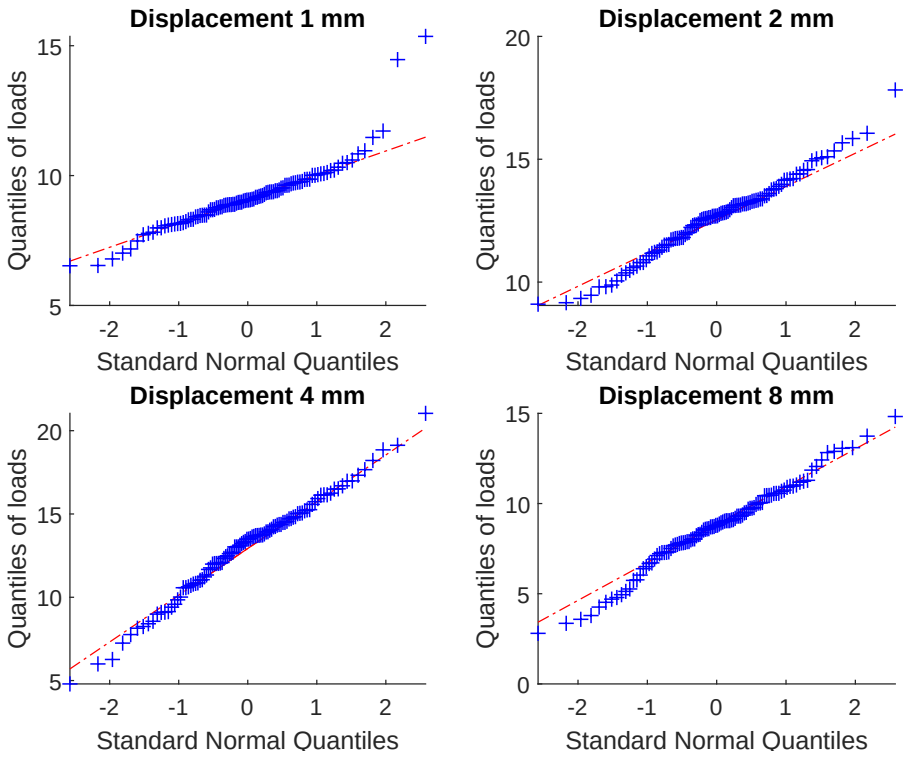

Figure 2.18: Quantile quantile plot of loads with different displacement levels for conical tumbler.

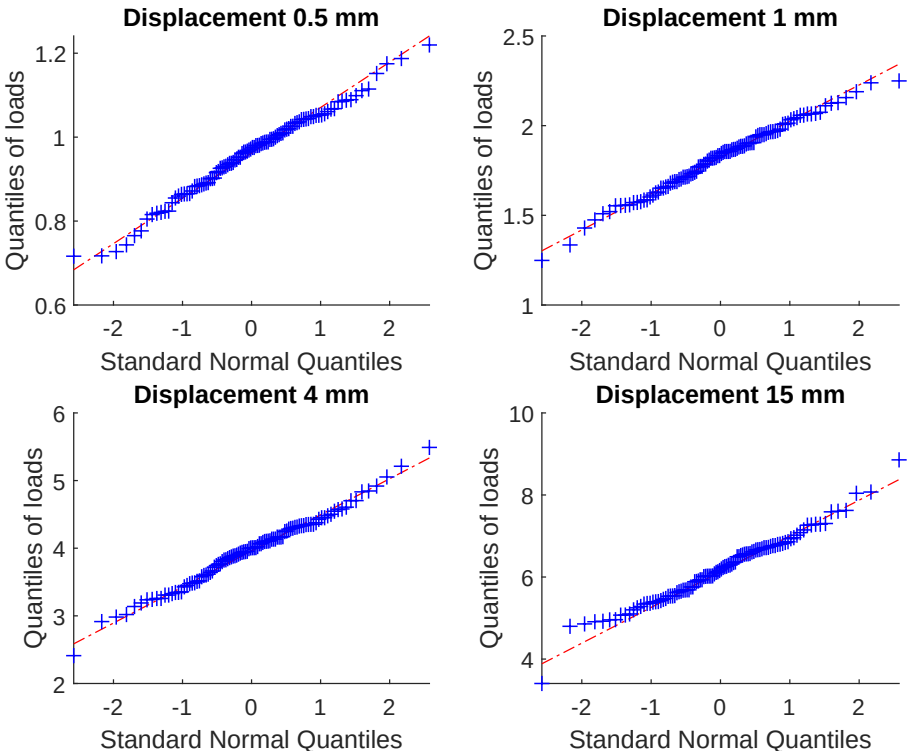

Figure 2.19: Quantile quantile plot of loads with different displacement levels for bowls.

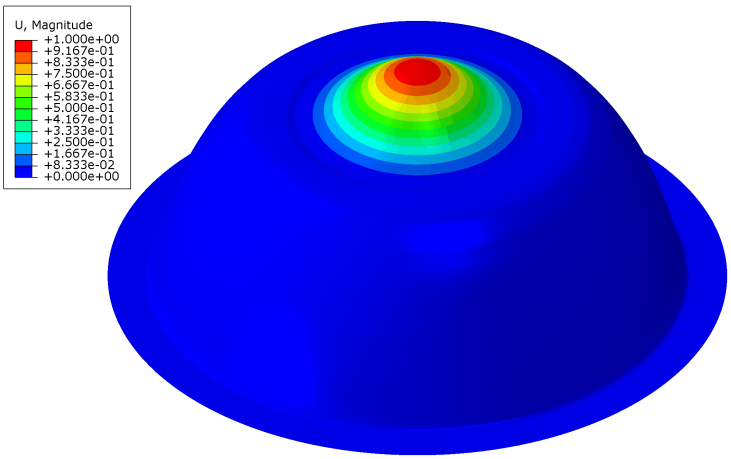

Figure 2.20: Buckled shape of bowl tumbler due to pressure load on top surface.

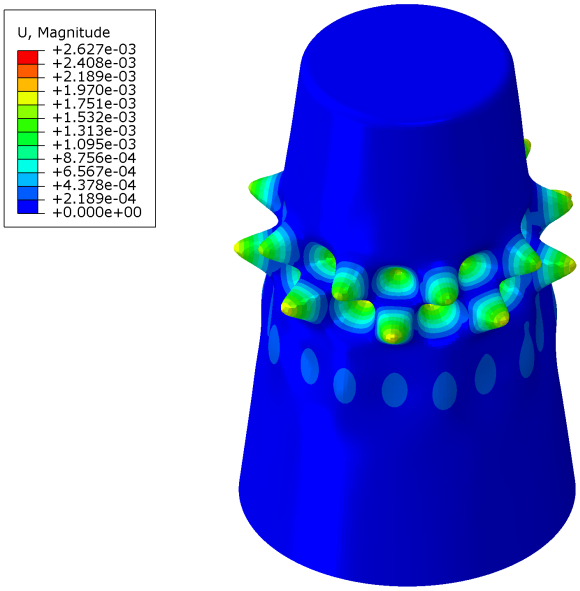

Figure 2.21: Buckled shape of conical tumbler due to pressure load on top surface.

2.4 Finite element analysis of the tumbler

As discussed above, the tumblers exhibit unstable postbuckling behaviour and large scatter in load displacement plots. In this section we use finite element simulations to show that a significant portion of the large variability of initial peak loads can be attributed to a geometrical interaction between the contact loading and variability in the fillet radius. We first carry out elastoplastic analysis of the tumbler under contact loading with a coefficient of friction 0.3, for different fillet radii. For comparison, we then also carry out elastoplastic analyses of the tumbler under surface traction loads for the same set of fillet radii.

Since the tumbler undergoes axisymmetric yielding before undergoing a symmetry breaking bifurcation (as amply demonstrated in the videos mentioned above), here the tumbler is modeled using the axisymmetric solid element in the commercial finite element package ABAQUS. The tumbler dimensions considered for analyses are averaged dimensions: see figure 2.5 and table 2.5. The fillet radius for both sets of analyses is allowed to vary from 1.8 mm to 3 mm.

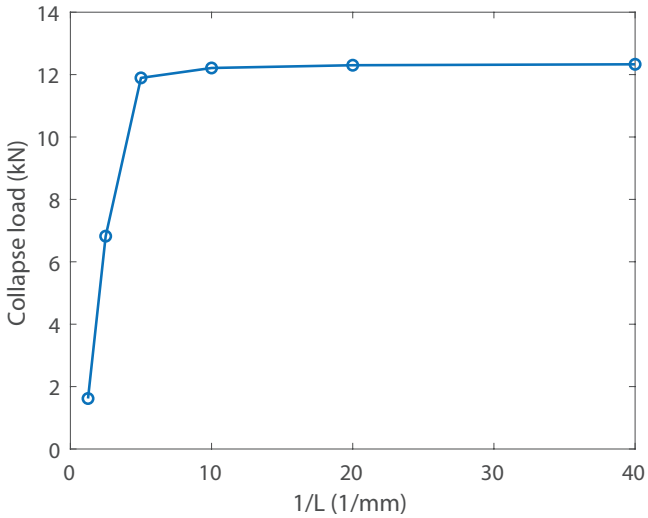

Figure 2.22: The variation of collapse load of the conical tumbler with different mesh sizes.

We have modelled the tumbler using first order, reduced integration axisymmetric solid element CAX4R to avoid shear and volumetric locking [45]. Mesh convergence studies were carried out for the conical tumbler with a fillet radius of 2.4 mm and subjected to traction load. Successive finite element meshes with element sizes (L) of 0.8 mm, 0.4 mm, 0.2 mm, 0.1 mm, 0.05 mm, and 0.025 mm were prepared, and collapse loads were computed for each mesh size. Figure 2.22 shows the variation of the collapse load for different element sizes. Beyond the element length of 0.2 mm, the change in the collapse load is very small. Based on these mesh convergence studies, we have chosen an element size of 0.05 mm (11 elements across thickness) for our simulations to avoid hourglass modes in simulation results.[3]

In the buckling experiments, the conical tumbler undergoes axisymmetric yielding before transitioning to a non-axis symmetric buckling mode. In a design activity, this observed axis-symmetric yielding would be considered the onset of failure, and the corresponding load is the buckling or failure load. Hence, the final (highest) load attained (horizontal part of the load-displacement curve) in our finite element simulations is the buckling load. As we are modelling the tumbler with axisymmetric elements and an elastic-perfectly-plastic material model, only the initial part of the conical tumbler deformation is captured. The subsequent non-axisymmetric deformation modes are not captured, restricting the validity of the simulation to the initial post-buckling regime.

The bottom edge of the tumbler is fixed for both sets of simulations. The elastic modulus of the tumbler is 200 GPa in all cases. We have used an elastic, perfect plastic material model with a yield stress of 700 MPa, chosen to match the overall average buckling load observed in experiments. The geometric nonlinearity is included in the analysis. The elastic perfect plastic behavior is modeled using the von Mises yield criterion and isotropic hardening.

[3]To avoid hourglass modes, ABAQUS recommends artificial strain energy to less than 2% of total internal energy [45], which in our case is 0.007%, hence the risk of hourglassing in the elements is ruled out.

In the first set of analyses, the top plate is modeled as a rigid body and a vertically downward displacement rate is imposed on it, at 1 mm/min. Contact is modeled between the top plate and tumbler. Figure 2.23 shows the corresponding finite element model and mesh in the fillet radius region. The thickness variation is shown in fillet region mesh.

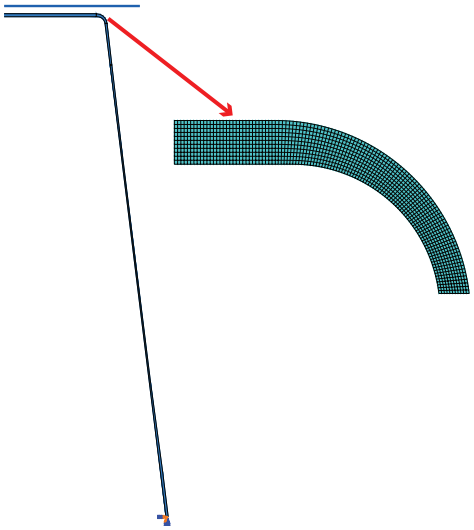

Figure 2.23: Finite element model of the tumbler and rigid plate. The mesh in fillet radius region is shown. The gap between the plate and tumbler is enhanced for clear depiction.

In the second set of analyses, surface traction in the downward direction is applied on a narrow concentric region of radius 21.25 mm and a width of 0.5 mm. The applied load is then increased pseudostatically until the load-displacement curve reaches zero slope. Figure 2.24 shows the ABAQUS model of the tumbler, showing the loading region.

We now present the simulation results. See figure 2.25. Since the second set of simulations actually show smaller variation in load displacement curves, we present them on the left to provide a basis for comparison. Figure 2.25 (left) shows the load displacement plot of the tumbler under surface traction with different fillet radii. It can be seen that peak load varies from 11.65 kN to 13.21 kN for the fillet radii considered. Figure 2.25 (right) shows the load displacement plots for the tumbler under contact loading. Here the variation is approximately twice as large for the same radii. The peak load varies from 11.15 kN to 17.10 kN. The contact based simulation also runs longer because of numerical

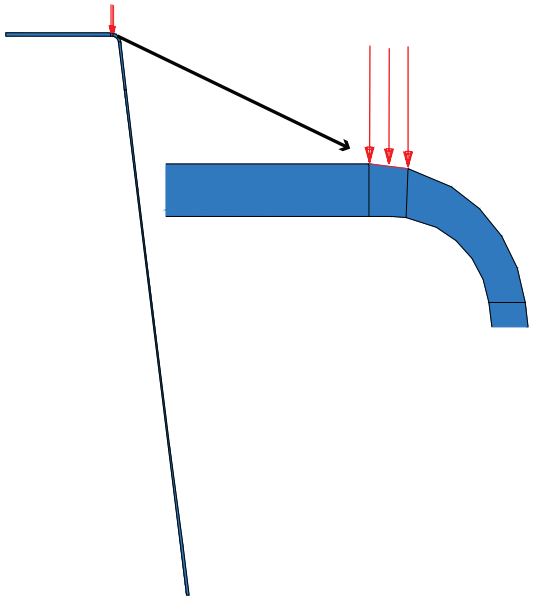

Figure 2.24: Finite element model of tumbler, highlighting the loading region where a surface traction is applied in the downward direction.

algorithmic issues that are not of interest here.

Figure 2.25 shows the contradictory trend of buckling load variation with respect to fillet radius in contact simulations and simulations with traction load. A likely reason for the observed reversal in the trend is as follows. There are two effects at play in this problem. The first effect is the stress amplification due to a small fillet radius at some location due to known tractions applied at another location. Due to this effect, in the traction-loading case, the geometry with the smaller fillet radius yields at a lower load, explaining the observed trend. The second effect is that of movement of the point of application of the load as yielding proceeds. This effect is missing in the traction loading case and strong in the contact loading case. If some initial local yielding in the small fillet region occurs under contact loading, then the contact circle is enlarged, and the edge of contact moves closer to the conical surface. In such a changed geometry, it is possible for the conical portion to sustain a higher load in compression without bending. The fillet portion which has yielded has by then become flat and is pressed against the rigid loading plate, so it deforms no more and takes up no further load. In this way, initial yielding

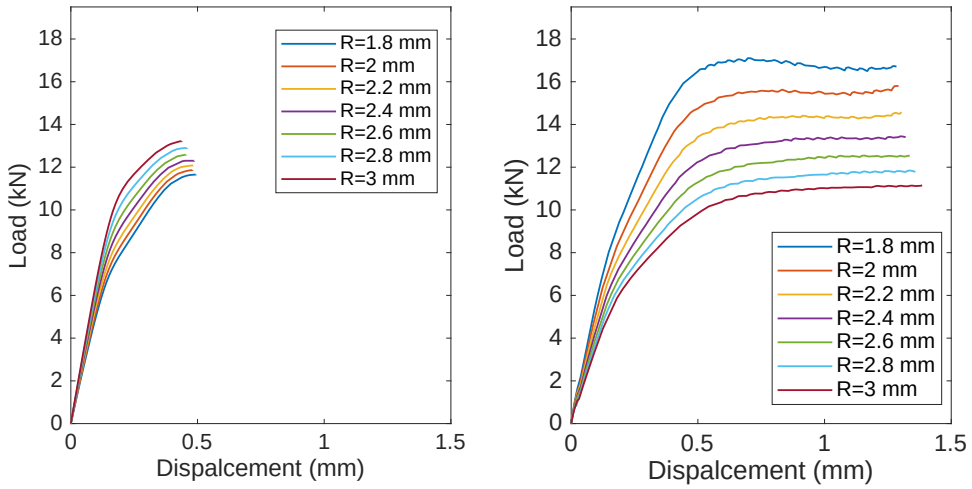

Figure 2.25: The load displacement plots for different fillet radii. Left: The load displacement with surface traction. Right: The load displacement with contact loading.

near the smaller fillet radius leads to greater protection from bending failure as loading progresses. This explains the observed reversal in the trend.

Figure 2.26 shows the deformed shape of the tumbler for a fillet radius 2.4 mm, to show that the loading does occur on an annular region. It is just that, aided by the proximity of a region with sharp curvature, the annular region of contact moves during the post-buckling phase. Figure 2.27 shows the final deformed shape of the conical tumbler under traction and contact load.

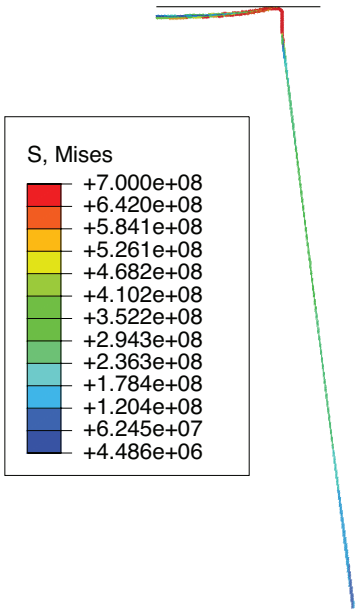

Figure 2.26: The deformed shape of tumbler for fillet radius 2.4 mm.

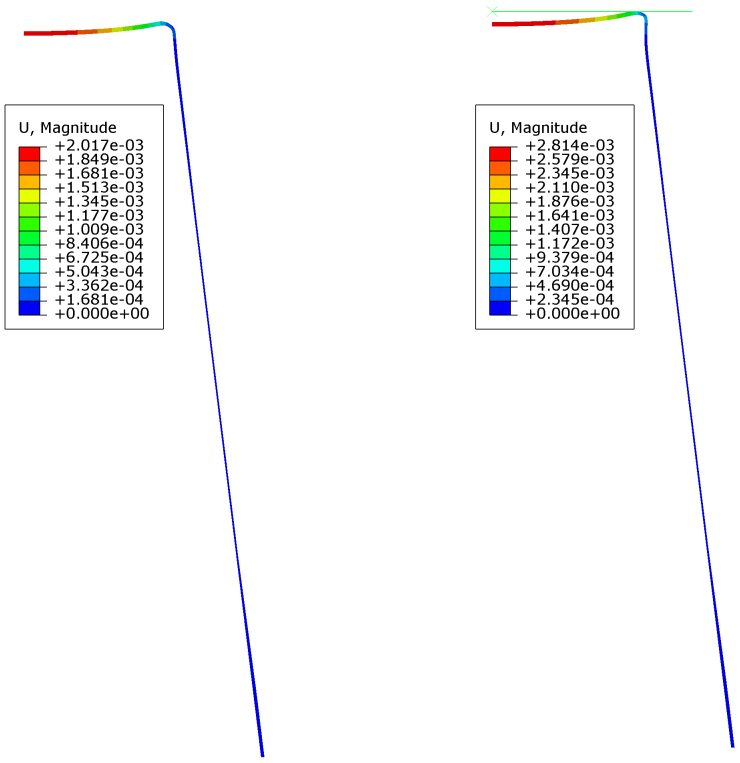

Figure 2.27: Final deformed shape of conical tumbler. Left: Under traction loads. Right: Under contact loads. Displacement are in m.

2.5 Conclusions

Buckling of thin shell structures is a long standing complex problem. Large-sample buckling experiments on notionally identical thin shell structures provide insight into statistical variability of the post-buckling behaviors of such structures. To that end, 100 experiments each, for two different shell geometries, have been reported in this chapter. There is large scatter in post-buckling behaviors. The scatter is about a factor of 2 for the bowl, which shows stable post buckling response; and about a factor of 5 for the tumbler, which shows unstable post buckling response.

Axisymmetric finite element simulations of the early part of the post-buckling response indicate that the application of loads through contact close to a region of high curvature could potentially lead to some kind of interaction, with increased sensitivity to variations in the fillet radius. We hope that more detailed three dimensional simulations in future work may yield further insights into the factors that control the surprisingly large variability in load-displacement behaviors observed experimentally in the present work.

If indeed there is a sensitivity-enhancing geometric interaction between the contact region and the region of high curvature, then such interactions could potentially be incorporated or guarded against in design codes. Design codes such as RCC-MR [18], which are widely used in the nuclear industry, presently allow a linear analysis based design calculation where the prescribed knockdown factors do not incorporate such interactions. In this way, the work presented in this chapter has potential safety implications that may warrant reexamination of some parts of codes like RCC-MR.

The buckling experiments presented in this chapter also highlight a potential pitfall of using linear analysis for the design of shells with unstable post-buckling behaviour (depicted in figure 2.13), subjected to low-probability earthquake loads during operation. During an earthquake, a shell with unstable post-buckling behaviour is subjected to transient displacements and may switch from stable equilibrium with higher sustained load to

unstable equilibrium, resulting in the collapse of the structure. Future work may produce simple and practical design methods that accommodate the insights obtained from this study.

Chapter 3

On one imperfection estimation method in the design code RCC-MR

We now turn to RCC-MR, which is the mainstay of structural design in the Indian nuclear industry. The work presented in this chapter has been published in [29].

3.1 Introduction

Commercial sodium-cooled fast breeder reactors are typically designed to operate for more than 40 years. Factors like high temperature damage through creep-fatigue, frequent thermal transients, low operating pressure, cost reduction efforts, and manufacturing difficulties, all together lead to large and thin reactor assembly components. Engineering design of such structures, specifically against buckling, must consider many factors including lowered yield stress at high operating temperatures, large radius to thickness ratios, and the well known sensitivity to geometric imperfections in such thin shells. Codes that govern the design of such structures must be examined widely within the general scientific community, since even a remote possibility of nonconservative designs has profound implications for human safety.

The French code RCC-MR (within RCC-MRx 2012, see e.g., [18, 46]) is used predominantly to design shell structures against buckling at high temperatures. It is the most important code available for buckling design of structures operating at high temperatures (from 293 K to 973 K). For example, the ASME Boiler and Pressure Vessel Code Section VIII Division 2 provides design rules for operating temperature limited to 753 K. Thus, the importance of RCC-MR for structural design in the nuclear industry is great.

RCC-MR prescribes, among other things, how geometrical imperfection and yield stress can be used to compute reduction or knockdown factors on computed linear elastic buckling loads to ensure safety. Specifically, RCC-MR appendix A7 provides detailed procedures for calculating the safe buckling loads of thin shells, accounting for both plasticity and imperfection, through purely elastic analysis [18]. The background formulation and experimental validation of the buckling design procedure given in RCC-MR is readily available [20].

The research literature on shell buckling is vast. We have presented a summary of review articles [7, 14, 15, 16], in chapter 1. But note that matters are not fully settled, and new studies with new loads, analyses, and experiments keep appearing.

Zhang *et al.* [47] carried out buckling experiments and finite element simulations on ten externally pressurized spherical shells. The authors found significant variation in buckling load among shells of the same radius to thickness, and experimental buckling load was about 15.0–24.5 % of classical buckling load [47]. The finite element results using elastic-plastic material properties agreed well with the experimental results. The author concluded that the realistic buckling load of the spherical shell could be obtained using FEM simulations, with measured geometric properties and elastic perfectly plastic material model.

Tall *et al.* [48] carried out the numerical simulations of spherical shells under external pressure and circumferential shear. Buckling capacity curves were generated for individual

loadings using different analysis levels defined in European code ECCS. Buckling load for the spherical shell under external pressure became independent of imperfection magnitude beyond a critical value, as also discussed in [42].

Zhu *et al.* [49] carried out the experimental and numerical investigation of the cylindrical shell under external pressure for different length to radius ratios. The authors reported excellent agreement between experimental and nonlinear buckling simulations results. The experimental buckling loads were also compared against two design codes used to design the pressure hulls of deep manned submersibles (China Classification Society and American Bureau of Shipping). It was reported that though the predicted safe load by both codes is smaller than experimental buckling loads, significant variation among safe loads predicted by both codes still exists.

Given the great complexity of the set of all possible shell geometries, loads, and resulting behaviors, a design code allows a structural designer to proceed with relatively less detailed effort and greater confidence at the same time, provided the designer follows certain simplified procedures and checks that are laid down in the code.

We emphasize that the design code offers multiple approaches to a designer, and the designer is free to adopt any of them. For this reason, although alternative design procedures based on elasto-plastic analysis are available as well, they are not relevant to the present chapter. Here we focus on those parts of the code that deal with elastic analysis based design. Such design is indeed carried out in the nuclear industry.

Geometric imperfection is a *critical* parameter in safe buckling load calculation. Within elastic analysis based design, RCC-MR specifies three different methods to obtain imperfection values from given manufacturing tolerances. We will duly describe all three methods, which require some technical details, a little later in the chapter. The key point here is that for the *same* manufacturing tolerances, the imperfection values obtained will differ for the three methods. Any one of these imperfection values can, in principle, be

used to calculate a safe buckling load. All three methods are allowed by the code. The imperfection values from the first two methods result in safe buckling loads, to the best of our knowledge, and have been validated against experiments [20]. The third method for imperfection quantification, which is potentially the least conservative, is the one we examine in this chapter.

A human aspect of the design activity should be noted. RCC-MR provides several alternative methods of safe design, and the human designer has a design in mind and checks it against one or more of these methods until *one* method certifies the design as safe. Any procedure within the code which allows a designer to certify a design as safe is therefore acceptable, and the design moves forward. The designer is neither expected nor encouraged to doubt the code. Neither is the designer required to check the design against several methods within the code and report that they *all* show the design is safe. Safety needs to be certified by *one* method within the code: no more, and no less. For these reasons, even a small source of rare risks in any code-certified design method demands attention from the scientific research community.

With the above motivation, the aim of this chapter is to critique the third method of imperfection quantification allowed by RCC-MR. We do emphasize that in general RCC-MR is comprehensive and impressive, and forms the mainstay of many design procedures in the nuclear industry of some countries including India. Our understanding of the specific calculation we critique below was gained fortuitously through other work not reported here, and we continue to hold RCC-MR in high regard in spite of it.

In this chapter, we will present detailed buckling design calculations for three example structures following the above mentioned (third) calculation alternative as specified in RCC-MR. We have chosen these structures with some care, to illustrate ways in which the imperfection quantification method can lead to potentially highly nonconservative designs. Our concluding suggestion will be that this third method should be re-examined

by competent authorities on shell design, with perhaps greater technical background supplied, or more experiments; or, if deemed appropriate, removed.

3.2 Safe buckling load as per RCC-MR

For completeness, we summarize the calculations prescribed by the code.

RCC-MR, Section III, Tome 1, Subsection Z, technical appendix A7 is sometimes referred to simply as RCC-MR-A7. RCC-MR-A7 provides reduction or knockdown factors for linear eigenvalue based buckling loads to account for geometrical imperfections and plasticity in real structures. We emphasize that the procedures we use here are based on elastic analysis. Design work in the nuclear industry is frequently based on purely elastic analysis based on RCC-MR, such as we examine here. RCC-MR does discuss alternative elasto-plastic design approaches as well, but they are independent of the elastic analyses and do not affect the present chapter.

3.2.1 Calculation procedure

To calculate the safe design buckling load of a structure, a linear elastic stress analysis and buckling analysis must first be carried out. This is routine linear finite element analysis with an arbitrarily chosen notional load N (say, 1 kPa or 1 N/m or 1 kN, as the case may be). Stresses in the structure due to this load are computed in the first step. In the second step, an elastic buckling load is computed using the so-called *eigenvalue analysis* to obtain a load multiplying factor, say λ; if $\lambda = 10.5$, for example, then buckling is predicted to occur at 10.5 times the notional load N (i.e., at 10.5 kN if the notional load was 1 kN).

After the stress analysis of the first step, stresses obtained at critical locations in the shell are to be decomposed into membrane (mean) and bending (linearly varying) parts. This straightforward procedure is described further in appendix 6.1. Note that

longitudinal and circumferential stresses are added tensorially and converted to von Mises stresses to quantify severity.

Subsequently, stresses are categorized into primary and secondary stresses as follows. (i) All membrane stresses are primary stresses. (ii) At locations far from geometrical discontinuities such as sudden changes in curvature, bending stresses are primary stresses as well. (iii) At or near geometrical discontinuities, bending stresses may be treated as secondary stresses[1].

After classifying the stresses obtained through finite element analysis into primary and secondary stresses, we are allowed to drop secondary stresses from further consideration[2], except for the third method of imperfection quantification as mentioned below in due course.

The largest (von Mises) stress intensity obtained above is to be multiplied by the λ obtained from eigenvalue analysis, giving a critical elastic stress. Here stress intensity is the von Mises stress of the stress tensor. This stress is to be divided by the yield stress of the material, to obtain a non-dimensional number ζ. Small ζ suggests that the structure's buckling response is elastic; large ζ implies plasticity will precede or accompany buckling.

Having computed ζ as above, we turn to geometrical imperfections, which the code allows us to quantify by three different methods, presented below in order of decreasing conservatism.

In the first method, the maximum deviation d between the real and nominal shell geometry, measured normal to the nominal shell surface, is to be divided by shell thickness h to obtain

$$\delta = d/h. \tag{3.1}$$

Larger δ leads to larger knockdown factors, as will be discussed in due course. For the

[1]See RCC-MR, Section III, Tome 1, Subsection B, table RB 3324.31 (pp. 97).

[2]The rationale is that secondary stresses can be relieved by local yielding without compromising the entire structure.

second method, the code says that sometimes

> "...it is possible only to consider a fraction of the previous value if it can be shown that the neglected fraction of the tolerance has no effect on instability. Thus, for a tube subjected to external pressure, only the ovalization tolerance is to be considered for defining the defect, to the exclusion of the mean diameter tolerance."

We have no further comment on the above two methods of quantifying imperfection.

The third method of quantifying imperfection, potentially the least conservative, and also the one we critique in this chapter, is as follows. The designer is allowed to define a new defect value d_{new}, which requires an additional linear elastic stress analysis of a deformed geometry generated by superimposing a scaled first buckling mode displacement on the nominal or perfect geometry. The scale factor is chosen to match the actual geometrical defect magnitude. From this additional analysis, the maximum stress intensity S_d (membrane plus bending, *not* dropping secondary stresses) is used to calculate

$$d_{new} = \frac{h}{6}\left(\frac{S_d}{P_m} - 1\right), \tag{3.2}$$

where d_{new} is new geometric defect, P_m is the maximum membrane stress from the linear analyses, and h is the shell thickness. We adopt the smaller of the two P_m's, from the ideal and the perturbed geometries, as a conservative step. Subsequently, the designer adopts the imperfection value

$$\delta = \frac{d_{new}}{h}, \tag{3.3}$$

which could potentially be nonconservative if $d_{new} \ll d$.

General readers may note that quantification of imperfection plays a *critical* role in the thin shell design process, which is conducted under various constraints as described earlier. The designer seeks a thin-walled yet safe design. Keeping imperfection low has

practical difficulties. For example, in a shell of diameter 14 m and thickness 21×10^{-3} m, a radial imperfection of 14×10^{-3} m represents merely 0.1% of the diameter, yet gives $\delta = 2/3$ by Eq. (3.1), usually too large for the resulting design to be practical. In such circumstances, a code-backed method of computing a smaller effective imperfection value is attractive. For this reason, critical examination of this third method of imperfection quantification is important.

With ζ and δ computed as above, the reduction factor $X(\zeta, \delta)$ is found from two charts provided in the code: one for stable and one for unstable post-buckling behaviors. Figure 3.1 shows the chart for unstable post-buckling, adapted from RCC-MR. X is as in Eq. (3.4), and $Y = \zeta X$. We have extracted the data and developed an interpolation program (details omitted), so arbitrary numerical values can be used.

Finally, the safe load for the structure is specified as the original load times the load multiplying factor times $X(\zeta, \delta)$, divided by a further safety factor of 2.5, i.e.,

$$\text{Safe load} = \frac{(\text{Notional load } N) \times (\lambda \text{ from eigenvalue analysis}) \times X(\zeta, \delta)}{2.5}. \tag{3.4}$$

In the Eq. (3.4), if the critical elastic stress value was not purely a membrane stress, but included both a membrane and a bending stress, then the safety factor would be 1.667 instead of 2.5.

From Fig. 3.1, for X to be close to unity, one needs *both* (i) very low imperfection or small δ, and (ii) predominantly elastic response at buckling, or small ζ. These conditions may be practically impossible to achieve for (i) large thin walled structures (small h increases δ) (ii) operating at high temperatures (lowered yield strength raises ζ). If a designer is forced to use $\delta = 1$, then the allowed stress levels may be too low to be useful: structural design may be unfeasible if one cannot exceed even 10% of yield stress. Yet, with other parameters held constant, if the code allows the designer to claim $\delta = 0.25$, then the allowed stress may double, making progress feasible.

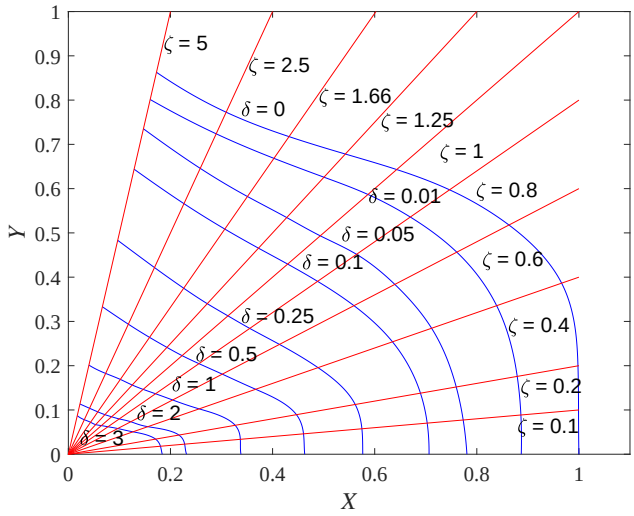

Figure 3.1: RCC-MR reduction factor chart for unstable post-buckling behavior, recomputed using our own interpolation program.

We hope that a general reader will by now be convinced that use of Eq. (3.2) for nuclear reactor shell design potentially has very significant consequences.

3.3 Shell design case studies

In this chapter we present case studies of three shell geometries, chosen to emphasize potential difficulties with Eq. (3.2).

First we note that RCC-MR-A7 provides reduction factors charts for un-stiffened shells, made of stainless steel 316 LN, whose properties are given in properties group A3.1S of [46]. The maximum value of ζ as defined in section 3.2, for which reduction factors are provided, is 5. Hence, dimensions and thickness of our shell examples below are chosen such that ζ remains below 5. Operating temperatures for these shells are taken notionally to be 293 K; but it will be seen that the precise temperature is irrelevant. The Young's modulus and yield stress of the material, in our example calculations below, are taken to be 2×10^5 MPa and 220 MPa respectively; and Poisson's ratio is taken to be 0.3 (see [46]). No other material parameters are needed by the code. For our finite element calculations, the thin shell geometry is modeled in the commercial finite element package

ABAQUS using first order, reduced integration, S4R elements.

In the following three subsections, we describe our three example shell structures. Analyses for these structures will be presented subsequently.

3.3.1 Example 1: Nonuniform cylinder with a spherical cap

See Fig. 3.2. We consider an axisymmetric thin shell, consisting of two concentric cylinders of different radii and heights, joined through two transition regions of large radii and a small conical region. The radius and height of the bottom cylinder are 2.3 m and 2.5 m respectively. The radius and height of the top cylinder are 1.15 m and 1.25 m respectively. The top of the upper cylinder is closed with a spherical cap of radius 3 m. The spherical cap and top cylinder are joined by a small fillet of radius 0.1 m. The wall thickness everywhere is 5×10^{-3} m. The displacements of the bottom edge of the structure are arrested, as shown.

The spherical cap is subjected to external pressure, with a notional load N of 50 kPa. A typical element size used in the calculation is of 20×10^{-3} m, selected from mesh convergence studies (see appendix 6.2).

3.3.2 Example 2: Ellipsoidal head

See Fig. 3.3. We consider a structure composed of an axisymmetric ellipsoidal head on a cylindrical shell. In the cross section shown in Fig. 3.3 (left), the elliptical curve represents the head; the aspect ratio of the quarter-ellipse shown in the cross section is 4. The radius of the cylindrical shell is 4 m. All shell wall thicknesses are 2.5×10^{-3} m. All displacement degrees of freedom of the top edge of the cylinder are arrested, as shown in Fig. 3.3 (right). The entire structure is subjected to internal pressure, with a notional load N of 15 kPa. Based on mesh convergence studies (see appendix 6.2), an element size of 25×10^{-3} m is used.

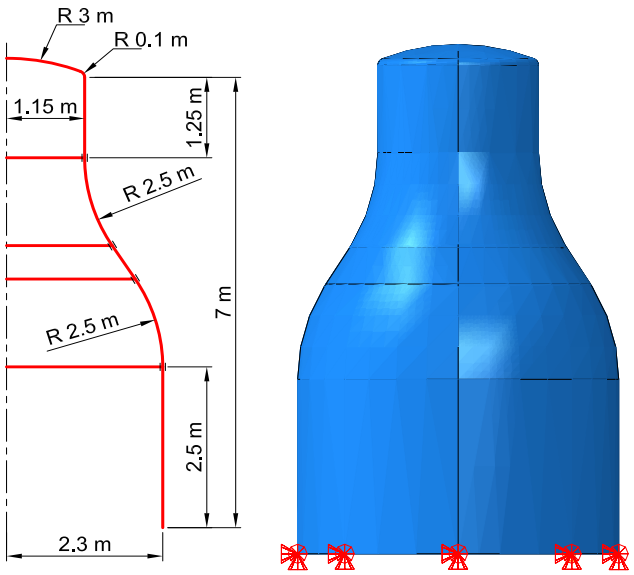

Figure 3.2: A nonuniform cylinder. Loading: external pressure on the spherical cap of radius 3 m. Left: schematic diagram. Right: ABAQUS model with boundary conditions.

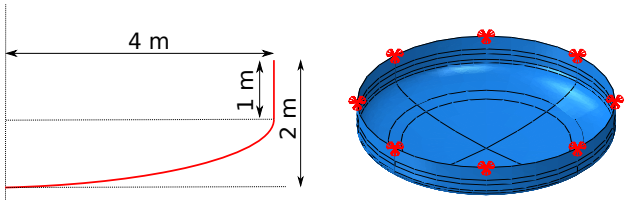

Figure 3.3: Ellipsoidal head. Loading: internal pressure. Left: schematic diagram. Right: ABAQUS model with boundary conditions.

3.3.3 Example 3: L-shaped shell under vertical end load

See Fig. 3.4. We consider a thin shell consisting of two cylinders of radius 1 m and length 10 m, perpendicular to each other, with an elbow shaped connection between them. The radius of the elbow's centerline is 3 m. The shell geometry is generated by sweeping a circle (figure, left) along a curve (figure, right). Figure 3.5 shows an ABAQUS model of the L-shaped shell.

The shell thickness is 5×10^{-3} m. One end of the shell is assigned a built-in boundary condition (all degrees of freedom restrained), and the other end is subjected to a vertically downward circumferentially distributed force (Fig. 3.5), with a notional load N of 1000 N/m. Based on mesh convergence studies (see appendix 6.2), an element length of 50 $\times$

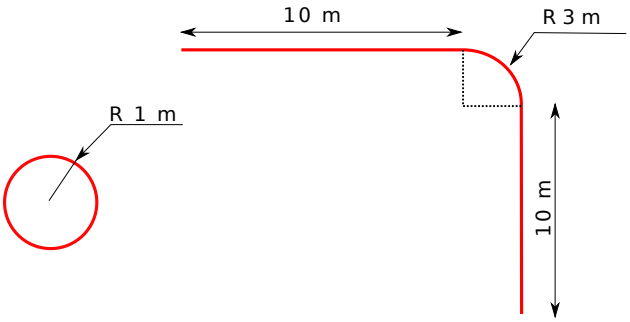

Figure 3.4: L-shaped shell. Left: circular cross section. Right: swept path used to define geometry.

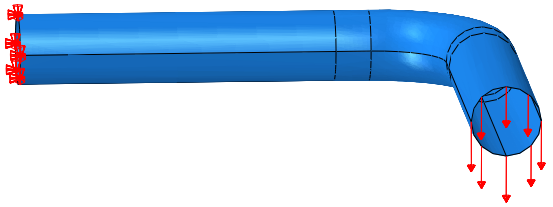

Figure 3.5: ABAQUS model of L-shaped shell with boundary conditions and downward-acting end loads.

10^{-3} m is used.

3.4 Imperfection quantification

The three shells given in subsections 3.3.1, 3.3.2 and 3.3.3 do not, in our opinion, involve extreme or outlandish geometries. They represent reasonable design situations. We now work out how a designer following the code might estimate the safe loads for these shell structures.

For each of the three shells, we will proceed as follows. Recall section 3.2 and Eq. (3.2). S_d is the maximum stress intensity (bending plus membrane), while P_m is the largest membrane stress. To be conservative, we interpret S_d to be the largest value obtained in the geometrically perturbed structure, and take P_m to be the smaller among the two largest values (unperturbed and perturbed geometries).

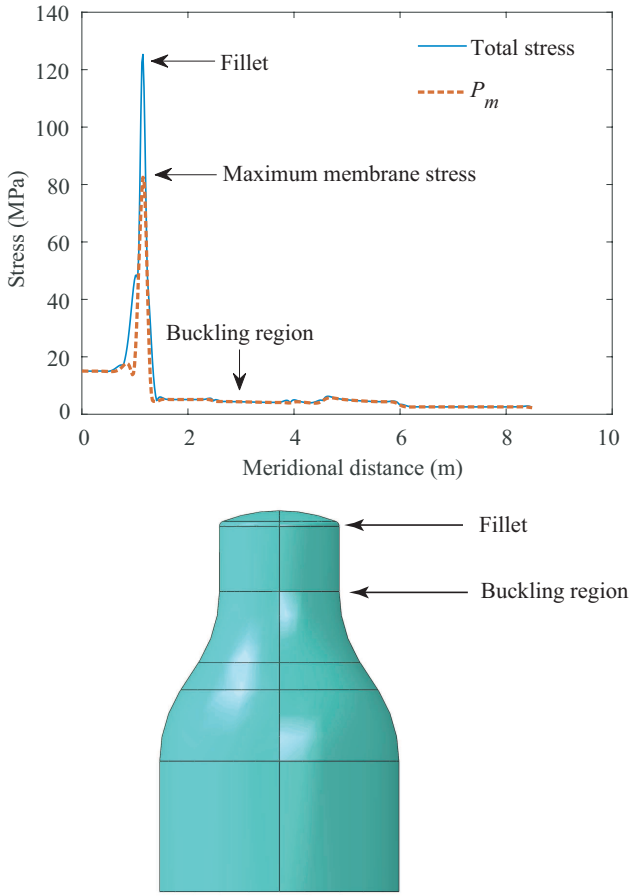

Figure 3.6: Top: membrane stresses, and total stresses (von Mises), plotted against curvilinear distance along the shell. Bottom: key locations on the shell.

3.4.1 Nonuniform cylinder with a spherical cap

First, analysis results for the ideal structure are presented in Fig. 3.6. The key property of this structure, for our purposes, is that the buckling region is removed from the region of most severe stresses.

Figure 3.6 (top) shows stress plots; and Fig. 3.6 (bottom) shows the structure with two key locations marked. Total stress in Fig. 3.6 and subsequent figures is computed as follows. At any location on the shell, for both inner and outer surfaces, the bending and membrane stresses are added tensorially. Then the von Mises stress is computed for both locations, inner and outer, and the higher value is used.

The largest bending stress and the largest membrane stress both occur at the fillet, far

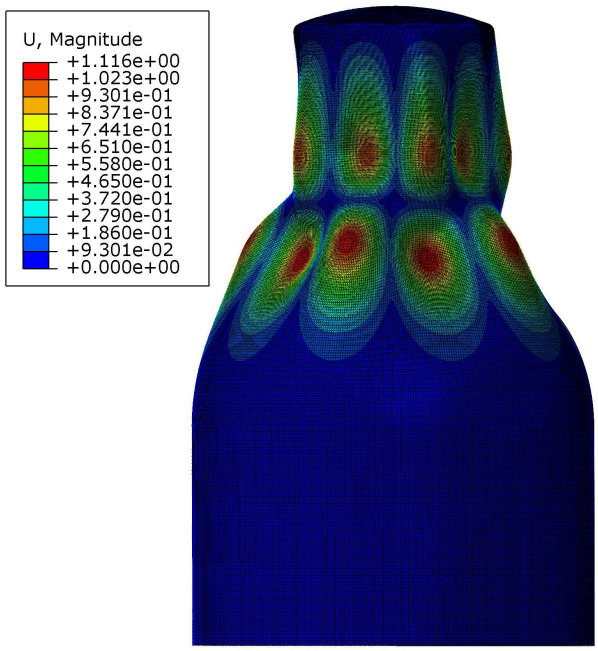

Figure 3.7: First linear elastic buckling mode of nonuniform cylinder with spherical cap. Displacements are exaggerated.

from the buckling region. Since the most severe stress occurs near a point of discontinuity in the geometry, the bending stress there is treated as a secondary stress (recall section 3.2). Results from the linear eigenvalue analysis are shown in Fig. 3.7, and show the buckled shape (with displacements exaggerated).

Now, as per the recommendation leading to Eq. (3.2), we are supposed to perturb the shell geometry in the same shape as the buckling mode, but with an amplitude equal to the imperfection present (or, in the case of designs, the imperfection allowed). It is a practical fact that no thin shell designer in the nuclear industry can assume an imperfection higher than the shell thickness, or $d/h > 1$ (recall the discussion following Fig. 3.1). For example, $d/h = 0.5$ is used in [50] (pp. 608). Here, for illustration, we adopt some overly high values of d/h to examine Eq. (3.2).

Results from an initial linear stress analysis on a perturbed geometry with $d/h = 1.5$ are shown in Fig. 3.8. A stress plot along the lines of Fig. 3.6 (top) is shown in Fig. 3.9. The oscillations in the total stress value are because of the oscillatory perturbation in

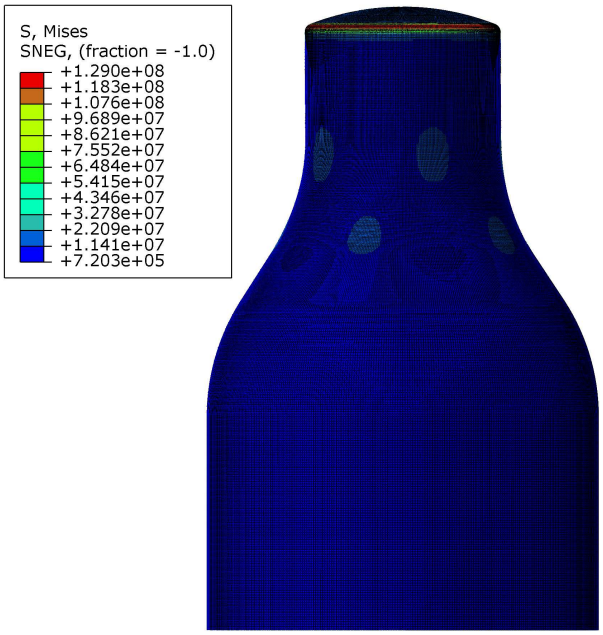

Figure 3.8: Results of linear stress analysis of a perturbed geometry with $d/h = 1.5$.

shape. They are not numerical artifacts.

The perturbation in geometry has influenced stresses mainly in the buckling region. The maximum bending plus membrane stress (S_d) at the fillet region has remained unchanged. The maximum membrane stress P_m has increased, but as explained above, to be conservative we will use the *smaller* P_m, i.e., from the ideal geometry or Fig. 3.6. In other words, for this structure, the effective imperfection computed using Eq. (3.2) is independent of the actual imperfection.

To better understand the role of d/h in these calculations, we carry out several linear elastic stress calculations with $d/h = 0.5$, 1.0, 1.5, 2.0, 2.5, and 3.0. Results are summarized in Fig. 3.10. It is seen that for all values of d/h any thin shell designer in the nuclear industry is likely to use, the largest S_d occurs in the fillet region and does not change at all; and P_m is lowest for the unperturbed structure and so that, too, does not change.

Thus, for our first example, namely the nonuniform cylinder with a spherical cap, by the third method of imperfection quantification, d_{new}/h is independent of imperfection, and is in fact remarkably low (about 0.12), more than 4 times smaller than the typically

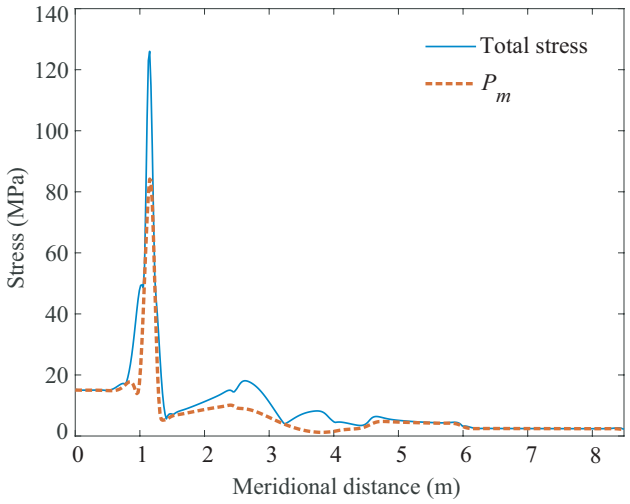

Figure 3.9: Membrane stresses, and total stresses (von Mises), plotted as a function of curvilinear distance measured along the shell, for $d/h = 1.5$.

used value of 0.5.

We now consider our second example.

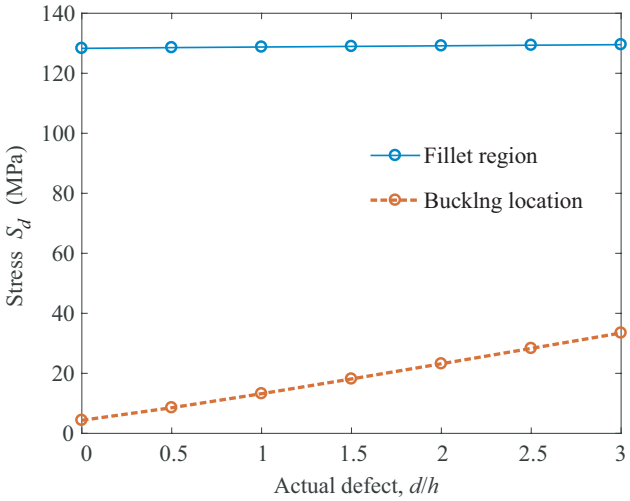

Figure 3.10: S_d at two locations: the fillet region, and in the buckling region. The horizontal axis depicts imperfection d/h.

3.4.2 Ellipsoidal head

In the ellipsoidal head, maximum stress severity occurs at approximately 0.1 m below the junction between the ellipsoidal head and the cylindrical portion. Maximum displacement

due to buckling occurs approximately 0.6 m below that junction. Figures 3.11 and 3.12 show the von Mises stress distribution and the first elastic buckling mode of the ellipsoidal head respectively (displacements are exaggerated). Figure 3.13 shows membrane stress and total stress (von Mises) plotted against curvilinear distance along the shell. Figure 3.14 shows key locations corresponding to Fig. 3.13.

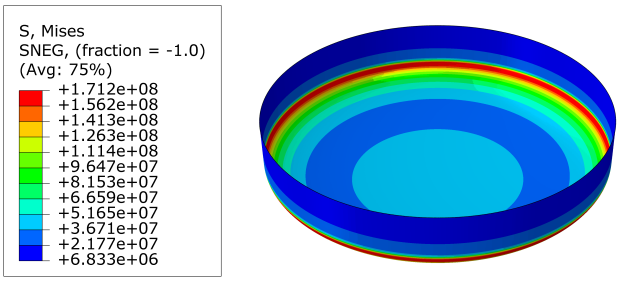

Figure 3.11: von Mises stress distribution in ellipsoidal head.

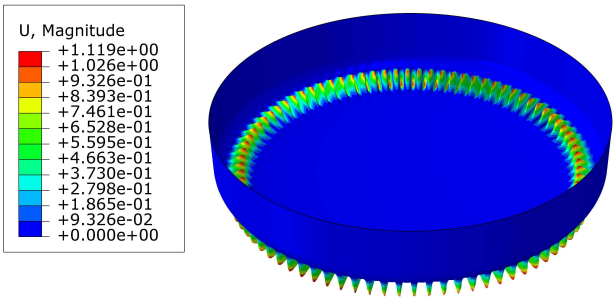

Figure 3.12: First buckling mode of ellipsoidal head.

As before, we perturb the geometry of the ellipsoidal head with imperfections of magnitudes $d/h = 0.5$, 1.0, 1.5, 2.0, 2.5, and 3.0. Stress profiles are plotted for $d/h = 1.5$ in Fig. 3.15. A rather significant increase in S_d is seen.

Figure 3.16 shows the final key results for different values of d/h. The increase in S_d notwithstanding, the computed imperfection seems too small. For the practical or reasonable value of $d/h = 0.5$, the new imperfection is about 25 times smaller at about 0.02, which is unreasonably small. In our opinion, such low imperfection is near-impossible to fabricate for large commercial thin-walled structures. For the impractically large value of $d/h = 3$, the new imperfection is about 15 times smaller at about 0.2, which is much

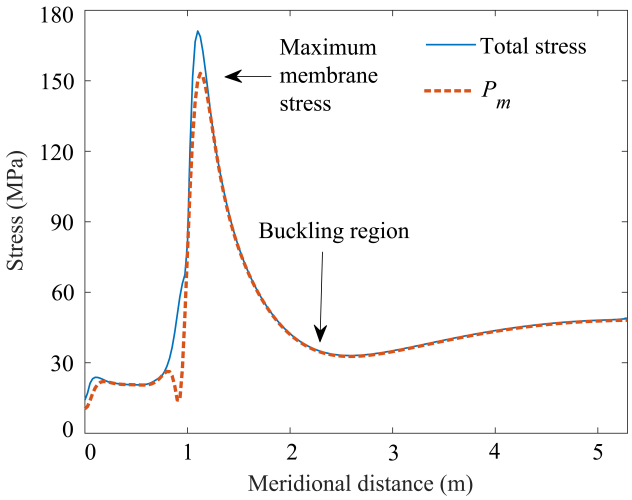

Figure 3.13: von Mises stress variation along the meridian of ellipsoidal head for perfect geometry. Key locations are marked.

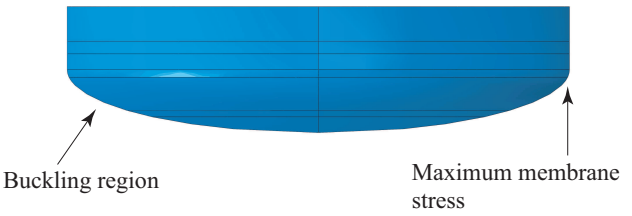

Figure 3.14: Ellipsoidal head geometry with key locations corresponding to Fig. 3.13.

smaller than the typical value of 0.5.

The dramatic conclusions from the study of the ellipsoidal head bear emphasis. The structure does not even have a sharp discontinuity. Yet, for an assumed physical imperfection of 0.5, Eq. (3.2) allows the designer to claim an *effective imperfection value that is twenty five times smaller*, i.e., the structure can be treated as essentially perfect.

We now turn to our third and final example.

3.4.3 L-shaped shell under vertical end load

Figures 3.17 and 3.18 show the von Mises stress distribution and first buckling mode of the L-shaped shell. The maximum stress occurs at the bend. Maximum displacement due to buckling occurs at the cylinder's free edge. Note that the region near the free edge does not have the largest deformations, merely the largest displacements; but it controls the

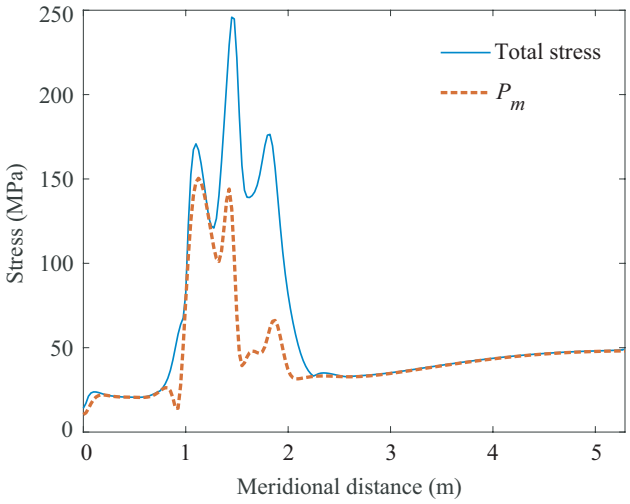

Figure 3.15: von Mises stress variation along the meridian of ellipsoidal head with geometry perturbed with imperfection $d/h = 1.5$.

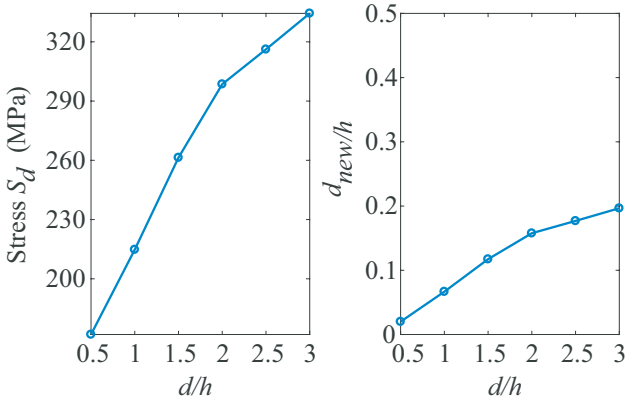

Figure 3.16: Ellipsoidal head. Left: Maximum stress S_d against actual d/h. Right: new imperfection value against actual d/h.

magnitude of the imperfections to be considered in the perturbed geometry. Figure 3.19 shows the membrane stresses and total stresses plotted against curvilinear distance along the shell along with some key locations indicated on the shell. Not surprisingly, stress analysis with a perturbed geometry shows no significant amplification of the stress levels at the bend location: see Fig. 3.20, where we have used $d/h = 1.5$. Figure 3.21 shows the variation of maximum stress intensity S_d, and d_{new}/h computed as per Eq. (3.2). It is seen that the computed effective imperfection value using Eq. (3.2) is essentially independent of the actual imperfection used, and is also extremely low (around 0.07 over a large range

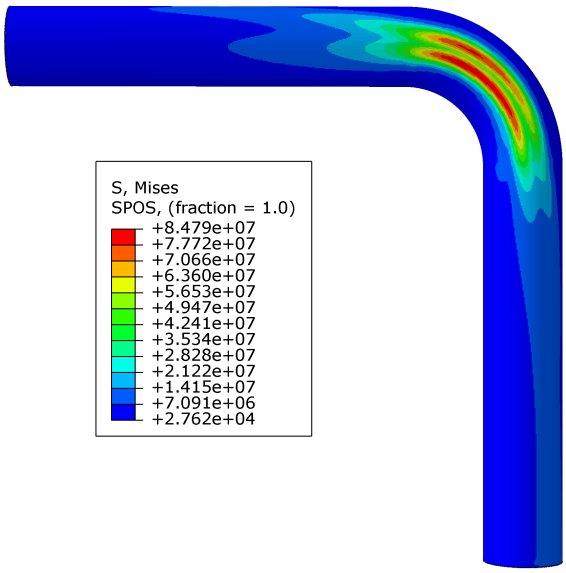

Figure 3.17: von Mises stress distribution in L-shaped shell.

of actual imperfection).

The low imperfection values computed for all three examples in this section will result in high predictions of allowable safe loads, as we will see next.

3.5 Final safe load estimation

Having decided on the imperfection value δ, and computed the eigenvalue analysis based load multiplying factor λ for all three design cases, it remains to obtain ζ by dividing critical elastic stress with the yield stress of the material (recall section 3.2). For all three cases, we will use the chart for unstable post buckling behavior (Fig. 3.1) to be conservative. We will compute safe buckling load as per both, the first method and third method of quantifying imperfections.

We first compute the safe buckling load for the nonuniform cylinder with a spherical cap.

The pertinent facts from the eigenvalue analysis are as follows. The notional load is $N = 50$ kPa, and the load multiplier $\lambda = 6.8229 \approx 6.82$. The critical elastic stress, for

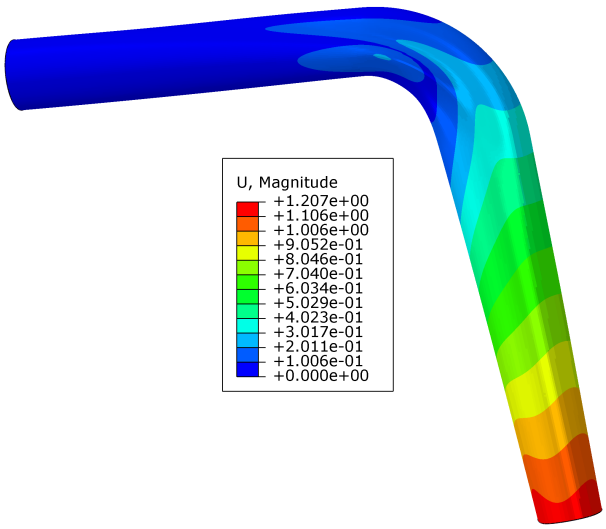

Figure 3.18: First buckling mode of L-shaped shell.

the applied pressure 50 kPa from Fig. 3.6, is 83.73 MPa. The yield stress of stainless steel 316 LN at room temperature is 220 MPa [46]. We find

$$\zeta = \frac{83.73 \times 6.82}{220} = 2.5956 \approx 2.6. \tag{3.5}$$

With the first method, with $\zeta = 2.60$ and a defect of $d/h = 1.5$, from the chart $X(\zeta, \delta) = 0.0517$, leading to a predicted safe load of 7.05 kPa. However, with the third method, with $\zeta = 2.60$, and new imperfection estimate $d_n/h \approx 0.09$, we obtain from the chart $X(\zeta, \delta) = 0.2262$, leading to a predicted safe load of 30.85 kPa. In other words, a designer using Eq. (3.2) can claim a safe load that is about 4.4 times bigger than predicted using the standard method.

Details of similar calculations for the ellipsoidal head and the L-shaped shell are given appendix 6.3. Here we report the final (large) factors by which the safe loads vary, when calculated using the first and third method of quantifying imperfection. For the ellipsoidal head, safe buckling loads as per the first and third methods are 1.14 kPa and 4.60 kPa respectively, i.e., a factor of 4. For the L-shaped shell, safe end loads as per the first and third methods are 198.34 N/m and 920.49 N/m respectively, i.e., a factor of 4.6.

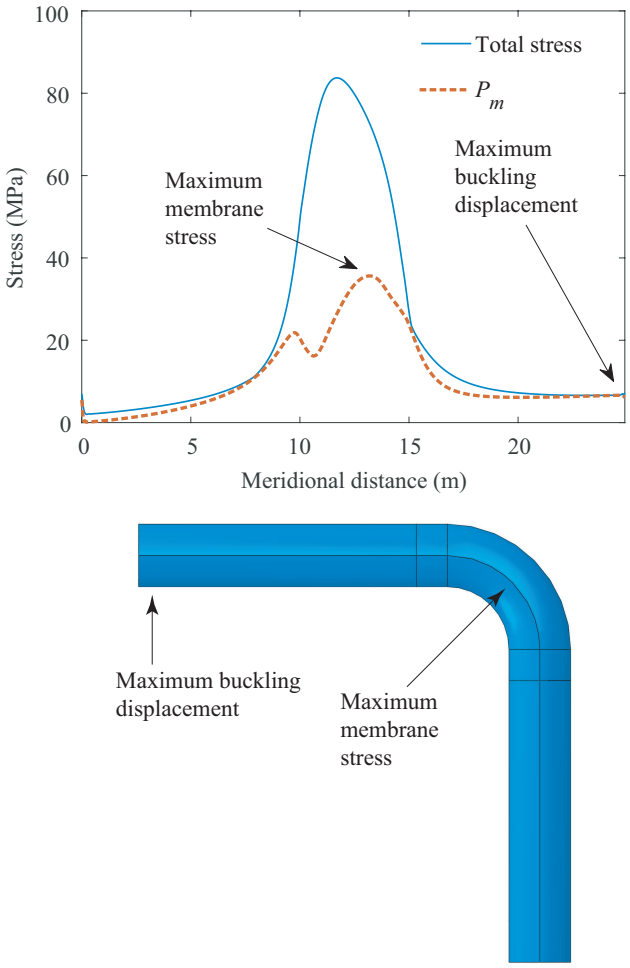

Figure 3.19: Top: membrane stresses, and total stresses (von Mises), plotted against curvilinear distance along the shell. Bottom: some key locations on the shell, (rotated view).

These three factors by which the safe load "increases" simply by use of Eq. (3.2), namely 4.4, 4 and 4.6, seem large. To understand the implications better, we can reconsider the calculation using a hypothetical example as follows.

Comparing imperfection values of 1.5 (usually too high) against a claimed value of 0.07 (very low) for a stainless steel 316 LN structure operating at 798 K, with a yield stress of 107 MPa, using the first method, we may be allowed a maximum stress of 6.3 MPa (impractically low) while using the third method we may be allowed a maximum stress of 30.2 MPa (with progress possible). A designer who did not have permission to use the third method of imperfection quantification would be forced to consider other,

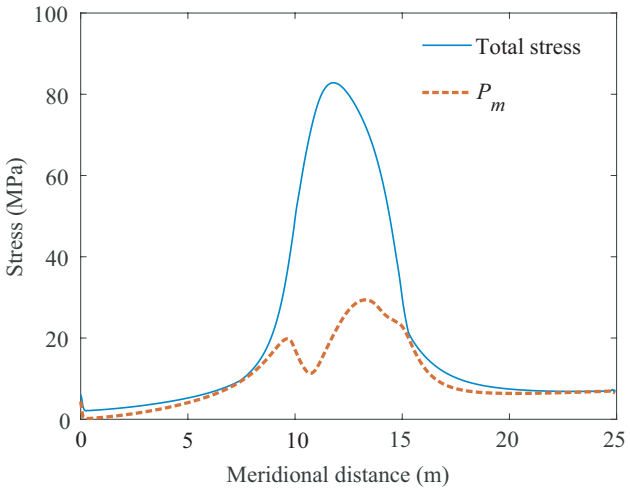

Figure 3.20: von Mises stress along the L-shaped shell (along different lines: one that passes through the point of maximum S_d and one that passes through the point of maximum P_m) for perturbed geometry with $d/h = 1.5$.

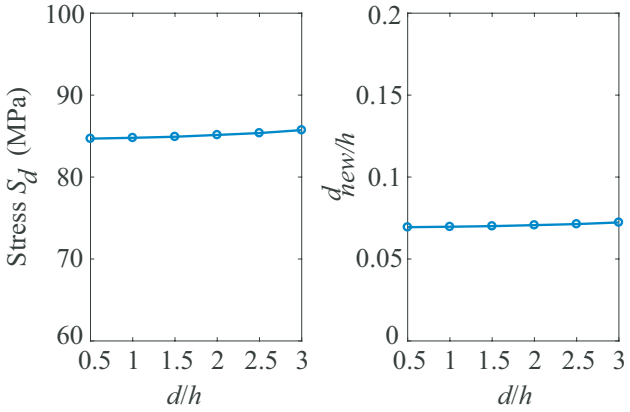

Figure 3.21: L-shaped shell. Left: maximum stress S_d. Right: new imperfection value against actual d/h.

possibly more expensive or more clever, designs. A designer who was allowed to use the third method, on the other hand, would be justified in settling on an easy, code-backed, and yet potentially nonconservative, design option.

3.6 Three ways in which the equation for $\mathbf{d_{new}}$ can fail

We recall Eq. (3.2), rewritten below

$$d_{new} = \frac{h}{6}\left(\frac{S_d}{P_m} - 1\right), \tag{3.6}$$

and note that the critical stresses (S_d, membrane plus bending; and P_m, membrane only) involve calculation with a notional and a perturbed geometry. The perturbation to the geometry is in the shape of the buckling mode shape, with amplitude equal to the actual physical imperfection d. The foregoing examples illustrate three ways in which the strategy can fail.

First, the buckling displacements may be localized to regions that are far away from the points where S_d and P_m are large. Subsequent perturbation in the shape of the buckling mode shape then leave the critical stress locations unaffected, and the new computed imperfection is found to be independent of the actual imperfection. This was observed in the first example (nonuniform cylinder with spherical head).

Second, even after perturbation, the ratio of S_d/P_m may not be significantly greater than unity; for example, if the ratio is 1.12, say, then we have an imperfection of about 0.02, which is unrealistically small and dangerous. This could potentially happen for some shells where the ratio was close to unity to begin with. Such was observed in the second example (ellipsoidal head).

Third, although buckling occurs at some highly stressed location, due to some long unbuckled section the actual displacement may be relatively much bigger at some faraway location. On scaling the perturbation to match the largest displacement to the physical imperfection, we then end up hardly perturbing the geometry where it most needs to be perturbed, and thereby end up with a small and insensitive imperfection value. This last

possibility was observed in the third example (L-shaped shell).

3.7 Discussion and conclusions

Liquid metal cooled fast reactors must be designed to be safe under all types of loading, to the extent of our knowledge and understanding. Yet, the response of large thin shells, containing low-viscosity liquid metal, under random loading that might conceivably excite complex dynamic fluid-structure interactions and resonances, is *extremely* difficult to predict with high accuracy and confidence. This is why we use design codes, and it is critically important that the codes be conservative.

Specified limits on geometric imperfection (i.e., manufacturing tolerances) strongly influence the cost of large thin-walled shell structures. Requiring tighter tolerances raises costs significantly. A code-backed calculation based on Eq. (3.2) presently allows a designer to claim a smaller *effective imperfection* value in his safe load calculation even while specifying larger manufacturing tolerances. This lets the designer lower costs. We emphasize that there is no implication of misconduct here: it is a simple practical consequence of Eq. (3.2) applied to any one of the shell structures described in this chapter.

Additionally, as observed above, the effective imperfection value from Eq. (3.2) can be quite insensitive to the actual physical imperfection. Yet, for structures with unstable post buckling behavior, it is well known that the buckling load is highly imperfection sensitive [14]. In this light, the recommendations resulting from Eq. (3.2) seem to contradict wide experience.

Finally, a designer who finds that, as per code-backed calculations, the safe load for his structure is both high and independent of physical imperfection may be tempted to lower wall thicknesses in places to achieve other technical goals in their specific application, potentially increasing the non-conservativeness.

For these reasons, we suggest that the third method of imperfection estimation in

RCC-MR be reconsidered carefully by its authors and other competent authorities on shell design, with perhaps greater technical background supplied, or more experiments; or, if deemed appropriate, removed.

We conclude this chapter by noting an anonymous reviewer's remark. The reviewer suggested that our comments on a designer's motivations might be misinterpreted as bordering on accusations of misconduct. We emphasize that such is not our goal at all. In our view, the designer trusts the code. That, in fact, is the whole point of the code. If *one* design procedure given in the code says that the structure is safe, the designer concludes that it is indeed safe. The designer is not required to verify or report that *several* alternative procedures in the code certify the structure is safe. If two alternative methods in the *same* code conclude differently, i.e., one suggests the structure is safe while the other says the load should be lowered, then the designer is technically fully justified in accepting the first conclusion. The responsibility of ensuring that *all* suggested methods are sufficiently conservative lies completely on the code.

In this chapter we have demonstrated that the third method can result in a surprisingly high safe buckling load. However, a sceptic may still argue that a higher safe load from the third method is not *unsafe* but merely higher than the safe load computed using the first method. Thus, she may argue that the nonconservatism of the third method is not conclusively proven. Towards that end, in the next chapter, we present two design examples and prove the nonconservatism of the third method unequivocally.

Chapter 4

Unequivocally nonconservative results from RCC-MR's third method

In this chapter, continuing with the critique of the third method of imperfection quantification in RCC-MR, we are able to conclusively show non-conservatism. The work in this chapter has been published in [30].

4.1 Introduction

As has already been noted in earlier chapters, thin shells are extensively used in structural design of liquid-metal-cooled fast breeder reactors. Such thin shells are sometimes at risk of buckling. Geometric imperfection and reduced yield strength at high temperatures both lower the buckling strength of such shells. The design code RCC-MR is used to design such shells against buckling [18]. RCC-MR is in general a robust design code and used predominately in fast breeder reactor design because it allows both arbitrary shell shapes and high temperatures (up to 700°C). These introductory lines are retained here at

the cost of some repetition, in the interest of making the chapter independently readable.

As noted earlier, RCC-MR specifies various procedures, some based on purely elastic analysis and others on inelastic analysis, to check the safety of a given design. These procedures are independent: the designer needs to demonstrate safety using any *one* procedure. Here we focus on the elasticity based approaches within RCC-MR. These approaches are based on computing reduction or knock-down factors on linear buckling loads, using two additional considerations: (i) yield stress, and (ii) an imperfection quantity.

RCC-MR specifies three methods to quantify imperfection in thin shells. In recent work [29], we have critiqued the *third* of these methods. In particular, we have shown that the imperfection quantity obtained using the third method can in some cases be 25 times lower than the imperfection quantity obtained from the first method, resulting in a declared safe load that is 4.6 times higher. However, our computations in that chapter did not *prove* nonconservatism in the third method. For example, a skeptic might argue that both designs were conservative, with the first method merely more conservative than the other, i.e., that the third method is still conservative, and merely more efficient.

The reader may note that proving nonconservatism in such situations is not trivial. There are no known analytical examples that serve our need, and so we must resort to either experiments or detailed simulations. Experiments may not convince skeptics who doubt the procedural precision, actual imperfections, true boundary conditions, or material quality in the experiments. Detailed simulations with elastoplastic material response could potentially be similarly doubted by skeptics who might observe that the plastic part of the constitutive relation is, after all, approximate.

For these reasons, we present in this chapter two simulations where the notional geometry and imperfection are both precisely described; the boundary conditions used are precisely stated; the structural response stays in the elastic regime; and the computations are carried out using a fine mesh and with a well established commercial code. Our intent

is that our computational examples should be both convincing in themselves as well as completely reproducible by others.

We have chosen two structural examples for demonstration. One example is a hemispherical shell subjected to external pressure and undergoing axisymmetric deformations. There are no radial restraints on the diametral circle, but rotations are restrained there (the simulation may thus also be viewed as one of a full hemispherical shell assuming top-and-bottom symmetry). The second example is a torispherical shell, subjected to external pressure, with similar symmetric boundary conditions. Both shells are thin enough that the postbuckling response is elastic. The imperfection assumed is a tiny axisymmetric change in curvature at the top, motivated by work discussed in [51] and [52]. We point out that both the geometry and loading in these design examples are reasonable: the spherical shell is a fundamental shape in design studies of thin shells under external pressure, while the torispherical shell finds direct application in some structures relevant to nuclear power plants. For both these structures, we will present the safe buckling load obtained using imperfection quantification by both the first and third methods of RCC-MR. Subsequently, the collapse loads of these imperfect, but still idealized and precisely described, structures will be obtained through geometrically nonlinear buckling analysis carried out using ABAQUS.

In what follows, we will first propose some terminology regarding bounds on safe loads. These terms will help to put the rest of the chapter in context, and explain why we claim that our calculations here constitute *proof* that the third method of imperfection estimation can in fact be nonconservative. We have described in full detail the procedure of calculating safe buckling load as per RCC-MR in chapter 3. However, in this chapter, we briefly present the safe buckling calculation procedure for the sake of completeness, and in the interest of keeping this chapter independent of others.

We now briefly describe the procedure of calculating safe loads using elastic analysis

as per RCC-MR. Then we will present details of our finite element models of the hemispherical shell and torispherical shell. We will present calculations of safe buckling loads with both the first and the third imperfection quantification methods. Finally, we will present geometrically nonlinear calculations of the maximum pressure sustained by the imperfect hemispherical and torispherical shell. We will end with some straightforward conclusions.

4.2 Bounds on safe loads

We adopt the following context for the structural design activity.

A real structure may be subjected to complicated and time-varying loads; and failure may be gradual or sudden. Design work based on nonlinear simulation often proceeds, however, by considering a pseudostatically increasing load that is precisely specified. The collapse load is taken to be that at which the load versus displacement curve first attains zero slope, because a subsequent small increase in load causes a large increment in deflection. Subsequently, safety factors may be introduced to knock down the safe load estimate below the computed collapse load.

For simplicity in the discussion below, we assume the load can be described by a single scalar load magnitude denoted by M. In simple cases, such as shells subjected to external pressure, M is indeed a single scalar, namely the pressure. For a structure under combined loading, e.g., a force F at some known point and another force $2F$ at another known point, we can take the scalar M to be the same as F, with the understanding that doubling M means all forces on the structure are doubled.

In this context, we consider some loading and failure situations that will clarify our discussion.

1. Let M_{ac} be the actual load at which the real structure being designed will collapse. This load is not known exactly. The aim of safe design is merely to ensure that M_{ac}

lies safely above loads actually experienced in service.

As a specific hypothetical example for clarity, imagine designing a shell subjected to external pressure. If the designer was able to experimentally load a prototype to failure, imagine that it *would fail at something like* 1×10^6 Pa, but such experimentation is not possible on the structure because it does not exist yet; or when it is built it will be too expensive to test in such a destructive way; or even if tested, it will show variation from test to test, i.e., it will have some random variations. In other words, the actual load of failure is not known, or cannot be known, or has some randomness in it.

2. Let M_{sl} denote a safe load for the structure. The aim of efficient design is to compute relatively high values of $M_{\text{sl}} < M_{\text{ac}}$. Here, "relatively high" makes the structure efficient, but if the inequality is violated then the structure fails. The design code specifies safe ways of computing such M_{sl}.

   If the design code allows k alternative methods, these methods may yield k different values,

   $$\{M_{\text{sl}_1}, M_{\text{sl}_2}, M_{\text{sl}_3}, \cdots, M_{\text{sl}_k}\}.$$

   The code does not require us to compute all these "safe" loads. We are allowed to choose *any* method p, and declare M_{sl_p} as a safe load.

   In the hypothetical example of item 1 above, imagine that four methods predict safe loads of

   $$\{M_{\text{sl}_1} = 6 \times 10^5 \text{ Pa}, M_{\text{sl}_2} = 2 \times 10^5 \text{ Pa}, M_{\text{sl}_3} = 7 \times 10^5 \text{ Pa}, M_{\text{sl}_4} = 5 \times 10^5 \text{ Pa}\}.$$

   The designer need not implement all methods, and can justifiably claim 6×10^5 Pa (say) as a safe load. The 7×10^5 Pa result need not be computed; and the 2×10^5

Pa result, even if computed, need not be reported.

3. Let M_{op} be the target or operational load.

   By this we mean that a tentative design for the structure is available. Its material and geometric specifications have been tentatively chosen. We are required to state whether the structure can safely sustain a load M_{op}.

   At this stage, being partially committed to a design, the designer is free to choose any $1 \leq p \leq k$ such that that $M_{\text{op}} < M_{\text{sl}_p}$.

   In the hypothetical example of items 1 and 2, if $M_{\text{op}} = 6.7 \times 10^5$ Pa, the designer is perfectly justified in sequentially trying everything, eventually trying the $M_{\text{sl}_3} = 7 \times 10^5$ Pa method, and thereby declaring the structure to be safe.

   A sobering consequence is that weak designs, through a designer's justifiable trial and error, may actively seek out the less conservative design methods from among the k methods allowed by the code. No malpractice on the part of the designer is implied by such a search, because the code presents all k methods as viable ones.

4. Next, we consider bounds on the load. Such bounds can be obtained using experiments or simulations. We explain here why good simulations provide more rigorous bounds than experiments. This is initially a little counterintuitive, because experiments are real and simulations are virtual.

   Let M_{e} be the failure load observed in a reliable experiment with a prototype of the structure being designed. Clearly, M_{sl} should not be greater than M_{e}. We call M_{e} an *empirical* upper bound on safe loads. In principle, others subsequently attempting the *same* experiment with notionally identical prototypes may obtain different failure loads. Thus, if some other people obtain lower failure loads, we will lower our initial upper bound. Conversely, it may happen that the first experiment actually had some flaw which we do not fully understand, but a hundred subsequent

experiments show a significantly higher failure load. Then we may discard the first experiment as an outlier, and raise our initial upper bound. In this sense, an experimentally obtained failure load provides an empirical upper bound. The bound may change upon repetition of the same experiment by others.

In contrast, let M_{c} be the failure load computed in a careful, well documented, and reproducible nonlinear numerical simulation of the structure. Assuming that the model used is within the purview of the design code (e.g., thin walled shell, allowable material properties, reasonable boundary conditions, purely elastic regime) and the computations are reliable (e.g., sufficiently refined mesh, robust and widely trusted finite element package), then M_{c} is a rigorous upper bound on safe loads. Provided the mathematical model for the structure is properly specified and the computation is done by a competent analyst, the result obtained will not change if someone else repeats the calculation. If another analyst does another calculation with, e.g., a slightly different geometrical imperfection, then a lower load may be obtained. In such cases, the upper bound can come down. But it can never go up. This is why computations provide rigorous upper bounds. If someone else comes along and claims that a higher load is safe, the existing computation can invalidate that claim.

For these reasons, we will proceed with numerical simulations in this chapter, because they provide rigorous upper bounds. No load can be called safe if it is higher than the failure load obtained from a reliable numerical simulation based on permissible mathematical modeling.

5. Finally, matters are slightly complicated due to the use of safety factors in design codes, as follows.

   Suppose that method A (not related to RCC-MR) of calculating a safe load yields a value $M_{\mathrm{sl_A}}$.

   Additionally, we carry out a detailed numerical simulation and obtain a computa-

tional failure load M_c. This M_c may be used in some other method (let us call it method B, and note that this, too, is not related to RCC-MR) of calculating safe loads, where the code says that M_c should be divided by a safety factor, e.g., 2.5. In other words,

$$M_{sl_B} = \frac{M_c}{2.5}. \tag{4.1}$$

In such situations, if we wish to critique method A, it is not sufficient to demonstrate that

$$M_{sl_A} > \frac{M_c}{2.5}. \tag{4.2}$$

We must deny method B its safety factor, extend the benefit of doubt to method A, and show that

$$M_{sl_A} > M_c. \tag{4.3}$$

To continue with an example that is slightly different from the hypothetical examples above, suppose there is a structure for which a code based procedure gives a safe load of $M_{sl_A} = 4.591 \times 10^3$ Pa. Suppose also that detailed nonlinear simulation shows a collapse load of $M_c = 4.154 \times 10^3$ Pa. Then the code is nonconservative, because it would certify an operational load of, say, $M_{op} = 4.3 \times 10^3$ Pa as safe, when in fact it would be unsafe. The numbers in this example are actually taken from the second computational example in this chapter, and constitute one of the two key demonstrations of nonconservative predictions based on RCC-MR's third method.

In our numerical simulations with various structures and various imperfections, we have found inequality (4.2) easy to achieve. It took persistence, and some luck, to find two structural examples which achieve inequality (4.3). The primary contribution of this

chapter is not in new shell mechanics. It is in finding the examples we present below, which demonstrate conclusively that RCC-MR's third method of imperfection estimation can lead to nonconservative designs in some cases. Since RCC-MR is used to design shell structures for use in nuclear reactors, our results have significant practical implications.

4.3 Safe buckling load as per RCC-MR-A7

Here we present the bare essential components of the safe buckling load calculation as per RCC-MR, Section III, Tome 1, Subsection Z, technical appendix A7. For more details see [18] as well as our summary thereof in [29].

A linear stress analysis and an eigenvalue-based buckling analysis are first carried out under a notional load (N) on the perfect geometry. From these two analyses, we obtain a maximum "primary" stress intensity as well as a buckling load factor λ respectively.

The primary elastic stress intensity S_e (in a von Mises sense) is obtained by taking the membrane stress P_m, and adding to it tensorially the bending stress if the location of interest is away from a point of discontinuity on the shell[1].

For the perfect hemispherical shell under uniform external pressure, $S_e = P_m$, uniform over the entire structure.

The buckling load factor (λ), obtained using routine linear buckling analysis, is multiplied with the maximum stress intensity S_e above, to compute a critical elastic buckling stress (σ_c). Then the rigidity parameter ζ is computed using the material yield stress σ_y as

$$\zeta = \frac{\sigma_c}{\sigma_y}. \tag{4.4}$$

Next, we quantify the geometrical imperfection δ. RCC-MR code allows three methods for the same, as mentioned above. In the first method the maximum deviation d between the real and nominal shell geometry, measured normal to the nominal shell surface, is

[1]Bending stresses near points of discontinuity are called secondary stresses, and not included.

divided by the shell thickness t, i.e.,

$$\delta = \frac{d}{t}. \tag{4.5}$$

In this chapter, we have no comment on RCC-MR's second method of imperfection quantification.

The third method proceeds as follows. A new elastic stress analysis is carried out using the notional load N on a *hypothetical* imperfect structure. The imperfect structure is generated by superposing on the perfect geometry a displacement pattern corresponding to the first elastic buckling mode. The size of the imperfection is chosen so that the maximum deviation between the perfect and the hypothetical-imperfect geometry, measured normal to the nominal shell surface, is the same d as used in the first method. From the results of the new stress analysis, the maximum elastic stress intensity S_d is computed, including *both* membrane and bending stresses, and including secondary stresses if any. The new imperfection quantity is taken as

$$\delta = \frac{1}{6}\left(\frac{S_d}{P_m} - 1\right), \tag{4.6}$$

with P_m as defined above.

With ζ and δ computed as above, we compute the reduction factor X from charts provided in RCC-MR. Note that ζ and δ are just two positive numbers obtained from stress analysis as described above, and the knock-down factor X depends only on ζ and δ, regardless of whether δ is obtained using the first method (Eq. (4.5)) or the third method (Eq. (4.6)).

Finally, the safe load for the structure is defined as the notional load N times the load multiplying factor λ times the knock-down factor X divided by a further safety factor of

5/2, i.e.,

$$\text{Safe load} = \frac{(\text{Notional load } N) \times (\lambda \text{ from eigenvalue analysis}) \times X}{2.5}. \tag{4.7}$$

In an alternative calculation, when the critical elastic stress (here, σ_c) contains a contribution from bending stresses as well (here, it does not), then a safety factor of 5/3 must be used; but if the resulting load exceeds that from Eq. (4.7) obtained using a membrane stress only, then Eq. (4.7) must be used. In other words, the calculation must be done twice, once including bending stresses and once not including them, with different safety factors for the two cases, and the *lesser* of the two computed loads must be taken as the safe load.

The reader may note that a shape perturbation using the first buckling mode shape has indeterminate sign. In other words, two shape perturbation directions can be considered, sometimes giving two different answers. RCC-MR does not comment on this issue. We will revisit it below.

Another important issue is that in this chapter we work with two different types of shape perturbations. The first is a deterministic shape perturbation proportional to the first buckling mode shape, as discussed in this section, following the third method of design from RCC-MR. The actual shape perturbation in the structure may be different. In particular, to obtain a low value of a rigorous upper bound M_c (see item 4, section 4.2), we are free to choose any shape perturbation we like.

4.4 Linear elastic finite element modeling

Our goal is to present two specific design examples to show that RCC-MR's third method of imperfection quantification can be nonconservative. We now present the linear elastic calculations required for our examples.

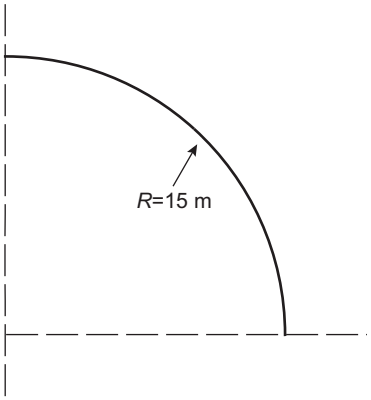

Figure 4.1: Schematic diagram of hemispherical shell.

The shell material is taken to be stainless steel 316 LN, for which reduction factor charts are given in RCC-MR. The operating temperature is assumed to be 20°C. The modulus of elasticity, Poisson's ratio and yield stress (σ_y) for SS 316 LN are 2×10^{11} Pa, 0.3 and 220×10^6 Pa respectively [46].

4.4.1 Geometry

Hemispherical shell

Our first example is a hemispherical shell with radius $R = 15$ m and thickness $t = 8 \times 10^{-3}$ m. Figure 4.1 shows the perfect geometry. For our example we have adopted a dimensional imperfection $d = \frac{t}{2}$ (recall Eq. (4.5)), i.e., 4×10^{-3} m. This imperfection value is not to be considered large. It is (i) a tiny percentage of the shell's radius, (ii) well within what the code allows, and (iii) recommended by some authors for practical design (e.g., [50], pp. 608).

The shell is subjected to uniform external pressure, with a notional value of $N = 1 \times 10^4$ Pa. The boundary conditions at the bottom are: no rotations, no vertical displacements, and no radial restraints. Our code-based analysis for the hemispherical shell is axisymmetric, because separate three dimensional simulations showed no relevant non-axisymmetric modes (details omitted). An axisymmetric buckling mode has been used by others as well

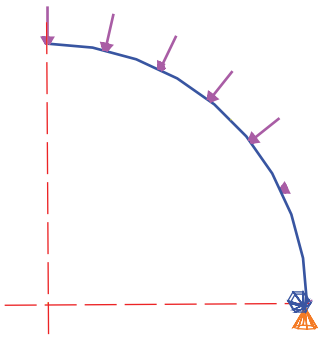

Figure 4.2: ABAQUS model of hemispherical shell with external pressure.

[51, 52].

Figure 4.2 shows an ABAQUS model of the hemispherical shell. We have used axisymmetric thin shell elements, SAX1, in ABAQUS for all our axisymmetric simulations.

Torispherical shell

Our second example is a torispherical shell with a crown radius of $R_1 = 30$ m and a knuckle radius $R_2 = 6$ m. Figure 4.3 shows the perfect geometry. The shape of the torispherical dished end requires two more parameters, for which we have used $a = 4$ m and $\phi = 81°$. The dimension b can be found in terms of R_1, R_2, a and ϕ, and turns out to be 23.6646 m. The shell thickness is taken to be 8×10^{-3} m. The dimensional imperfection we will use is 4×10^{-3} m.

The torispherical shell is subjected to uniform external pressure, with a notional value of $N = 1 \times 10^4$ Pa. The boundary conditions at the bottom are: no translational displacements, except radial displacement is allowed.

Since the first buckling mode shape of the torispherical shell is non-axisymmetric, we have modeled this shell using the three dimensional element S4R in ABAQUS. Figure 4.4 shows an ABAQUS model of the torispherical shell.

Next, mesh convergence is examined.

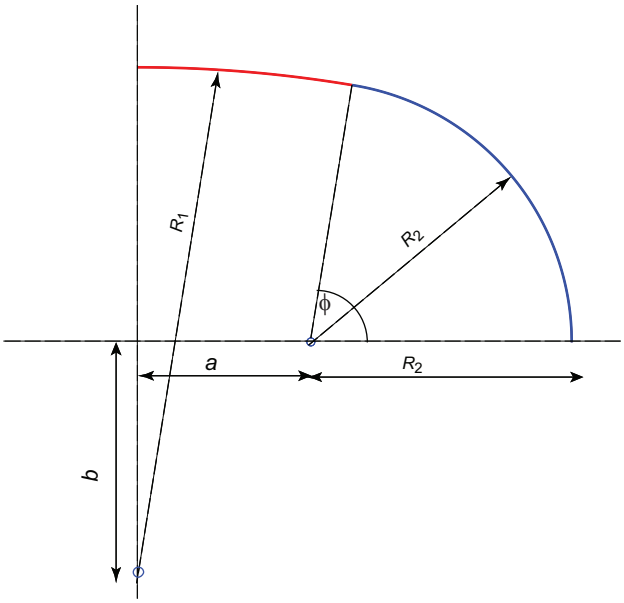

Figure 4.3: Schematic sketch of torispherical shell.

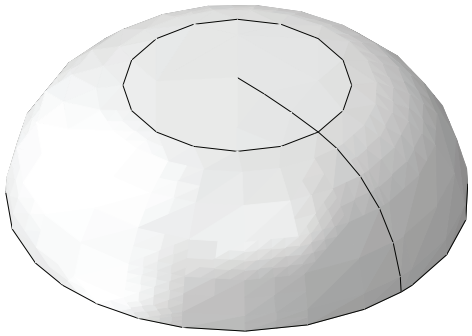

Figure 4.4: ABAQUS model of torispherical shell.

4.4.2 Mesh convergence

Mesh convergence studies were carried out for the strain energy for the perfect shell, and for S_d for an imperfect shell perturbed by the first buckling mode shape.

For the perfect hemispherical shell, successive finite element models were created with element sizes (h_e) of 0.4 m, 0.2 m, 0.1 m, 0.05 m, 0.025 m and 0.0125 m (these are actually element "seed" sizes specified to ABAQUS, which then carries out automated meshing). A series of linear stress and buckling analyses were carried out. Figure 4.5 (a) shows the strain energy obtained against the reciprocal of element size h_e.

Next, a series of linear stress analyses were carried out on the perturbed shell geometry,

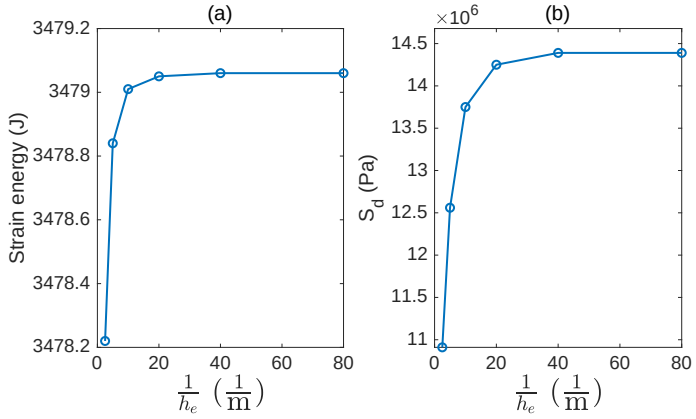

Figure 4.5: Mesh convergence for the hemispherical shell. (a) Strain energy of perfect hemispherical shell. (b) S_d in imperfect hemispherical shell.

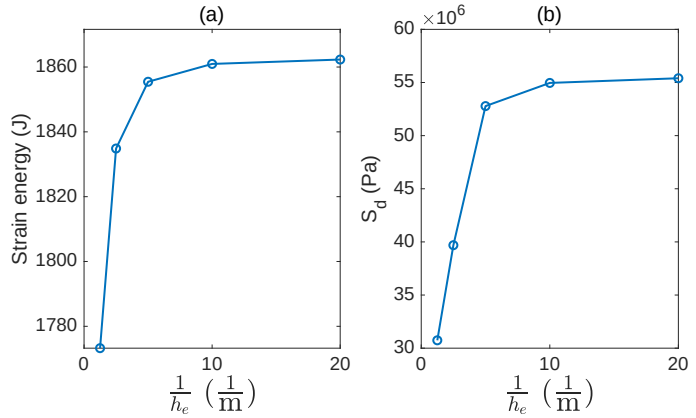

Figure 4.6: Mesh convergence for the torispherical shell. (a) Strain energy of perfect torispherical shell. (b) S_d in imperfect torispherical shell.

with a shape perturbation proportional to the first buckling mode shape, and with the maximum imperfection introduced being 4×10^{-3} m ($\delta = 0.5$ as per Eq. (4.5)). The maximum elastic stress intensity S_d was computed for each mesh size. Figure 4.5 (b) shows S_d against the reciprocal of element size h_e.

Based on this convergence study, the results from the mesh with $h_e = 0.0125$ m were adopted for the hemispherical shell.

For the torispherical shell, because a three dimensional mesh was used, the element sizes adopted were slightly larger. Successive finite element models were created for element sizes of 0.8 m, 0.4 m, 0.2 m, 0.1 m and 0.05 m. Linear stress and buckling analyses were carried out for these meshes. Figure 4.6 (a) shows the strain energy obtained against

the reciprocal of element size h_e. Next, a series of linear stress analyses were carried out on an imperfect shell geometry perturbed by the first buckling mode shape, with largest deviation equal to 4×10^{-3} m. Figure 4.6 (b) shows S_d thus obtained against the reciprocal of element size h_e. Based on this convergence study, the results from the mesh with $h_e = 0.05$ m were adopted for the torispherical shell.

We will now compute safe buckling load as per RCC-MR.

4.5 Safe buckling load as per RCC-MR

4.5.1 Hemispherical shell

First, linear stress and buckling analyses on the perfect geometry are carried out, as described above. Figure 4.7 shows the first buckling mode of the hemispherical shell. The linear buckling load factor (λ) from buckling analysis is 6.8846. Figure 4.8 shows that the membrane stress distribution is constant in the perfect hemispherical shell, with $P_m = 9.376 \times 10^6$ Pa.

Recalling Eq. (4.4), we obtain

$$\zeta = \frac{\lambda \times P_m}{\sigma_y} = \frac{6.8846 \times 9.376 \times 10^6 \text{ Pa}}{220 \times 10^6 \text{ Pa}} = 0.2934. \tag{4.8}$$

As per RCC-MR's first method for quantifying imperfection, $\delta = 0.5$ (Eq. (4.5)).

To compute δ as per RCC-MR's third method, an additional linear stress analysis is carried out on a perturbed geometry, with a maximum geometrical deviation of 4×10^{-3} m. Figure 4.9 shows the resulting stress distribution (von Mises); S_d is found to be 14.39×10^6 Pa.

The imperfection δ, as per the third method or Eq. (4.6), is

$$\delta = \frac{1}{6}\left(\frac{S_d}{P_m} - 1\right) = \frac{1}{6}\left(\frac{14.39 \times 10^6 \text{ Pa}}{9.376 \times 10^6 \text{ Pa}} - 1\right) = 0.0891, \tag{4.9}$$

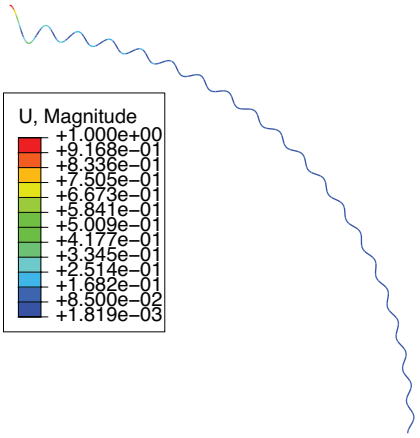

Figure 4.7: First buckling mode of hemispherical shell (displacements (unit: m) are exaggerated, the maximum displacement shown is 187.5 times the shell thickness).

which is much smaller than 0.5.

As explained earlier, it now remains only to compute the knock-down factor X, which is a function of ζ (found to be 0.2934, see Eq. (4.8)) and δ (equal to 0.5 by definition, if following the first method; and equal to 0.0891, if using the third method or Eq. (4.9)). The difference is significant.

With $\zeta = 0.2934$ and $\delta = 0.5$, X is 0.413 from RCC-MR's chart for unstable post-buckling response. The safe pressure is then (recall Eq. (4.7))

$$\frac{(\text{Notional load } N) \times (\lambda) \times X}{2.5} = \frac{(1 \times 10^4 \text{ Pa}) \times (6.8846) \times 0.413}{2.5} = 11.37 \times 10^3 \text{ Pa}. \tag{4.10}$$

With $\zeta = 0.2934$ and $\delta = 0.0891$, in contrast, X is 0.6877 from the same chart. The corresponding safe external pressure from RCC-MR's chart is (Eq. (4.7))

$$\frac{(\text{Notional load } N) \times (\lambda) \times X}{2.5} = \frac{(1 \times 10^4 \text{ Pa}) \times (6.8846) \times 0.6877}{2.5} = 18.938 \times 10^3 \text{ Pa}. \tag{4.11}$$

Hence, the safe pressure computed using the third method of imperfection estimate

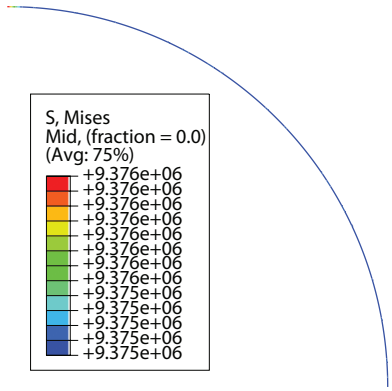

Figure 4.8: The membrane stress (unit: Pa) in hemispherical shell.

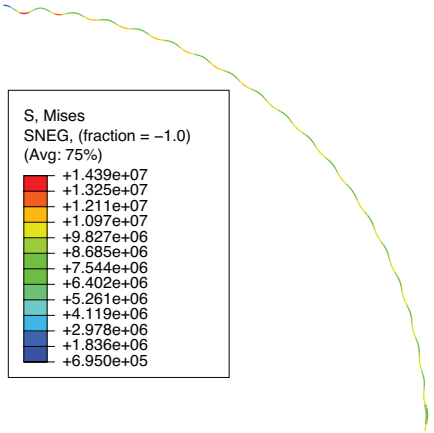

Figure 4.9: von Mises stress (unit: Pa) distribution in the perturbed hemispherical shell geometry. Displacements are exaggerated: the magnification factor is 500.

is 18.938×10^3 Pa. If we consider the imperfection to be in the opposite direction, the computed safe buckling pressure is 13.772×10^3 Pa (details omitted).

4.5.2 Torispherical shell

As before, linear stress and buckling analyses on the perfect geometry are carried out first. Figure 4.10 shows the first buckling mode of the torispherical shell. The linear buckling load factor (λ) from buckling analysis is 1.6885. Figure 4.11 shows the membrane stress distribution in the perfect torispherical shell, with $P_m = 35.01 \times 10^6$ Pa. The maximum membrane plus bending stress (S_e) occurs at the geometrical discontinuity in the toripshrical shell. As per the code, these stresses are considered as secondary stress

(see RCC-MR, Section III, Tome 1, Subsection B, table RB 3324.31 (pp. 97)); hence these are not included and P_m is used for S_e.

We now proceed to compute ζ, and δ from the first and third methods.

Recalling Eq. (4.4), we obtain

$$\zeta = \frac{\lambda \times P_m}{\sigma_y} = \frac{1.6885 \times 35.01 \times 10^6 \text{ Pa}}{220 \times 10^6 \text{ Pa}} = 0.2687. \tag{4.12}$$

As per RCC-MR's first method, $\delta = 0.5$ (Eq. (4.5)).

To compute S_d for use with the third method, we perturb the nominal geometry with the first buckling mode such that the maximum geometrical deviation induced is 4×10^{-3} m. Figure 4.12 shows the resulting stress distribution (von Mises); S_d is found to be 55.40×10^6 Pa.

The new imperfection quantity, as per the third method or Eq. (4.6), is

$$\delta = \frac{1}{6}\left(\frac{S_d}{P_m} - 1\right) = \frac{1}{6}\left(\frac{55.40 \times 10^6 \text{ Pa}}{35.01 \times 10^6 \text{ Pa}} - 1\right) = 0.097, \tag{4.13}$$

which is much smaller than 0.5.

With $\zeta = 0.2687$ and $\delta = 0.5$, X is 0.4233 from RCC-MR's chart for unstable post-buckling response. The safe pressure is then (recall Eq. (4.7))

$$\frac{(\text{Notional load } N) \times (\lambda) \times X}{2.5} = \frac{(1 \times 10^4 \text{ Pa}) \times (1.6885) \times 0.4233}{2.5} = 2.859 \times 10^3 \text{ Pa}. \tag{4.14}$$

With $\zeta = 0.2687$ and $\delta = 0.097$, in contrast, X is 0.6797 from the same chart. The corresponding safe external pressure, by the third method, is (Eq. (4.7))

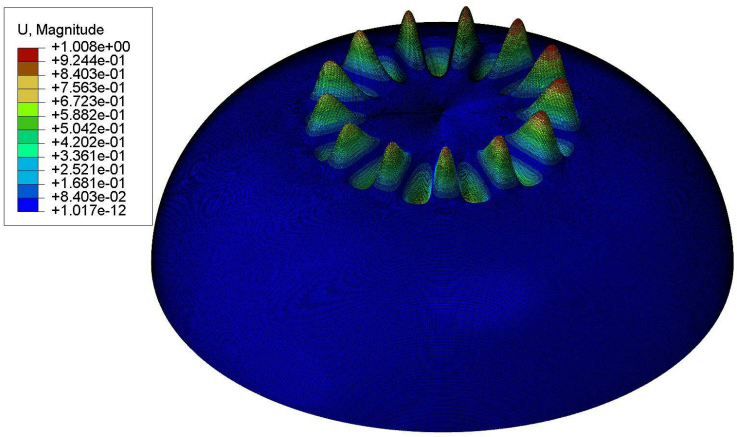

Figure 4.10: First buckling mode of the torispherical shell. Displacement (unit: m) are exaggerated. The maximum displacement is 250 times the shell thickness.

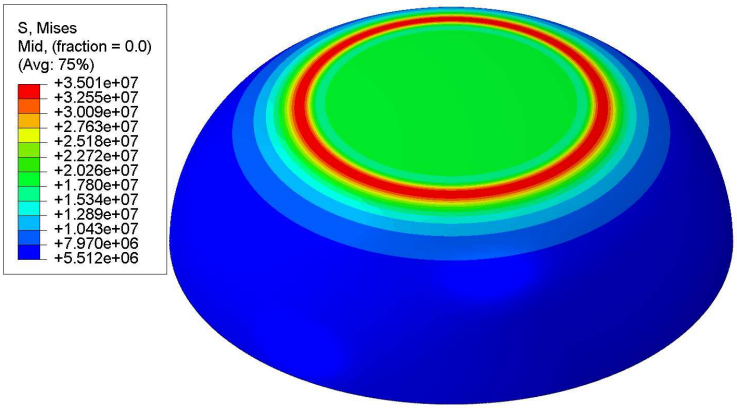

Figure 4.11: Membrane stress (unit: Pa) distribution in the perfect torispherical shell.

$$\frac{(\text{Notional load } N) \times (\lambda) \times X}{2.5} = \frac{(1 \times 10^4 \text{ Pa}) \times (1.6885) \times 0.6797}{2.5} = 4.591 \times 10^3 \text{ Pa}. \tag{4.15}$$

Hence the safe pressure computed using the third method of imperfection estimate is 4.591×10^3 Pa. Unlike the hemispherical shell, in this case an imperfection assumed in the opposite direction has a negligible effect: the safe buckling pressure obtained is 4.584×10^3 Pa.

This concludes our computation of the safe buckling loads of the two structures (hemispherical and torispherical) using both the first and third methods of imperfection quan-

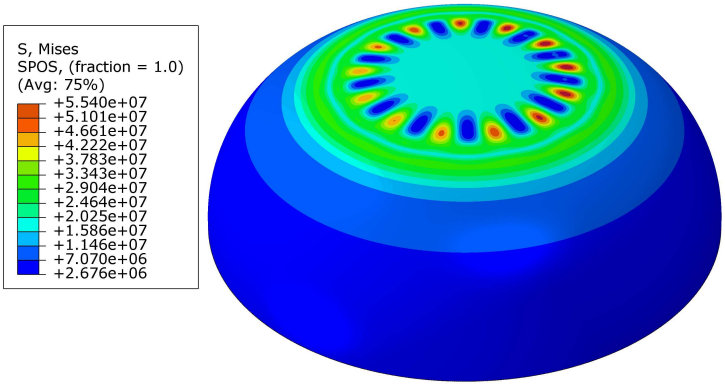

Figure 4.12: von Mises stress (unit: Pa) distribution in the perturbed torispherical shell geometry.

tification of RCC-MR. We now proceed to compute rigorous upper bounds M_c for these safe loads, using nonlinear elastic buckling analysis (recall item 4 of section 4.2).

4.6 Nonlinear buckling analysis

In this section we will present fully nonlinear and detailed simulations of post-buckling response of our shells using ABAQUS.

In order to validate and verify our nonlinear analysis procedure, we have first reproduced the result of a nonlinear buckling analysis of an imperfect spherical shell reported and discussed in [53]. Details are presented in appendix 6.4.

We now proceed with analyses with our own shell geometries.

4.6.1 Hemispherical shell

Geometry

As mentioned at the end of section 4.3, the actual imperfection in the structure need not be in the shape of the first buckling mode. Imperfections in structures that are yet to be manufactured are, unavoidably, unknown at the design stage. Hence, for safe design load calculations using nonlinear analysis, there is no restriction on the imperfection shape

to be used in analysis. We are allowed to consider any shape, subject only to the δ we specify as part of the design, which in the present case means that the maximum deviation $d = 4 \times 10^{-3}$ m.

Here, the imperfect geometry of the hemispherical shell used for nonlinear analysis is generated by superimposing an axisymmetric dimple shaped imperfection on the perfect geometry. The dimple is located at the pole, as discussed in [51, 52]. It is emphasized that the dimple as imperfection shape is realistic and important, although it does not match the elastic bucking mode shape. From previous experimental and theoretical studies, it is known that a spherical shell under external pressure buckles in the form of such a dimple [47, 53, 54].

Using polar coordinates (r, θ) to generate the axisymmetric shape, with r in m and θ in radians, we adopt

$$r(\theta) = R + d \times \left(1 - 2e^{-800\left(\theta - \frac{\pi}{2}\right)^2}\right) - d \times \epsilon_1(\theta), \tag{4.16}$$

where $\epsilon_1(\theta)$ is defined as below:

$$\epsilon_1(\theta) = \begin{cases} -\frac{1}{1.4661} \times \theta + 1 & 0 \leq \theta \leq 1.4661 \,(\text{which is } 84^\circ) \\ 0 & 1.4661 < \theta \leq \frac{\pi}{2}. \end{cases} \tag{4.17}$$

The numerical parameters above were selected after some trial and error.

Finally, Cartesian coordinates of the imperfect axisymmetric hemispherical shell profile are computed as

$$x = r(\theta) \times \cos(\theta), \quad y = r(\theta) \times \sin(\theta), \tag{4.18}$$

which we used for inputs to ABAQUS.

The shape perturbation used is shown in Fig. 4.13, exaggerated by a factor of 100.

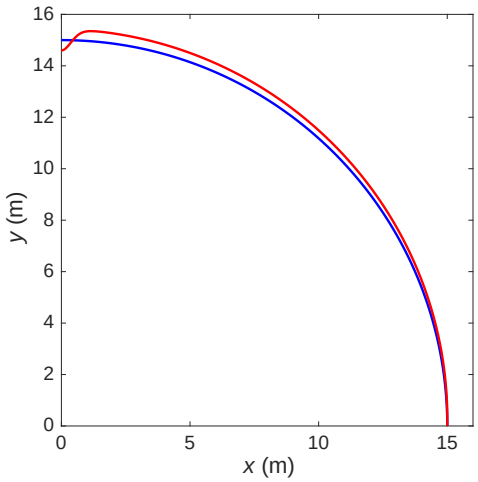

Figure 4.13: The shape perturbation in the hemispherical shell, exaggerated by a factor of 100. Coordinates x and y are in m.

Figure 4.14 (a) shows a zoomed view of the actual imperfection, where imperfect and perfect shells are plotted together with shell thickness shown to scale. The dashed lines show the perfect shell, and solid lines show the imperfect shell. Further, Fig. 4.14 (b) shows both imperfect and perfect hemispherical shells on a larger scale, plotted together with shell thickness, to emphasize how small the imperfection really is. In Fig. 4.14 (b), perfect and imperfect shells are indistinguishable to plotting accuracy. It will be seen below that even this tiny imperfection has a significant effect on the collapse load.

Nonlinear analysis

We have used two separate nonlinear buckling analysis procedures, 'Static, General' and 'Static Riks', both available in ABAQUS. In 'Static, General', the load is applied incrementally and the Newton-Raphson method is used to find a solution after each load increment. The load at which the method fails to converge is called the collapse load. In 'Static Riks' analysis, an arc length technique is used to compute the peak load as well as post-buckling response of the structure.

In both approaches, the linear elastic buckling pressure ($P_{cr} = 68.846 \times 10^3$ Pa) is applied as the reference load. Collapse occurs before this load is reached. The ratio of

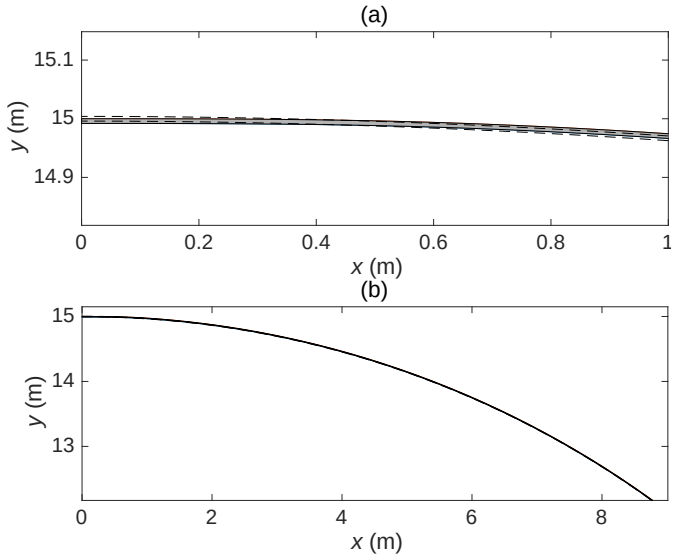

Figure 4.14: Perfect (dashed lines) and imperfect hemispherical shells (solid lines), with shell thickness shown. Coordinates x and y are in m. (a) Zoomed region near the pole shows small imperfection. (b) On a larger scale, the two geometries look indistinguishable.

maximum load sustained to the reference load is referred to below as the reduction factor from nonlinear analysis. Plasticity is irrelevant in our analysis because the maximum stress in the hemispherical shell at its maximum or collapse load is less than the material yield stress. In fact, we have run the simulation both in purely geometrically nonlinear elastic mode as well as in elastic-plastic mode, and obtained the same results, as expected.

Figure 4.15 shows the load displacement plot of the imperfect hemispherical shell obtained from both analysis procedures. The displacement at the pole location is depicted in the plot. The reduction factor from both analysis procedures was 0.2403. On multiplying this reduction factor with the reference pressure (68.846×10^3 Pa), we obtain the maximum buckling pressure from nonlinear analysis as 16.544×10^3 Pa. Figure 4.16 shows the von Mises stress distribution in the hemispherical shell at maximum load. The maximum stress in the structure at that load is 128.9×10^6 Pa, which is less than the yield stress.

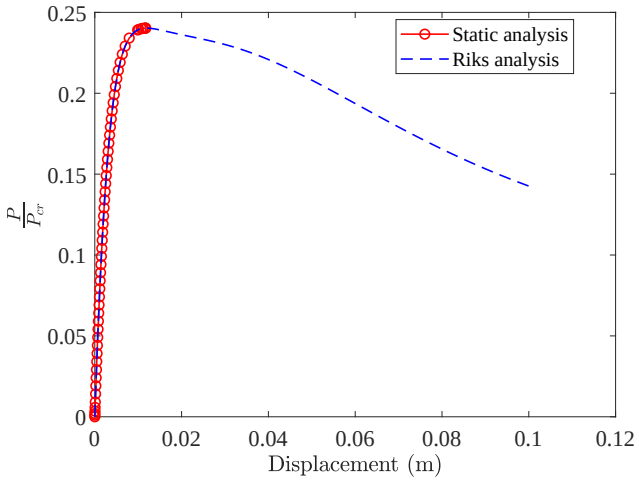

Figure 4.15: Load displacement plot of the hemispherical shell.

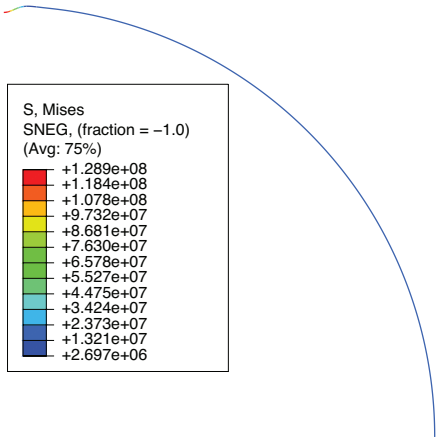

Figure 4.16: von Mises stress (unit: Pa) distribution in the hemispherical shell at maximum load.

4.6.2 Torispherical shell

Geometry

The imperfect geometry of the torispherical shell for nonlinear buckling analysis is constructed by introducing an axisymmetric dimple at the pole location of the perfect geometry, similar to that used for the hemispherical shell. An interesting observation from nonlinear buckling analysis conducted using three dimensional simulations (details omitted) is that the buckling is axisymmetric, and so this section presents an axisymmetric

analysis with a refined mesh (0.0125 m). There is no contradiction in the buckling of the axisymmetric imperfect structure being axisymmetric, although the first elastic buckling mode shape of the perfect shell is non-axisymmetric as noted in section 4.5.2. The collapse load obtained using axisymmetric nonlinear analysis is still a rigorous upper bound on the safe load of the structure.

Cartesian coordinates of the perfect axisymmetric torispherical shell are obtained using separate formulas for the crown and knuckle regions as below (recall Fig. 4.3). In the crown region,

$$y = b + \sqrt{R_1^2 - x^2}, \qquad 0 \le x \le R_2 \cos(\phi) + a. \tag{4.19}$$

In the knuckle region,

$$x = R_2 \cos(\theta) + a, \quad y = R_2 \sin(\theta), \qquad 0 \le \theta \le \phi. \tag{4.20}$$

The imperfect geometry is defined using polar coordinates as follows. Using the Cartesian coordinates of the perfect profile as given above, we first define

$$r = \sqrt{x^2 + y^2}, \qquad \psi = \arctan\left(\frac{y}{x}\right), \tag{4.21}$$

where r is in m and ψ is in radians. We define a defect

$$r_d = d \times \left(1 - 2e^{-70\left(\psi - \frac{\pi}{2}\right)^2}\right) - d \times \epsilon_1(\psi), \tag{4.22}$$

where

$$\epsilon_1(\psi) = \begin{cases} -\frac{1}{1.0472} \times \psi + 1 & 0 \le \psi \le 1.0472 \\ 0 & 1.0472 \le \psi \le \frac{\pi}{2}. \end{cases} \tag{4.23}$$

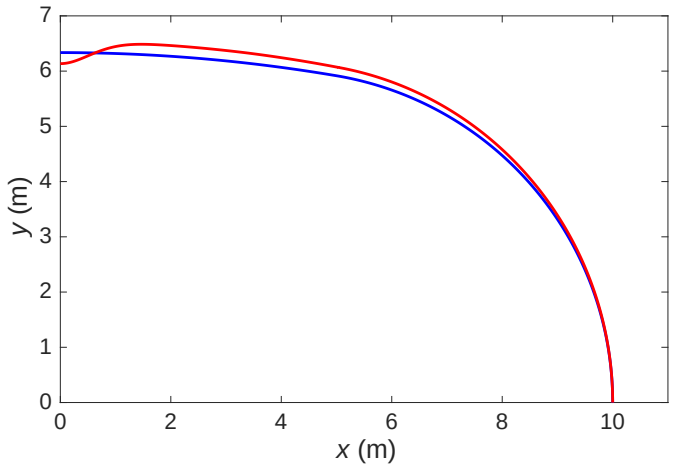

Figure 4.17: The shape perturbation in the torispherical shell, exaggerated by a factor of 50. Coordinates x and y are in m.

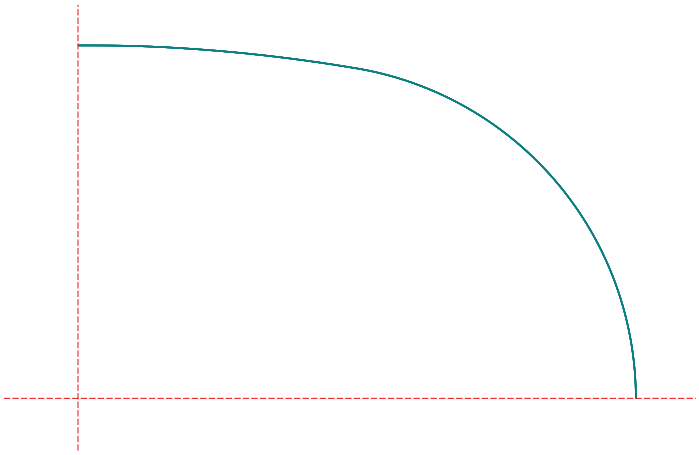

Figure 4.18: ABAQUS model of imperfect torispherical shell (axisymmetric).

Finally, we define the Cartesian coordinates of the imperfect geometry as

$$x_d = x + r_d \cos(\psi), \quad y_d = y + r_d \sin(\psi). \tag{4.24}$$

The shape perturbation used is shown in Fig. 4.17, exaggerated by a factor of 50. The actual imperfection is tiny, as was the case for the hemispherical shell. Figure 4.18 shows the ABAQUS model of the imperfect torispherical shell.

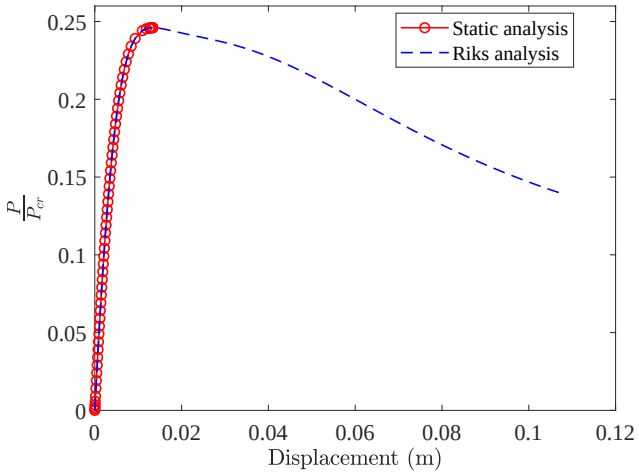

Figure 4.19: Load displacement plot of the torispherical shell.

4.6.3 Nonlinear analysis

As before, we have used both 'Static, General' and 'Static Riks' procedures to compute the nonlinear collapse load. The linear elastic buckling pressure (P_{cr}) is 16.885×10^3 Pa, and is taken as the reference load. Plasticity is excluded because the maximum stress at the peak load is below yield.

Figure 4.19 shows the load displacement plot of the imperfect torispherical shell obtained from both analyses. The displacement at the pole location is depicted in the plot. The reduction factor from both analysis procedures is 0.2460. On multiplying this reduction factor with the reference pressure of 16.885×10^3 Pa, the buckling pressure (collapse load) from nonlinear analysis is found to be 4.154×10^3 Pa. Figure 4.20 shows the von Mises stress distribution in the torispherical shell at the collapse load. The maximum stress at that load is 64.83×10^6 Pa, well below yield.

4.7 Discussion and conclusions

The safe load for our hemispherical shell using RCC-MR's third method of imperfection quantification was 18.938×10^3 Pa (see Eq. (4.11)), while the collapse load from nonlinear analysis above was 16.544×10^3 Pa. Since the latter is a rigorous upper bound for the safe

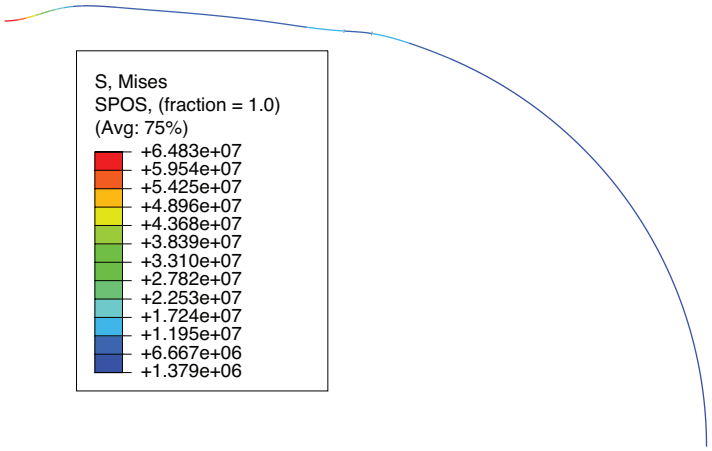

Figure 4.20: von Mises stress (unit: Pa) distribution in the torispherical shell at maximum load. Deformations are exaggerated: the magnification factor is 20.

load, we conclude that the third method is nonconservative for this structure by a factor of about 8/7. As mentioned above, however, the shape perturbation used for RCC-MR's third method could in principle have been assigned the opposite sense (the code does not specify which sense should be used). With the imperfection taken in the opposite sense, the third method would have predicted a safe load of 13.772×10^3 Pa, which would be conservative.

The above dilemma, however, disappears for the torispherical shell example, where imperfections in both directions give essentially the same results. For the torispherical shell, the safe load using RCC-MR's third method of imperfection quantification was 4.591×10^3 Pa (see Eq. (4.15)), while the collapse load from nonlinear analysis above was 4.154×10^3 Pa. Thus, for this structure, RCC-MR's third method is unequivocally nonconservative by a factor of about 11/10.

It is emphasized that in RCC-MR, design based on full nonlinear simulation with imperfections prescribes a further safety factor of 2.5 which we have denied ourselves here[2] in order to extend the maximum possible benefit of doubt to RCC-MR's third method. Otherwise, the nonconservativeness factor would be higher than 11/10.

[2]The American Society of Mechanical Engineers (ASME) [55] recommends a safety factor of 3.

The low reduction factors obtained from the above nonlinear analyses of imperfect shells are not surprising. Buckling experiments with hemispherical shells under external pressure have exhibited similar low reduction factors (see chapter 9 of [34]). Computational buckling studies of hemispherical shells under external pressure have also exhibited similarly low reduction factors, see [51, 53]. In fact, our choice of the hemispherical shell example in this chapter for critiquing RCC-MR's third method was prompted by these works. We are not aware of similar studies with torispherical shells, but the similarity of the reduction factor values between the two shells is encouraging from the viewpoint of our critique. Finally, due to the indeterminacy of the direction of shape perturbation adopted, for the purposes of this chapter, the spherical shell example is not conclusive. For this reason, we have constructed the torispherical shell example, after some trial and error, to provide an unequivocal demonstration of nonconservativeness in the third method.

As explained in section 4.2, our precisely described, purely below plastic yielding, finely meshed, geometrically nonlinear buckling calculations using a reliable and widely available computational package (ABAQUS) provide rigorous upper bounds on the safe load. Due to unmodeled effects, these bounds may not be achieved by real structures, and failure may actually occur at even lower pressures. This is why the code specifies a further safety factor of 2.5 on these estimates. For this reason, we suggest that for practical structures the nonconservativeness of the third method may be even greater than 11/10 in some cases.

We conclude this chapter by reiterating that, overall, we have great respect for RCC-MR, which is used heavily for structural design of nuclear components in several countries including India. However, the third method of imperfection estimation for elastic analysis-based buckling design of thin shells in RCC-MR requires reexamination by the appropriate scientific authorities.

Chapter 5

Conclusions

This thesis has presented large-sample buckling experiments of two shells, highlighting large variability among buckling loads of shells and in the post-buckling response. With motivation and insights from the buckling experiments, we presented three design examples for which the third method of imperfection estimation within RCC-MR leads to surprisingly high estimate of safe buckling loads. We have also shown that the third method of imperfection estimation leads to unequivocally nonconservative buckling loads in some cases. Such a demonstration for this design code is missing from the literature to the best of our knowledge.

In chapter 2, we presented 100 buckling experiment, each, of two shells geometries. One shell geometry is a dome-shaped shell with a flat base, and another shell is a truncated conical shell with a flat base. We have provided a detailed geometric and material characterization of the thin shell specimens. The experiments show that both shells undergo plastic buckling.

The buckling load displacement curves of 100 bowls show stable post-buckling response and variability in buckling loads by a factor of 2. The buckling load-displacement curves for 100 conical shell specimens show significant variations in buckling load, by as much as a factor 5, and unstable post-buckling response. Our results demonstrate large variability

in the buckling loads of thin shells, seen more clearly here because the sample size used is large.

We attributed large variability in the buckling load of conical shells to the presence of high curvature in the vicinity of contact loading. The interaction of contact loading and geometric imperfection results in significant variability in buckling loads.

To demonstrate this, we have carried out two sets of axisymmetric elastoplastic finite element simulations of the conical shell. In the first set of simulations, tractions are directly applied to the conical shell. In the second set of simulations, we applied the load through contact with a rigid plate. The second set of simulations show approximately twice as much sensitivity to geometrical imperfections, validating our hypothesis.

The following are the salient deductions from large-sample buckling experiments of two thin shells.

First, in the case of shell designs, where loads are transferred through contact, the factor of safety need to be reassessed in design procedures that are purely based on linear analysis. Such procedures do not account for the complex interaction of loading and geometry and may result in an unrealistically higher safe buckling load. Hence, in design codes like RCC-MR, the factor of safety for such design cases should be reexamined.

Second, experimental load-displacement curves of conical shells highlight that shells with unstable post-buckling responses require particular care during design. For example, consider a safety-critical shell, like a large diameter nuclear reactor vessel with unstable post-buckling behaviour, designed for static loads using the design code. During reactor operation, it may be subjected to earthquake loads (with low probability). In case an earthquake does occur, then due to dynamic forces, the reactor vessel may undergo transient displacements and switch to an unstable regime in the load-displacement curve. Such phenomena may result in collapse of the vessel due to dynamic loads well below the static buckling load. Such issues need to be incorporated into design procedures and code

in clear and simple ways.

Third, large-sample experiments exhibited significant variability in buckling loads, as much as a factor of 5 for conical shells. Design procedures in design codes rely on buckling experiments for deriving factors of safety [19, 20]. Hence our experiments highlight the importance of a large test matrix of shells for more reliable design procedures.

Fourth, our experimental results provide a rich input source for developing computational models of plastic buckling. We hope that more detailed three-dimensional simulations in future work may yield greater understanding of factors contributing to the surprisingly large variability observed in buckling experiments.

In chapter 3, we examined the third method of RCC-MR using some detailed numerical examples. The first example is a nonuniform cylindrical shell closed at one end with a spherical endcap under external pressure. This example showed that the buckling displacements might be localized to regions away from high-stress regions. Also, the perturbation in the shape of the buckling mode may result in a newly computed imperfection value, which is independent of the actual imperfection. Hence, the safe buckling load of the shell becomes independent of its actual imperfection, which contradicts the broad shell buckling experience. This is an unexpected finding with potentially serious consequences, and provides a warning against use of this "third method" from RCC-MR.

The second example is a cylinder with an ellipsoidal head under internal pressure. With this example, we showed that even after perturbation, the ratio of S_d/P_m might not be significantly higher than unity, resulting in tiny imperfections estimates and unrealistically high safe buckling loads. The third example is an L-shaped pipe with an end load. In this example, like the second example, the newly computed imperfection quantity is very small compared actual value used for computations (e.g., 25 times smaller), leading to an unrealistically high safe buckling load.

We concluded chapter 3 by noting that a designer trusts the design code. Hence

when he or she finds that as per code-backed calculations, the safe buckling load of a design structure is both high and independent of physical imperfection, the designer may be tempted to lower wall thicknesses to achieve other technical goals in their specific application, potentially increasing nonconservativeness.

In chapter 4, we proved the nonconservatism of the third method of RCC-MR by using two design examples. We also explained why proving such nonconservatism is difficult using experiments or with large material nonlinearity in simulations.

Our two design examples are a spherical shell and a torispherical shell, both under external pressure. We have shown that compared to nonlinear finite element simulations, the third method overpredicts the collapse load of imperfect shells by factors of about 8/7 and 11/10. While proving nonconservatism, we have denied a safety factor of 2.5 to ourselves, in order to give the third method benefit of the doubt.

We concluded chapter 4 by emphasizing that overall, we have great respect for RCC-MR, which is used heavily for the structural design of nuclear components in several countries including India. However, the third method of imperfection estimation for elastic analysis-based buckling design of thin shells in RCC-MR requires reexamination by appropriate scientific authorities.

Chapter 6

Appendix

6.1 P_m and $P_m + P_b$ calculation

Procedures summarized here (for completeness) are based on *RCC-MR Section III Tome 1 Subsection B*. First the membrane stress tensor is computed from the mean values of individual stress components σ_{ij} averaged across shell thickness (*section RB 3224.12, pp. 25*),

$$(\sigma_{ij})_m = \frac{1}{h} \int_{-h/2}^{h/2} \sigma_{ij} \cdot dx \tag{6.1}$$

where h is the shell thickness and x is a local through-thickness integration variable. Similarly, the bending stress tensor is calculated from the total stress tensor components, each averaged by integration (*section RB 3224.12, pp. 25*), as in

$$(\sigma_{ij})_b = \frac{12s}{h^3} \int_{-h/2}^{h/2} \sigma_{ij} \cdot x \cdot dx \tag{6.2}$$

where s will be chosen as $\pm\frac{h}{2}$ depending on which case gives greater stress severity in combination with $(\sigma_{ij})_m$.

The equivalent stress or stress intensity for a given stress tensor with principal stresses

σ_1, σ_2 and σ_3 is given (*section RB 3224.43, pp. 27*) by

$$\bar{\sigma} = \sqrt{\frac{(\sigma_1 - \sigma_2)^2 + (\sigma_1 - \sigma_3)^2 + (\sigma_3 - \sigma_2)^2}{2}}. \tag{6.3}$$

As per *section RB 3224.51*, primary membrane stress intensity P_m is calculated from principal stresses of the membrane stress tensor as per Eq. (6.3). To calculate $P_m + P_b$, first a membrane plus bending stress tensor is constructed by adding

$$(\sigma_{ij})_{m+b} = (\sigma_{ij})_m + (\sigma_{ij})_b \tag{6.4}$$

and then the $P_m + P_b$ stress intensity is calculated as von Mises stress using the components $(\sigma_{ij})_{m+b}$.

6.2 Mesh convergence studies

In mesh convergence studies, successive mesh models are created by halving the element sizes of previous mesh models.

For the nonuniform cylinder with a spherical cap, the initial mesh model used had an element size (L) of 0.16 m, and successive meshes had element sizes of 0.08 m, 0.04 m, 0.02 m and 0.01 m. For the elliptical head with cylinder, the initial mesh model used had an element size of 0.4 m, and then successive models had element sizes of 0.2 m, 0.1 m, 0.05 m and 0.025 m. For the L-shaped pipe, the initial mesh model had an element size of 0.2 m, with subsequent meshes of 0.1 m, 0.05 m and 0.025 m. Two solution quantities, namely the stress at a critical location in the model and the total strain energy, were used to study convergence for the different models. Both parameters are plotted against $1/L$ (with L in m).

Figures 6.1, 6.2 and Fig. 6.3 show that good convergence was obtained with the element

sizes finally used. The percentage changes observed due to the final refinement steps were tiny in all three cases.

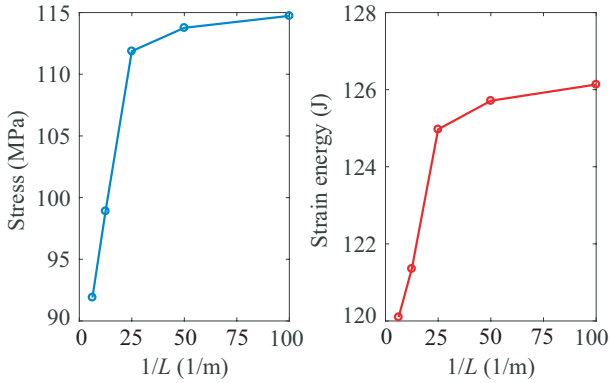

Figure 6.1: Mesh convergence for the nonuniform cylinder with spherical cap. Left: von Mises stress. Right: strain energy.

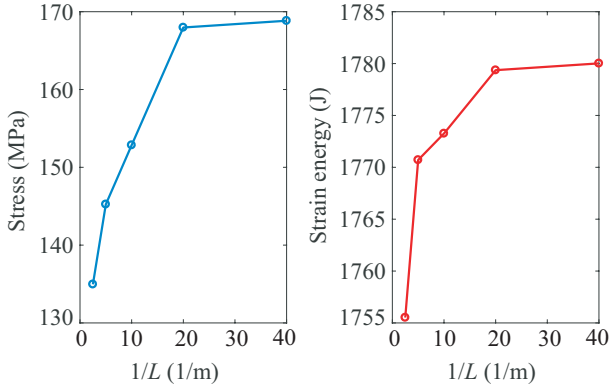

Figure 6.2: Mesh convergence for the ellipsoidal head. Left: von Mises stress. Right: strain energy.

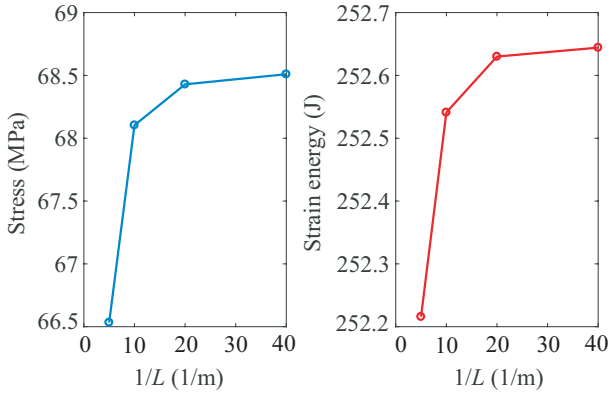

Figure 6.3: Mesh convergence for the L-shaped pipe. Left: von Mises stress. Right: strain energy.

6.3 Safe buckling load calculation details

In this section, we present some safe load calculation details for the ellipsoidal head and the L-shaped shell. It will be seen that, except for our use of Eq. (3.2), we have been conservative in all other ways.

6.3.1 Ellipsoidal head

For the ellipsoidal head, the notional load is $N = 15$ kPa. The location of maximum membrane plus bending stress is not at a structural discontinuity. See Fig. 3.15. Hence we shall compute the safe buckling load comparing the result from both: just the membrane stress intensity P_m as well as the membrane plus bending stress intensity $P_m + P_b$. We shall take the lower permissible load obtained as the safe load.

We will denote the ζ due to membrane stress intensity P_m as ζ_m, and denote the ζ due to membrane plus bending stress intensity $P_m + P_b$ as ζ_{m+b}.

From linear stress analysis, as shown in Fig. 3.15, P_m is 153.4 MPa and $P_m + P_b$ is 171.25 MPa. From linear buckling analysis, the load multiplier $\lambda = 3.45$. We obtain

$$\zeta_m = \frac{153.4 \times 3.45}{220} \approx 2.41 \tag{6.5}$$

and

$$\zeta_{m+b} = \frac{171.25 \times 3.45}{220} \approx 2.69. \tag{6.6}$$

First let us consider membrane stress intensity alone. For actual defect $d/h = 1.5$, we obtain from charts $X_m(\zeta, \delta) = 0.0551$. For the equivalent new defect $d/h = 0.1173$, we obtain $X_m(\zeta, \delta) = 0.2221$. The safe buckling load as per the first and third methods are 1.14 kPa and 4.60 kPa respectively.

Now we consider both membrane and bending stress intensity. For actual defect $d/h = 1.5$ and $\zeta_{m+b} = 2.69$, we obtain from the chart $X_{m+b}(\zeta, \delta) = 0.0502$. For the

equivalent new defect $d/h = 0.1173$, we obtain from the chart $X_{m+b}(\zeta, \delta) = 0.2040$. The safe buckling load as per the first and third method are 1.56 kPa and 6.34 kPa respectively.

To be conservative, we adopt the first estimates as the safe loads.

6.3.2 L-shaped shell

For the L-shaped shell, the notional load is $N = 1000$ N/m, and the load multiplier $\lambda = 9.78$.

From linear stress analysis, as shown in Fig. 3.20, P_m is 59.79 MPa and $P_m + P_b$ is 84.6 MPa. Accordingly,

$$\zeta_m = \frac{59.79 \times 9.78}{220} \approx 2.66 \tag{6.7}$$

and

$$\zeta_{m+b} = \frac{84.6 \times 9.78}{220} \approx 3.76. \tag{6.8}$$

From the charts, for an actual defect $d/h = 1.5$ and $\zeta_m = 2.66$, we obtain $X_m(\zeta, \delta) = 0.0507$. For the equivalent new imperfection value $d/h = 0.07$, we obtain $X_m(\zeta, \delta) = 0.2353$. The safe buckling load as per the first and third methods are 198.34 N/m and 920.49 N/m.

Similarly, for $d/h = 1.5$ and $\zeta_{m+b} = 3.76$, we obtain from the chart $X_{m+b}(\zeta, \delta) = 0.0378$. For the equivalent new imperfection value $d/h = 0.07$, we obtain from the chart $X_{m+b}(\zeta, \delta) = 0.1791$. The safe buckling loads as per the first and third methods are 221.81 N/m and 1.05 kN/m respectively.

To be conservative, we again adopt the first set of values.

6.4 Verification and validation of nonlinear buckling procedure

6.4.1 Geometry

Section 6 of [53] reports on semi-analytical nonlinear buckling analyses of imperfect axisymmetric spherical shells. The analyses are carried out for spherical shell for different radius to thickness ratios and various dimple defects at the poles. Here, to validate our ABAQUS calculations, we will reproduce results for one specific case in which the radius to thickness ratio is 100 and the defect magnitude is half of the shell thickness ($\delta = 0.5$). In [53], the actual shell radius R is not specified because the nondimensionalized answer does not depend on it. In our ABAQUS calculation, we consider a shell radius $R = 5$ m, thickness $t = 0.05$ m, and defect magnitude $d = 0.025$ m. We have modelled the upper half of the spherical shell with axis-symmetric elements, and used a symmetric boundary condition at the equator. Figure 6.4 shows the schematic of the perfect spherical shell.

The shell is subjected to uniform external pressure with a notional value of $N = 2.421 \times 10^7$ Pa, which is the elastic buckling pressure of the corresponding perfect spherical shell obtained by linear buckling analysis. The dimple defect geometry in [53] is defined as

$$w_I(\theta) = -d \times e^{-\left(\frac{(\theta - \frac{\pi}{2}) \times \sqrt{\sqrt{1-\nu^2} \times \frac{R}{t}}}{1.5} \right)^2}, \tag{6.9}$$

where ν is 0.3. Cartesian coordinates of the imperfect axisymmetric hemispherical shell profile are computed as

$$x = (R + w_I(\theta)) \times \cos(\theta), \quad y = (R + w_I(\theta)) \times \sin(\theta), \tag{6.10}$$

and used for inputs to ABAQUS.

6.4.2 Nonlinear analysis

We have used the nonlinear buckling analysis procedure 'Static Riks'. Plasticity is excluded as the results reported in [53] are for an elastic material. The load-displacement curve is not given in [53], but the reduction factor $\left(\frac{P}{P_{cr}}\right)$ is reported to be 0.4.

Figure 6.5 shows the load-displacement plot of the imperfect spherical shell from our ABAQUS calculations. The displacement at the pole location is depicted in the plot. The reduction factor $\left(\frac{P}{P_{cr}}\right)$ computed from the present analysis is $0.3973 = 0.40$ to two significant digits, to be compared with 0.4 from [53]. This essentially perfect match with an external researcher serves to validate our ABAQUS simulations.

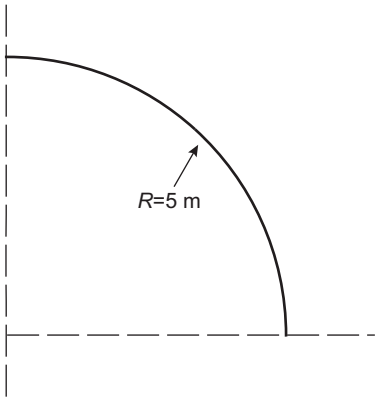

Figure 6.4: Schematic of the spherical shell used for validating our ABAQUS calculations.

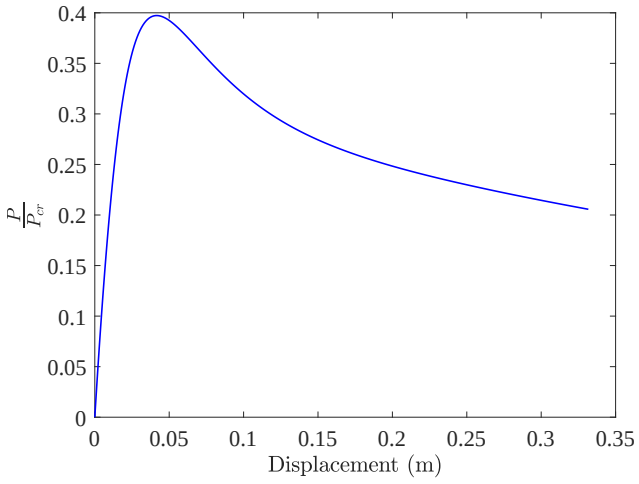

Figure 6.5: Load displacement plot of the spherical shell with dimple defect at poles.

Bibliography

[1] A. W. Leissa, *Vibration of shells*, vol. 288. Scientific and Technical Information Office, National Aeronautics and Space, Washington, D.C., 1973.

[2] E. Ventsel and T. Krauthammer, *Thin plates and shells: theory, analysis, and applications*. Marcel Dekker, New York, 2001.

[3] S. Timoshenko and J. M. Gere, *Theory of elastic stability 2e*. Dover Publications Inc., Mineola, New York, 2009.

[4] L. A. Samuelson and S. Eggwertz, *Shell stability handbook*. Elsevier Applied Science, London, 1992.

[5] D. Bushnell, *Computerized buckling analysis of shells*, vol. 9. Springer, Netherlands, 1985.

[6] T. V. Karman and H. S. Tsien, "The buckling of thin cylindrical shells under axial compression," *Journal of the Aeronautical Sciences*, vol. 8, pp. 303–312, 1941.

[7] G. J. Simitses, "Buckling and post buckling of imperfect cylindrical shells: a review," *Applied Mechanics Reviews*, vol. 39, no. 10, pp. 1517–1524, 1986.

[8] R. C. Tennyson, "A note on the classical buckling load of circular cylinder under axial compression," *AIAA Journal*, pp. 475–475, 1963.

[9] B. O. Almroth, A. M. C. Holmes and D. O. Brush, "An experimental study of the bucking of cylinders under axial compression," *Applied Mechanics Reviews*, vol. 4, pp. 263–270, 1964.

[10] C. D. Babcock, *The buckling of cylindrical shells with an initial imperfection under axial compression loading*. PhD thesis, California Institute of Technology, 1962.

[11] J. Arbocz and C. D. Babcock, "The effect of general imperfections on the buckling of cylindrical shells," *Journal of Applied Mechanics*, vol. 36, no. 1, pp. 28–38, 1969.

[12] P. Mandal and C. R. Calladine, "Buckling of thin cylindrical shells under axial compression.," *International Journal of Solids and Structures*, vol. 37, pp. 4509–4525, 2000.

[13] E. R. Lancaster, C. R. Calladine and S. C. Palmer, "Paradoxical buckling behavior of a thin cylindrical shell under axial compression.," *International Journal of Mechanical Sciences.*, vol. 42, pp. 843–865, 2000.

[14] J. W. Hutchinson and W. T. Koiter, "Postbuckling theory," *Applied Mechanics Reviews*, vol. 23, no. 12, pp. 1353–1366, 1970.

[15] J. G. Teng, "Buckling of thin shells: recent advances and trends," *Applied Mechanics Reviews*, vol. 49, pp. 263–274, 1996.

[16] H. Schmidt, "Stability of steel shell structures," *Journal of Constructional Steel Research*, vol. 21, pp. 159–181, 2000.

[17] American Society of Mechanical Engineers, *Pressure vessel code case N-284. Metal containment shell buckling design methods.* New York, NY., 2015.

[18] RCC-MRx, *Section III-tome-1-subsection Z-Appendix A-7, Analyses taking account of buckling.* AFCEN, Paris, 2012.

[19] C. D. Miller, "Research related to buckling design of nuclear containment," *Nuclear Engineering and Design*, vol. 79, no. 2, pp. 217 – 227, 1984.

[20] B. Autrusson, D. Acker, and A. Hoffmann, "Discussion and validation of a simplified analysis against buckling," *Nuclear Engineering and Design*, vol. 98, no. 3, pp. 379–393, 1987.

[21] S. P. Damodaran, R. Ravi, P. Chellapandi, and S. B. Bhoje, "Buckling behaviour of PFBR main vessel and its thermal baffles under seismic loadings," *Transactions of the 12th International conference on Structural Mechanics in Reactor Technology (SMiRT-12)*, 1993.

[22] P. Chellapandi, S. C. Chetal and B. Raj, "Investigation on buckling of FBR vessels under seismic loadings with fluid structure interactions," *Nuclear Engineering and Design*, vol. 238, pp. 3208–3217, 2008.

[23] R. Ramesh, S. P. Damodaran, P. Chellapandi, S. C. Chetal, and S. B. Bhoje, "Creep buckling problems in fast reactor components," *Transactions of the 13th International conference on Structural Mechanics in Reactor Technology (SMiRT-13)*, 1995.

[24] R. Srinivasan, S. P. Damodaran, P. Chellapandi, and S. B. Bhoje, "Application of simplified buckling analysis rules of RCC-MR (1993) for PFBR-IHX," *Transactions of the 14th International conference on Structural Mechanics in Reactor Technology (SMiRT-14)*, 1997.

[25] G. Gupta and A. K. Sharma, "Buckling Analysis of Sodium to Sodium Heat Exchanger Tubes," *Applied Mechanics and Materials*, pp. 632–638, 2016.

[26] P. Chellapandi, P. Puthiyavinayagam, V. Balasubramaniyan, S. Ragupathy, V. Rajanbabu, S. Chetal, and B. Raj, "Design concepts for reactor assembly components of 500MWe future SFRs," *Nuclear Engineering and Design*, vol. 240, no. 10, pp. 2948–2956, 2010.

[27] P. Chellapandi, P. Puthiyavinayagam, V. Balasubramaniyan, S. Raghupathy, V. R. Babu, S. Chetal, and B. Raj, "Development of Innovative Reactor Assembly Components towards Commercialization of Future FBRs," *Energy Procedia*, vol. 7, pp. 359–366, 2011.

[28] A. Kumar, M. Nandagopal, K. Laha, and A. Chatterjee, "Variability in large-sample postbuckling behavior of two small thin walled structures," *Sadhana*, vol. 46, no. 1, p. 51, 2021.

[29] A. Kumar and A. Chatterjee, "On one imperfection estimation method for thin shell buckling in the design code RCC-MR," *ASME J of Nuclear Rad Sci*, vol. 5, no. 4, 2018.

[30] A. Kumar and A. Chatterjee, "Unequivocally nonconservative results from one method of imperfection quantification in RCC-MR," *ASME J of Nuclear Rad Sci*, vol. 7, no. 1, 2020.

[31] W. Pengfei, C. Tang and Y. Yang, "Structural reliability and reliability sensitivity analysis of extremely rare failure events by combining sampling and surrogate model methods," *Proceedings of the Institution of Mechanical Engineers, Part O: Journal of Risk and Reliability*, vol. 233, no. 6, pp. 943–957, 2020.

[32] H. Cheng, J. Tao, X. Chen and Y. Jiang, "Fatigue reliability evaluation of structural components under random loadings," *Proceedings of the Institution of Mechanical Engineers, Part O: Journal of Risk and Reliability*, vol. 228, no. 5, pp. 469–477, 2014.

[33] V. L. Ontiveros, M. Modarres and M. Amiri, "Estimation of reliability of structures subject to fatigue loading using plastic strain energy and thermodynamic entropy generation," *Proceedings of the Institution of Mechanical Engineers, Part O: Journal of Risk and Reliability*, vol. 229, no. 3, pp. 220–236, 2015.

[34] J. Singer, J. Arbocz, and T. Weller, *Buckling Experiments: Experimental Methods in Buckling of Thin-Walled Structures, Vol. 2*, vol. 17. John Willy and Sons Inc., New York, 2002.

[35] M. K. Chryssanthopoulos, "Probabilistic buckling analysis of plates and shells," *Thin-Walled Structures*, vol. 30, no. 1, pp. 135 – 157, 1998.

[36] K. Sabarethinam and J. E. Padgett, "Stochastic modeling of geometric imperfections in aboveground storage tanks for probabilistic buckling capacity estimation," *ASCE-ASME Journal of Risk and Uncertainty in Engineering Systems, Part A: Civil Engineering*, vol. 2, no. 2, 2016.

[37] E. A. Gotsulyak, O. A. Lukyanchenko and V. V. Shakh, "On stability of cylindrical shells of variable thickness with initial imperfections," *International Applied Mechanics*, vol. 45, no. 4, p. 433, 2009.

[38] V. Papadopoulos, G. Stefanou and M. Papadrakakis, "Buckling analysis of imperfect shells with stochastic non-gaussian material and thickness properties," *International Journal of Solids and Structures*, vol. 46, no. 14, pp. 2800 – 2808, 2009.

[39] T. M. Roudsari, M. Gordini, H. Fazeli, and B. Kavehei, "Probability analysis of double layer barrel vaults considering the effect of initial curvature and length imperfections simultaneously," *International Journal of Steel Structures*, vol. 17, no. 3, pp. 939–948, 2017.

[40] J. Arbocz and M. W. Hilburger, "Toward a probabilistic preliminary design criterion for buckling critical composite shells," *AIAA Journal*, vol. 43, no. 8, pp. 1823–1827, 2005.

[41] T. Trayana, L. S. da Silva, M. Liliana, C. Rebelo, and A. Taras, "Towards a standardized procedure for the safety assessment of stability design rules," *Journal of Constructional Steel Research*, vol. 103, pp. 290 – 302, 2014.

[42] A. Lee, F. L. Jiménez, J. Marthelot, J. W. Hutchinson, and P. M. Reis, "The geometric role of precisely engineered imperfections on the critical buckling load of spherical elastic shells," *Journal of Applied Mechanics*, vol. 83, no. 11, pp. 111005–111005–11, 2016.

[43] O. Ifayefunmi, "Buckling behavior of axially compressed cylindrical shells: Comparison of theoretical and experimental data," *Thin-Walled Structures*, vol. 98, pp. 558 – 564, 2016.

[44] J. C. Wohlever and T. J. Healey, "A group theoretic approach to the global bifurcation analysis of an axially compressed cylindrical shell," *Computer Methods in Applied Mechanics and Engineering*, vol. 122, no. 3-4, pp. 315–349, 1995.

[45] D. S. ABAQUS, "Abaqus documentation (6.17)," *Providence, RI*, 2014.

[46] RCC-MRx, *Section III-tome-1-subsection Z-Appendix A-3, Properties groups for materials*. AFCEN Paris, 2012.

[47] J. Zhang, M. Zhang, W. Tang, W. Wang and M. Wang, "Buckling of spherical shells subjected to external pressure: A comparison of experimental and theoretical data," *Thin-Walled Structures*, vol. 111, pp. 58 – 64, 2017.

[48] M. Tall, S. Hariri, P. L. Grognec, and Y. Simonet, "Elastoplastic buckling and collapse of spherical shells under combined loadings," *Thin-Walled Structures*, vol. 123, pp. 114 – 125, 2018.

[49] Y. Zhu, Y. Dai, Q. Ma, and W. Tang, "Buckling of externally pressurized cylindrical shell: A comparison of theoretical and experimental data," *Thin-Walled Structures*, vol. 129, pp. 309 – 316, 2018.

[50] B. Raj, P. Chellapandi, and P. R. V. Rao, *Sodium fast reactors with closed fuel cycle*. CRC Press, 2015.

[51] F. L. Jiménez, J. Marthelot, A. Lee, J. W. Hutchinson, and P. M. Reis, "Technical Brief: Knockdown Factor for the Buckling of Spherical Shells Containing Large-Amplitude Geometric Defects," *Journal of Applied Mechanics*, vol. 84, no. 3, p. 4, 2017.

[52] A. Lee, F. L. Jiménez, J. Marthelot, J. W. Hutchinson, and P. M. Reis, "The Geometric Role of Precisely Engineered Imperfections on the Critical Buckling Load of Spherical Elastic Shells," *Journal of Applied Mechanics*, vol. 83, no. 11, p. 11, 2016.

[53] J. W. Hutchinson, "Buckling of Spherical Shells Revisited," *Proceedings of the Royal Society A: Mathematical, Physical and Engineering Sciences*, vol. 472, no. 2195, p. 25, 2016.

[54] L. Seaman, *The Nature of Buckling in Thin Spherical Shells*. Ph.D. dissertation, Cambridge, MA, USA, 1962.

[55] ASME, *Boiler & Pressure Vessel Code, Section VIII Rules for Construction of Pressure Vessels Division 2 Alternative Rules*. The American Society of Mechanical Engineers, Two Park Avenue, New York, NY 10016-5990, 2019.